



HAL
open science

Extensions of the scalar sector: from compositeness to dark matter and back

Lara Mason

► **To cite this version:**

Lara Mason. Extensions of the scalar sector: from compositeness to dark matter and back. Physics [physics]. Université de Lyon; Randse Afrikaanse Universite (Johannesburg), 2022. English. NNT: 2022LYSE1025 . tel-03953984

HAL Id: tel-03953984

<https://theses.hal.science/tel-03953984>

Submitted on 24 Jan 2023

HAL is a multi-disciplinary open access archive for the deposit and dissemination of scientific research documents, whether they are published or not. The documents may come from teaching and research institutions in France or abroad, or from public or private research centers.

L'archive ouverte pluridisciplinaire **HAL**, est destinée au dépôt et à la diffusion de documents scientifiques de niveau recherche, publiés ou non, émanant des établissements d'enseignement et de recherche français ou étrangers, des laboratoires publics ou privés.



N°d'ordre NNT : 2022LYSE1025

THESE de DOCTORAT DE L'UNIVERSITE DE LYON

Opérée au sein de l'**Université Claude Bernard Lyon 1**
En cotutelle avec l'**Université de Johannesburg – Afrique du Sud**

Ecole Doctorale N° ED 52
Physique et Astrophysique de Lyon (PHAST)

Discipline : Physique

Soutenue publiquement le 04/03/2022, par :
Lara Mason

Extensions of the scalar sector

From compositeness to dark matter and back

Devant le jury composé de :

FUKS, Benjamin: Professeur des Universités, Université Paris Sorbonne (Président)

DE CURTIS, Stefania: Directrice de Recherche INFN Italie, Istituto Nazionale di Fisica Nucleare (Rapporteuse)

KRAML, Sabine: Directrice de Recherche CNRS, CNRS/Université Grenoble Alpes (Rapporteuse)

DELAUNAY, Cedric: Chargé de Recherche CNRS, CNRS (Examineur)

MAHMOUDI, Farvah: Maître de Conférences, Université Lyon 1 (Examinatrice)

DEANDREA, Aldo: Professeur des Universités, Université Lyon 1 (Directeur de thèse)

CORNELL, Alan: Professeur des Universités, University of Johannesburg (Co-directeur de thèse)

Extensions of the scalar sector

From compositeness to dark matter and back



Lara Mason

Institut des deux Infinis | Department of Physics
l'Université Claude Bernard Lyon 1 | University of Johannesburg

This dissertation is submitted for the degree of
Doctor of Philosophy in Physics

Supervised by

Aldo Deandrea
Alan S. Cornell

December 2021
11933420 | 220031336

Declaration

I hereby declare that except where specific reference is made to the work of others, the contents of this dissertation are authentic and original and have not been submitted in whole or in part for consideration for any other degree or qualification in this, or any other university.

Lara Mason

December 2021

11933420 | 220031336

The work presented in this thesis is based on the following publications and proceedings, in collaboration with others, during the author's PhD studies between January 2019 and December 2021:

- A.S. Cornell, A. Deandrea, T. Flacke, B. Fuks, L. Mason, *Contact interactions and top-philic scalar dark matter*, Journal of High Energy Physics (2021), no.7, 026 [[arXiv:2104.12795](#)]
- A.S. Cornell, A. Deandrea, B. Fuks, L. Mason, *Future lepton collider prospects for a ubiquitous composite pseudo-scalar*, Phys. Rev. D **102** (2020), no. 3, 035030 [[arXiv:2004.09825](#)]
- A.S. Cornell, W. Doorsamy, B. Fuks, G. Harmsen, L. Mason, *Boosted decision trees in the era of new physics: a smuon analysis case study*, [[arXiv:2109.11815](#)]
- L. Mason, A.S. Cornell, A. Deandrea, B. Fuks, *Bottom-quark contributions to composite pseudo-scalar couplings at LHC*, Frascati Physics Series: Strong dynamics for physics within and beyond the Standard Model at LHC and Future Colliders (2019), V70, 110-115, [[hal-02550156](#)]
- L. Mason, A.S. Cornell, A. Deandrea, B. Fuks, *The ubiquitous pseudo-scalar in composite Higgs models*, proceedings of the South African Institute of Physics conference (2019) ISBN: 978-0-620-88875-2)

In addition, results presented in Chapter 4 and in the latter part of Chapter 5 are derived here by the author for the first time.

Acknowledgements

My first and greatest thanks must go to Alan and Aldo. I couldn't have asked for a better pair of supervisors, who ground through university bureaucracy to organise this joint degree for me, who have made these three years a pleasure, and who have allowed me to stand on my own two feet as a physicist.

Thank you to Alan, who is always supportive and always on my side, but also knows when to push me, not least when he made me listen to heavy metal music non-stop on two eight hour drives. Thanks to him for steering me to many exciting opportunities, for our weekly meetings where our conversations veered completely off topic, and for being the reason for the re-emergence of my Australian inflections.

Equal thanks go to Aldo, knowledgeable and approachable in perfect balance. Thanks to him for always being so encouraging and for having confidence in me, for giving me biscuits and coffee when I cried in his office, for driving me and my large suitcases around Lyon, and for showing me anything is possible when he once ate two pizzas in one sitting while we were at dinner in Italy together.

A third and heartfelt thank you to Benj, my 'unofficial supervisor'. I'm very grateful to him for being so generous with his time and with his knowledge, and also for sitting through 16 hours of Alan's heavy metal music with me. I count myself very lucky to have worked with him.

A few more very important thank yous to: Shahrâm: *king of pizza, bikes, and ice cream, and the kindest person around*, Tom: *precise, knowledgeable and supportive, a collaborator I was lucky to have*, Giacomo: *probably the most cited person in this work, for many lunch discussions over Margheritas*, Sylvie: *elle s'occupe de nous tous*, and Amelie: *oh-so-generous and baker extraordinaire*. Thanks to Rach, Ema, Lianie, Gerhard, Wesley, Hotel Doll-Sautel-Vatani, and the IP2I doctorants. Thank you to the many physicists I have emailed out of the blue, and who have unfailingly written helpfully back. That generosity is my favourite thing about this field. And to my family, with special mention to my siblings, scientific and otherwise, to my mum for eternal support, to Dad, who valiantly reads through each of my papers, and to Sean, who reads as far as the abstract. I am lucky to have such love in my life.

Abstract

Composite Higgs models are a branch of Beyond the Standard Model theories which seek to address the hierarchy problem inherent to the current formulation of the Standard Model. In this thesis, we discuss and implement extensions to the scalar sector of the Standard Model, focusing on models of compositeness and their associated phenomenology. A key area of interest is then the appearance of compositeness at current and future colliders, which can be used to motivate the choice of the new era of experimental programs. To that end, this work details the construction of a number of effective models which are testable at colliders, and which are linked as extensions to the scalar sector. We include a comparison of twelve minimal composite Higgs modes featuring an underlying fermionic completion, and discuss ubiquitous features expected across all such models, including a light pseudo-scalar, which is shown to be reachable at future lepton colliders with the help of machine learning techniques. The study also reveals the consideration of bottom quarks in fermion-loops coupling the light scalar to SM states to be non-negligible. Phenomenology at future lepton colliders is extended through a study of the most minimal composite Higgs model of this nature, $SU(4)/Sp(4)$, where we outline a potential search for the heavy pseudo-Nambu Goldstone boson η , considering both fermiophobic and fermiophilic couplings. While composite Higgs models seek primarily to address the separation of the electroweak and Planck energy scales, some such models may also produce dark matter candidates. We conclude this work with an investigation into heavy dark matter which couples to the top-sector of the Standard Model via a t -channel interaction, situating it within a composite Higgs model through its interaction with a heavy fermionic mediator and a top partner. Finally, the visibility of the model at colliders and astrophysical experiments is examined.

Extension du secteur scalaire des modèles composites à la matière noire

Le modèle Standard, qui gouverne la physique des particules, est une théorie très établie. Dans cette théorie, les champs et les forces sont gouvernés par une combinaison de relativité et de mécanique quantique. Ces dernières années, les propositions d'extension ou de modification du modèle Standard (MS) se sont rapidement multipliées. Ces extensions sont dues à des questions irrésolues qui suggèreraient que la théorie n'est pas complète. Au cours de la dernière décennie les plus importantes contributions à la recherche de « Beyond the Standard Model » (BSM) ont été dues aux collisionneurs tels que le Large Hadron Collider (LHC) au CERN, qui ont fourni d'énormes quantités de données à l'échelle du TeV depuis ses premières collisions en 2009. Deux expériences au LHC, ATLAS et CMS, ont contribué à la découverte du boson de Higgs, la dernière pièce du puzzle MS, en 2012.

Le Higgs est apparu comme une résonance élémentaire de spin 0, unique en son genre, avec une masse de 125 GeV. Il est crucial pour le fonctionnement du SM par sa contribution au mécanisme de brisure de symétrie électrofaible (EWSB), se produisant à une échelle $v = 246$ GeV. La découverte du boson de Higgs a été considérée comme la confirmation d'une théorie présentée pour la première fois dans les années 1960. Sans cette théorie, le SM ne pourrait pas prévoir l'univers dans lequel nous nous trouvons. Cependant, sa découverte a également ouvert la voie à un certain nombre de questions sur la nature du SM. L'une de celles est le problème de la hiérarchie. En effet l'échelle de l'EWSB choisie par la nature est anormalement basse par rapport à l'échelle de Planck, qui est la borne énergétique supérieure de la théorie. Un certain nombre de modèles ont été présentés pour résoudre ce problème du « non naturel ». Une piste de recherche prometteuse est celle des modèles composites, qui sont le sujet principal de cette thèse. Dans ces modèles, le boson de Higgs se défait de sa nature élémentaire et apparaît comme un état lié de fermions fondamentaux, soumis à une nouvelle interaction forte.

Le modèle original, qui remplace le secteur de Higgs par une dynamique de jauge fondamentale comportant des champs de matière fermionique, est le *technicolor*. Cette théorie brise la symétrie EW par le condensat des fermions. Le principe de la technicolor est que le secteur qui est responsable de l'EWSB interagit fortement ; le condensat des fermions brise la symétrie EW et crée le boson de Higgs par le même procédé. Par analogie avec la technicolor, les modèles composites remplacent le secteur scalaire du

modèle Standard par un secteur régi par une dynamique forte. Dans ce secteur, les fermions fondamentaux possèdent une symétrie globale de saveur. Le groupe « hypercolor » qui gouverne les fermions est laissé ininterrompu dans la théorie, mais le groupe de saveur est divisé en un sous-groupe. Ces modèles sont confinés aux basses énergies. Le boson de Higgs est un état lié de fermions confinés par une interaction de jauge forte, qui se condensent à l'échelle caractéristique du confinement. Tout comme en Quantum Chromo Dynamic et en technicolor, la symétrie de saveur est dynamiquement brisée en un sous-groupe par un processus de condensation.

Dans cette thèse, nous présentons un nombre d'études sur la phénoménologie des extensions au secteur scalaire de la physique des particules. Nous nous concentrons principalement sur les modèles composites et présentons de nombreuses façons dont ils peuvent être vus dans les collisionneurs. Nous proposons des motivations de recherche sur les futurs collisionneurs. L'accent est mis sur les modèles comportant des fermions sous-jacents, et nous présentons également des motivations théoriques tout en mentionnant les contraintes existantes.

Nous commençons par discuter les modèles composites dans le chapitre 2. La première étude phénoménologique est présentée dans le chapitre 3 où nous enquêtons sur une particule pseudo-scalaire légère qui apparaît omniprésente dans de similaires modèles composites. L'analyse comporte douze configurations possibles du modèle composite de Higgs et utilise des techniques de « machine learning » pour améliorer les analyses traditionnelles de « cut-and-count ». Nous explorons l'utilisation de ces techniques dans un futur collisionneur électron-positon (e^+e^-). L'étude montre la puissance des futurs collisionneurs, qui seront des « usines » à particules telles que le Higgs, produisant des millions de collisions et permettant des mesures très précises de leurs propriétés. Les secteurs scalaires étendus comportant des pseudo-scalaires sont intéressants car ils peuvent être largement modélisés en fonction de leurs propriétés et interactions, tout en figurant dans de nombreux scénarios BSM différents. Dans cette thèse nous considérerons le pseudo-scalaire qui apparaît en raison d'une brisure de symétrie $U(1)$ dans les modèles composites comme un bon candidat pour une recherche qui est de type axion (ALP). Dans cette étude, nous étudions la production de l'ALP avec un boson Z et utilisons des techniques de « machine learning » (BDTs) pour séparer le signal du bruit de fond.

Nous présentons ensuite, dans le chapitre 4, une analyse plus approfondie du scénario du modèle composite $SU(4)/Sp(4)$ qui comprend une présentation des brisures de symétrie et des potentiels pertinents présents dans la théorie. Nous profitons de cette occasion non seulement pour examiner certaine phénoménologie, mais aussi pour présenter une explication plus approfondie du fonctionnement d'un modèle composite générique. Cela inclut les brisures de symétrie spontanées et explicites et leurs conséquences physiques. Nous décrivons également une étude phénoménologique de la résonance ' η ' qui est la deuxième caractéristique toujours présente d'un modèle

composite. Étant donné l'existence de résultats EWPT rigoureux, nous avons étudié le cas η le plus lourd, avec une masse supérieure à 500 GeV. Nous nous sommes concentrés principalement sur des scénarios fermiophobes, qui mènent à des signaux intéressants mais souffrent d'une faible production rendant difficile leur recherche dans ce modèle.

Enfin, nous présentons dans le chapitre 5 une tentative pour décrire un candidat de matière noire lourd dans un modèle composite, en envisageant que le candidat de matière noire se présente comme une résonance scalaire. La description du Higgs dans un modèle composite offre non seulement une solution au problème de hiérarchie, mais peut aussi naturellement générer un candidat de matière noire de multiples façons. Ceci sera discuté plus loin dans cette thèse, où nous présenterons une nouvelle approche pour inclure la matière noire dans un modèle composite. Cette nouvelle approche, au contraire de l'approche bien connue de la matière noire pNGB, a l'avantage de pouvoir être incluse dans un modèle composite présentant n'importe quelle symétrie de saveur. Comme beaucoup d'autres modèles, nous incluons une symétrie Z_2 dans la théorie, selon laquelle le candidat à la matière noire sera impair et toutes les particules SM seront paires. Le candidat se couple uniquement au secteur 'top', et son théorie efficace a été déjà proposé. À cette fin, nous ajoutons à un modèle existant un terme générique de dimension-cinq qui devrait apparaître dans un certain nombre de théories BSM. Nous étudions la densité relique et effectuons un ajustement semi-analytique aux données simulées. Nous étudions ensuite la détection directe et indirecte et examinons les contraintes du collisionneur. Enfin, nous étudions l'impact sur la phénoménologie d'un « top partner », une particule lourde supplémentaire qui est un composant fondamental dans de nombreux modèles composites. Nous discutons des interactions supplémentaires qui peuvent survenir et expliquons pourquoi on ne s'attendrait pas à des modifications des contraintes du collisionneur en raison de cette nouvelle résonance. Au lieu de cela, d'autres investigations devraient se concentrer sur des expériences d'astrophysiques pour en déduire d'autres limites.

Pour connaître la vraie nature de la physique des particules, nous devons continuer à avancer vers des énergies plus élevées pour étudier les limites supérieures du SM. Cette thèse a introduit un certain nombre de modèles effectifs qui démontrent la portée des théories composite. Nous y avons motivé l'extension du secteur scalaire comme le lieu où peuvent être trouvées les réponses à certaines des questions les plus importantes de la physique des particules.

Table of contents

1	Introduction	1
1.1	The emergence of the Higgs	2
1.2	An Effective Field Theory	5
1.3	Symmetries	7
1.3.1	Symmetry breaking; spontaneous or otherwise	8
1.4	Looking Beyond the Standard Model	9
1.4.1	<i>How?</i> : Physics at colliders	9
1.4.2	<i>Why?</i> : The hierarchy problem	10
1.5	Extending the scalar sector	13
2	The composite Higgs solution	15
2.1	Technicolour: a precursor to compositeness	17
2.2	Composite Higgs models	18
2.2.1	Fermions all the way down	20
2.2.2	Vacuum misalignment	22
2.2.3	Fermion mass generation	24
2.2.4	Vector-like quarks	26
2.3	Experimental constraints	27
3	A light composite hint at future colliders	29
3.1	Singlet axial symmetry	33
3.2	Effective model	34
3.2.1	<i>b</i> -quark effects	37
3.3	Collider phenomenology	39
3.3.1	Future lepton colliders	40
3.3.2	An FCC-ee case study	45
3.3.3	Testing a signal hypothesis	46
3.4	Cut-and-count	47

3.5	Machine learning	51
3.5.1	Boosted decision trees	52
3.5.2	Application of XGBOOST	54
3.5.3	Approximate median discovery significance	55
3.5.4	XGBOOST results	56
3.6	Conclusion	58
4	An $SU(4)/Sp(4)$ case study	61
4.1	The underlying model	62
4.2	The Effective Field Theory framework	63
4.2.1	The chiral effective model	64
4.2.2	Scalar potential	65
4.2.3	Explicit symmetry breaking: fermion couplings	66
4.2.4	WZW and triangle boson couplings to η	68
4.3	Phenomenology at colliders	69
4.3.1	Fermiophobic phenomenology	71
4.4	Conclusion	74
5	Top-philic dark matter in a composite model	75
5.1	Heavy dark matter and a t -channel mediator	79
5.2	Fitting the relic density curve	82
5.2.1	Parametrising the shift due to coannihilations	85
5.3	Direct detection constraints	88
5.4	Indirect detection constraints	94
5.5	Collider constraints	95
5.5.1	Recasting an analysis and the CL_s technique	97
5.6	Reinterpreted LHC analysis results	98
5.7	A top partner	102
5.7.1	Experimental discussion	104
5.8	Conclusion	106
6	Concluding remarks	107
	References	111

Chapter 1

Introduction

Particle physics finds itself, both theoretically and experimentally, in a period of flux. The reigning theory is the Standard Model (SM), an incredibly successful theory developed in the early 1970s which collects the fields and forces of particle physics and governs them by a combination of special relativity and quantum mechanics. In recent years, proposals to extend or modify the theory to address outstanding questions have been rapidly increasing, and the dominant contributions to explorations of Beyond the Standard Model (BSM) theories in the past decade have been due to colliders such as the Large Hadron Collider (LHC) at CERN, which has delivered enormous amounts of data at the TeV scale since its first collisions in 2009. Two experiments at the LHC, ATLAS and CMS, famously announced the discovery of the Higgs boson, the final piece of the SM puzzle, in 2012 [1, 2]. The Higgs appeared as an elementary spin-0 resonance, the only one of its kind, with a mass of 125 GeV. It is crucial to the functioning of the SM through its contribution to the electroweak symmetry breaking (EWSB) mechanism [3], occurring at a scale $v \sim 246$ GeV. The discovery of the Higgs was viewed as confirmation of a theory first proposed in the 1960s without which the SM would not predict the universe in which we find ourselves. However, its discovery also paved the way for a number of questions probing the nature of the SM. One such question is that of the hierarchy problem, where the scale of EWSB chosen by nature is unnaturally low in comparison to the Planck scale, which would be the upper energy bound of the theory should the SM not be an effective model. A number of models have been proposed to address this issue, offering BSM solutions to this problem of ‘unnaturalness’. A promising avenue of exploration is that of compositeness, a main subject of this thesis, where the Higgs boson sheds its elementary nature and appears instead as a bound state of fundamental fermions, subject to strong dynamics.

The SM is an incredibly successful theory; of that there can be little doubt. It is arguably the most precise theory ever, and features predictions across a range of energies. Including elementary matter and gauge fields, it is a spontaneously broken non-Abelian gauge theory which has been constructed and rigorously tested over the past 50-odd years. The inception of the SM was the unification of the electromagnetic and weak forces by Glashow, Weinberg and Salam [4–6], and it incorporates three of the four fundamental forces, along with matter particles and force carriers. At the time of this writing, the measurements taken at colliders remain overwhelmingly in agreement with the SM. Small deviations have been sighted, including those in the measurements of the muon magnetic moment [7, 8], and a number of B decay processes involving $b \rightarrow s \ell^+ \ell^-$ ($\ell = e, \mu$) have been measured experimentally to disagree with SM predictions [9–18]. Despite a huge variety of experimental searches however, no new particles have been sighted. Why, then, would we seek to go beyond the SM? In fact, the plethora of BSM studies that are currently being pursued are motivated by a number of outstanding questions, including the origin of matter/antimatter asymmetry, the origin of neutrino masses, the (only partial) quantum description of gravity, the lack of CP violation in strong interactions, the origin of hierarchy in fundamental scales, and the nature of dark matter. The final two points will be discussed and addressed in this thesis, and we leave the former points to others. More than anything, we consider that the SM is an effective field theory (EFT), expected to be valid only up to some energy scale. Above that energy scale, new physics is expected to occur.

1.1 The emergence of the Higgs

Much of the work on scalar extensions of the SM that will follow in subsequent chapters revolves around the Higgs sector and the extension thereof. The light scalar state first observed at CERN [1, 2] in 2012 confirmed the existence of a resonance, charged under the SM group $SU(3)_c \times SU(2)_L \times U(1)_Y$, with Higgs-like couplings to some SM particles. This 125 GeV particle has largely been accepted to be the Higgs boson, predicted in 1964 [19] as the excitation of the Higgs field which was also first theorised in the same year [20, 21]. In the latter paper, Francois Englert and Robert Brout discuss a mechanism that may give mass to Yang-Mills fields extending a Lie group from a global to a local symmetry; the gauge bosons. They showed that the gauge invariance of the theory with a degenerate vacuum can be maintained despite the acquisition of mass, through what is now called the Brout-Englert-Higgs

mechanism. In the paper written by Peter Higgs [19], the author extended work done on superconductors by Anderson [22] to outline a case in which Goldstone’s theorem [23, 24], where massless Goldstone bosons are produced, fails. Instead, Higgs showed that the gauge fields acquired mass, which had already been seen in experiment. Crucially, it was only Peter Higgs who predicted the existence of a massive boson, now named after him, which would accompany this mechanism. Nearly 50 years later, the particle on which the SM depended for the origin of mass was observed.

In the SM $SU(2)_L \times U(1)_Y$ electroweak (EW) theory, the Higgs sector consists of one complex Higgs doublet, and therefore one Higgs boson [25]. The scalar part of the SM Lagrangian, which describes the dynamics of the Higgs boson, is written as

$$\mathcal{L}_{Higgs} = (D^\mu \phi)^\dagger (D_\mu \phi) - V(\phi), \quad (1.1)$$

where the first term encodes the kinematics of the state, and the second is the potential, written as

$$V(\phi) = -\mu^2 \phi^\dagger \phi + \lambda (\phi^\dagger \phi)^2. \quad (1.2)$$

Notably, the ‘mass term’ for the Higgs is encoded in its potential, and the λ parameter describes the quartic self interaction. The potential is $SU(2)_L \times U(1)_Y$ -invariant but its true vacuum state is not, as the minimum corresponds to $\langle |H| \rangle = v/\sqrt{2}$. When $\mu^2 < 0$, the scalar field develops a vacuum expectation value (vev) v , and spontaneously breaks the symmetry; that is, a negative value of μ^2 leads to a set of equivalent minima lying in a hypersphere of radius $\sqrt{-\mu^2/(2\lambda)}$, with $\langle \phi \rangle = 0$ an unstable local maximum. The choice of one of the minima by rolling down the slope of the well-known Mexican hat potential spontaneously breaks the rotational symmetry. Invariance under the $U(1)$ symmetry associated to electromagnetism remains.

Minimising the potential and examining perturbations around the ground state results in a massive (real) scalar particle, with tree-level mass $\sqrt{-\mu^2}$. The appearance of such a resonance is an unavoidable consequence of spontaneous symmetry breaking, which also leads to three massless Goldstone bosons which are ‘eaten’ by the gauge bosons W and Z . More detail on this process is available in the literature, such as in Ref. [26]. The discovery of the SM Higgs in 2012 allowed the parameters of the potential to be experimentally fixed, defining the scale of the masses of the SM particles.

The problem solved by the Higgs mechanism within the SM is, in particular, that of the masses of the weak gauge bosons. In an unbroken EW theory, the massless gauge bosons need an extra degree of freedom to become massive [27]. The solution is linked

to Goldstone's theorem, where three broken generators yield three degrees of freedom, to be 'eaten' by the W and Z gauge bosons. In the absence of EWSB, three components of the Higgs field would have massless Goldstone excitations. However, when we gauge the theory with the EW interactions, these excitations are the longitudinal modes for the massive EW gauge bosons [28]. One of the foremost goals of high energy physics is to establish the origin of the EWSB mechanism. While the discovery of the Higgs was the jewel in the SM crown, allowing the gauge bosons and fermions to obtain the masses we observe experimentally, it does not explain the dynamics underlying the spontaneous symmetry breaking. The discovery of this final piece of the SM puzzle has therefore brought with it its own problems, and has been a driving factor in the theories seeking to extend the SM as it currently stands. Many are convinced that the origin of new physics must be in the scalar sector, and that the answers to many of the open questions in the SM lie with the Higgs.

The need for composite Higgs models, promising BSM avenues which extend the scalar sector, arises because the SM Higgs is an elementary weakly coupled particle which interacts with physics at a scale Λ , and would therefore be expected to have a mass on the order of Λ . The observation of the Higgs boson at 125 GeV suggests that Λ should be low, in contradiction with the non-observance of new physics seen at colliders. At present, the upper limit on the SM is the Planck scale, where 19 orders of magnitude separate the Planck mass and the EW scale. In order to keep the Higgs this light, we require a huge amount of fine tuning, which doesn't sit well with physicists. Instead of requiring this fine tuning, we can instead systematically solve the issue by introducing new symmetries which result in the Higgs mass only being sensitive up to a new energy scale Λ' not far above the EW scale. Under these symmetries the Higgs boson is instead a composite object, and arises as a bound state of fermionic matter [29, 30]. If the Higgs boson is a bound state of a new strong sector rather than an elementary scalar, quantum corrections to its mass may only contribute up to a finite scale, stabilising the Higgs field dynamics [31].

It should be emphasised that the hierarchy problem is not an aesthetic one. The fact that the only fundamental scalar ever observed is subject to quantum corrections to its mass highlights a tension between the immovable laws of quantum field theory on one hand and the way that nature appears to present itself on the other. The rigid laws of quantum mechanics and relativity seem to want to make our universe unnatural via the Higgs sector. There is therefore good reason to expect that it is the Higgs sector which holds the clues for BSM physics, and one may then be motivated

to place the scalar sector under a theoretical and experimental microscope, as we will aim to do in this work.

1.2 An Effective Field Theory

The golden thread which weaves through this discussion is that of energy scales defining the relevant physics, which will be arguably the most important concept in this thesis. Three known scales of nature which are relevant to the study of high energy particle physics are the EW scale, the quantum chromodynamics (QCD) scale, and the Planck scale, and the gap between the first and the last is the origin of the hierarchy problem. The Planck scale sits at 1.2×10^{19} GeV, which is the scale at which the perturbative semi-classical description of gravity within the SM breaks down [32]. This is the highest energy scale of which we know. At the EW scale, EWSB of the doublets unifying the left-handed (LH) chirality components of up and down fermions occurs. Also referred to as spontaneous symmetry breaking, this is the mechanism through which fermions and massive gauge bosons acquire mass, as discussed in the previous section. It is the EW scale which defines the order of mass in which the EW gauge bosons and the Higgs lie. The lowest of the three, the QCD scale, is characteristic of QCD confinement, below which bound hadron states occur. It sits at around 1 GeV, and echoes of this idea emerge in *technicolour*, the predecessor to composite Higgs models, which will be discussed in the next chapter.

By definition, an EFT like the SM must have a scale below which it is relevant, and higher dimensional operators are added to a theory according to that scale. A composite Higgs theory as will be discussed in subsequent chapters relies on a compositeness scale at which new physics emerges, and far below which the Higgs must lie. This motivates the description of the Higgs as a pseudo-Nambu Goldstone boson (pNGB), where a Goldstone boson acquires a small amount of mass. Before diving into the details of composite Higgs models or any phenomenological studies, let us begin by outlining the construction of EFTs in a little more detail, and examine the concept of symmetries and symmetry-breaking which will be crucial to this work. This construction will be utilised again in each of the proceeding chapters.

In attempting to address any physics question, we must construct a theoretical model, which should make predictions and be testable. Of course, a fundamental theory of everything, from the lowest energy scales to the largest, would be first prize. However, this is generally not realistic and so instead we turn to EFTs [33–35], which allow us to factorise physics of different length scales into manageable portion sizes. In particular,

EFTs for BSM theories parametrise the physics occurring at some (relatively) high energy scale Λ , used to estimate the resulting effects on observables at an energy scale $E \ll \Lambda$. The forms of the operators within the EFT are independent of the physics at the higher scale, and are fully described by the lighter particles which have not been integrated out. This allows for the construction of new theories from Lagrangians, making use of the fact that physical problems come with distinct energy scales. An EFT construction generally simplifies a given problem, ignoring contributions which are not relevant at a given energy scale, and also parametrises additions to known physics, investigating how observables will change with the additions.

Consider physics in the ultraviolet (UV) regime of high energies and short distances, where the dynamics and interactions of quarks and gluons can be written down. As we move to lower energies and longer distances (recalling the uncertainty principle), it no longer makes sense to talk about quark and gluon dynamics, but rather pions. As we continue towards lower energies, we discuss molecules. Each distance scale has an EFT, and associated laws of physics. If the EFT is extendable to the UV, it has a UV completion (although these completions are not unique). To move between higher to lower energies we match parameters between the UV and IR using power counting. This matching features, for example, in the direct detection investigation of chapter 5. Consider the effective theory of Newton's gravity with General Relativity as its UV completion, or effective Fermi Theory with a UV completion in Glashow-Salam-Weinberg EW theory $SU(2)_L \times U(1)_Y$. Thus far, a fully satisfactory UV completion for the SM has not been proposed.

The recipe for constructing an EFT is simple, and will be followed in a number of subsequent chapters in this work. One begins by collecting the fields and constructing all the allowed (local) operators in the theory at the energy of relevance. Symmetries may constrain the interactions, and one may play around with adding a symmetry, or envisioning a small breaking of a symmetry. Parameters attached to operators in the EFT may have dimension as each term in the Lagrangian should be of dimension-four in total. Operators in Lagrangians may be written as

$$\mathcal{L} = C \frac{\mathcal{O}}{\Lambda^{D(\mathcal{O})-4}} \quad (1.3)$$

where Λ is the cut-off, or limit of validity, and C is a typically dimensionless number known as the Wilson coefficient which may be fixed or given by the UV theory. At our scale Λ , scattering amplitudes approach unity as they are proportional to $(E/\Lambda)^n$, where E is the energy, and we lose convergence of the perturbative series. An EFT is then entirely defined by its particle content, the symmetries which are respected (or

broken), and the relevant scale below which we can work. It should be held front of mind, particularly as we move towards composite Higgs models, that the scale Λ defines the strength of the interaction, but not necessarily the energy scale of the new dynamics. Particles are likely to emerge below the scale Λ .

1.3 Symmetries

Symmetries are the backbone of EFTs and particle physics as a whole. They are transformations of the fields which leave the Lagrangian invariant, and play a fundamental role in the formulation of the SM, which can be written down as an $SU(3)_c \times SU(2)_L \times U(1)_Y$ symmetric theory. The first term is the gauge group from which QCD emerges and which governs the strong force, and the second and third terms arise from the unification of the EW group. Here c indicates the ‘‘colour’’ charge, L refers to the left-handed chirality components, and $Y = Q - T_3$ is a generator called hypercharge. The particles of the SM behave according to their representations under the SM symmetry group, which are determined by their charges under each group. The Higgs multiplet is written as $(1, 2)_{1/2}$; that is, it is a singlet under $SU(3)$, a doublet under $SU(2)$, and has a hypercharge value $1/2$. The dynamics of particles are governed by the SM Lagrangian, which is Lorentz-invariant and local, and which should be invariant under the symmetries governing the theory. The Lagrangian contains terms bilinear in the fields which account for the dynamics and (if relevant) masses of the associated particles, and terms with at least three fields, which account for interactions [36]. The Lagrangian for the SM based on $SU(2)_L \times U(1)_Y$ is written as

$$\mathcal{L}_{SM} = \mathcal{L}_{gauge} + \mathcal{L}_f + \mathcal{L}_{Higgs} + \mathcal{L}_{Yuk}, \quad (1.4)$$

where the terms related to the gauge bosons, fermions, Higgs and Yukawa interactions are each indicated separately. The SM is a local gauge theory; the symmetries under which each term of the Lagrangian of eq. (1.4) is invariant govern additional (gauge) fields which describe the interactions between the original fields depending on the spatial coordinate x . Gauge transformations relate equivalent field configurations which correspond to the same physical observable. Gauge invariance implies invariance of the system under gauge transformations, and is a fundamental principle of the SM. In essence, the laws of physics should not change under a space-time transformation. Crucially, while the Lagrangian in eq. (1.4) is symmetric under $SU(2)_L \times U(1)_Y$

transformations, the mass spectrum observed in experiments is not: the vacuum of the system breaks the EW symmetry. This is a crucial component of the SM, and of BSM theories of the Higgs sector.

1.3.1 Symmetry breaking; spontaneous or otherwise

While symmetries are a fundamental component of the SM and theories extending it, the breaking of some symmetries is equally crucial to the dynamics of the theories. Symmetries may be broken explicitly, through terms which do not respect the symmetry of the Lagrangian, or spontaneously, where *states* of a system do not respect the same symmetries as the theory that describes them. A symmetry is approximate if the parameter that breaks it is very small compared to the other parameters in the theory. In the case of both global and gauge symmetries, spontaneous symmetry breaking occurs when the Lagrangian obeys the symmetry, but its solutions do not. There is no explicit symmetry-breaking term introduced, but the vacuum, or ground state, of the system is not symmetric [36]. In the SM, the minimal mechanism for spontaneous symmetry breaking facilitates the breaking of $SU(2)_L \times U(1)$, triggered by the Higgs field obtaining a non-zero vacuum expectation value, as described above. The finite vacuum expectation value of a field means that the field spontaneously breaks EW symmetry not by explicit terms in the Lagrangian, but via the vacuum [37].

Spontaneously broken global symmetries G are governed by Goldstone's theorem [24, 23], which asserts that, for G spontaneously broken to a subgroup H , each broken generator corresponds to a massless mode, or Goldstone boson. If G is gauged into a local symmetry group featuring gauge bosons, the bosons become massive via the Higgs mechanism, which occurs due to the presence of a scalar (Higgs) field ϕ , which breaks the symmetry. After this breaking, the subgroup $H \subset G$ under which the vev of ϕ is invariant allows us to divide the generators of the group G into two sets. Unbroken generators in H annihilate the vacuum, and broken generators are situated in the orthogonal set G/H . Each broken generator in G/H is associated to a Goldstone boson which is by definition massless, carrying the same quantum numbers as the generators [36]. To each broken generator is associated a gauge vector, which acquires a longitudinal degree of freedom and a mass. The Goldstone boson of that broken generator is 'eaten' by the vector to provide this longitudinal degree of freedom, which allows the W^\pm and Z bosons to obtain mass as observed at experiment.

1.4 Looking Beyond the Standard Model

Although the SM has been (and continues to be) an incredibly successful theory, we find two clear classes of problems with the theory which have led to the construction of BSM theories. The first question mark appears as some phenomena which are completely at odds with the SM and are not included in the theory. This class features the problem of dark matter and neutrino masses; if dark matter is a particle, it is not a SM particle, and the theory does not include neutrino masses which have been experimentally observed. The second class of problems with the SM are features within the theory which point to a deeper structural misunderstanding, such as areas where fine tuning is required and the hierarchy of quark and lepton masses. The latter will not be discussed in this work, but the former issue of fine tuning relates to the Higgs mass instability, which is relevant to this work. In motivating the need for BSM physics model-building, the *how* and *why* to go beyond the SM will be briefly discussed, with an emphasis on the topics of this thesis.

1.4.1 *How?: Physics at colliders*

Searching for new particles or making precise measurements of deviations from theory requires a large amount of energy in a controlled environment. BSM physics is, in general, very rare, and only if we control standard physics very well can we reasonably analyse what we produce to detect rare events. Large amounts of energy are required to produce heavy particles, and collisions need to occur at a high rate to ensure enough data is collected to be statistically significant (especially for the rare BSM processes). High energy collider physics is currently dominated by proton-proton collisions at the LHC at CERN. Built to discover the Higgs and having achieved its goal in 2012, its upcoming high luminosity runs (to operate from 2026 with a luminosity target of 3000 fb^{-1}) promise precision measurements of Higgs couplings and searches for new physics. With the LHC nearing its design energy of 14 TeV, a discussion is taking place within the high energy physics community as to the properties of the collider which will succeed the LHC.

The future of particle physics, and indeed the physics at future colliders, necessitates a discussion around whether there is a genuine need to move to higher energies. Sceptics may cite the relative paucity of results at the LHC, where the physics of EWSB hinted that there had to be some new physics below the 1 TeV scale. We find ourselves in another era, much like in the 1960s, where some of the relevant questions challenge the structures of space-time and quantum mechanics. The very fact that we have seen the

Higgs, a fundamental scalar, and nothing else is surely reason enough to examine it with the strongest possible experimental microscope.

A good case for the next collider to be built is made for an electron-positron collider, and proposals which have been put forward include the International Linear Collider (ILC) [38], with initial energies in the range of 250-1000 GeV, the Compact Linear Collider (CLIC) [39], which could reach up to 3 TeV, as well as the Future Circular Collider (FCC-ee) [40] and Circular Electron Positron Collider (CEPC) [41], which will operate around the Z pole and WW threshold, up to energies of 500 GeV [42]. While muon colliders have also been proposed and may offer good precision combined with a high energy reach, they will not be discussed here. Electron-positron machines will operate at a variety of centre of mass energies, many of them lower than the LHC. While the LHC still boasts the largest centre-of-mass collision energy for a circular collider, circular lepton colliders offer large luminosities which will be crucial for discovering weakly interacting particles, as well as for precise measurements. Large circular lepton colliders such as the FCC-ee offer a synergy with the proposed 100 TeV colliders, as the same physical structures may be used. In chapters 3 and 4, searches for composite resonances at future lepton colliders are proposed.

As protons are composite objects and leptons are point-like, the physics at each type of collider is quite different. Proton colliders feature both strong and EW interactions, and are therefore subject to a significant QCD background. Lepton colliders feature mainly EW interactions so are more free of this phenomenon, although high energy collider signals will always be subject to some background from QCD events. The point-like nature of lepton colliders lends itself to a well defined initial state and precision measurements with minimal pileup and underlying events, while hadron collider initial states are less well known due to the composite nature of protons. In this thesis we will present phenomenology across a number of colliders, both current and future, and address how they may be used to address some outstanding questions being asked of the SM.

1.4.2 *Why?: The hierarchy problem*

The hierarchy problem is at the centre of many efforts to extend the scalar sector of the SM, but why is the Higgs special? There are a number of unique quantum number possibilities for particles which are allowed in nature and are compatible with quantum field theory; elementary particles may possess spin-0, 1/2, 1, 3/2, or 2. Fermions, such as the quarks, possess spin-1/2, and the gauge bosons of the SM spin-1. Of fundamental scalar particles (with spin-0), there is only one; the Higgs boson.

Particles possessing spin $3/2$ do not appear in the SM, but we will encounter them in later chapters when discussing vector-like quarks, or top-partners. Particles of spin-2, such as the BSM graviton, will not be discussed. These choices of spin are not imposed for elegance; they are simply all that we are allowed to have. The fact that the Higgs is the only elementary spin-0 particle observed in nature is the origin of the hierarchy problem. While fermions are protected from mass corrections by chiral symmetries, and gauge bosons by the restoration of the gauge symmetry in the massless limit [43], the Higgs is not protected by symmetries from becoming very massive.

This can be seen via the Higgs Lagrangian, which features large interactions which break its shift symmetry; in particular the top Yukawa and gauge couplings are very large, leading to large breakings of the shift symmetry and large corrections to its mass. If a parameter in a theory may feel corrections due to instability against quantum corrections, and we need to keep it smaller than those corrections, then that parameter is fine tuned. In this sense, the hierarchy problem is not an abstract notion at all, but is a very familiar problem. The same issue emerged in early studies of QCD, when it was found that the pions would be subject to quantum destabilisations. This problem was very clearly resolved in QCD, but is not resolved in the SM. The hierarchy problem, emerging from the many orders of magnitude separating the weak and Planck scales, can be argued from a number of perspectives; the loop correction argument is well-known, and is presented for example in Ref. [43]. Following that argument, the effective theory below the SM cut-off can be written as a Lagrangian [32]

$$\mathcal{L}_{SM} = C\Lambda_{SM}^2\mathcal{L}^{(d=2)} + \mathcal{L}^{(d=4)} + \frac{1}{\Lambda_{SM}}\mathcal{L}^{(d=5)} + \frac{1}{\Lambda_{SM}^2}\mathcal{L}^{(d=6)} \quad (1.5)$$

where d indicates the dimension in energy. The term with dimension 2 is the Higgs mass term $c\Lambda_{SM}^2 H^\dagger H$, which by dimensional analysis must come with the included coupling, which should be the Higgs mass m_H . Given that the Higgs mass has been measured to be 125 GeV, we should hope that Λ_{SM} is not too large, or face the prospect of a very small (and very fine-tuned) C . In fact, the m_H that appears in the Lagrangian is not the physical Higgs mass. The Higgs, which is sensitive to the UV scale, undergoes loop corrections to its mass, the largest of which are predicted to be the Higgs self interactions and the top quark loop corrections, since Higgs couplings to fermions are proportional to their masses.

Instead of the loop-correction argument, one may study instead a less-traditional argument more directly based on symmetries, which arises from QCD. The early

motivations for composite Higgs models (via *technicolour*, to be discussed in the following chapter) arose due to possible similarities identified with QCD, and the structure has been preserved in many ways in composite Higgs models. Unlike in the SM, where we may imagine some scale Λ quite far above the Higgs mass (and the EW scale), in QCD we have Λ_{QCD} , the ρ mesons and the like just below it, and then the three light pions far below the scale of the theory. The three pions are very close in mass and are Goldstone bosons. An exact Goldstone boson is massless due to a shift symmetry, which is related to the fact that in the UV there is a continuous global symmetry which has been spontaneously broken. It is because there does not exist an exact chiral symmetry in QCD, but rather an approximate theory in the UV, that the pions are not massless.

The general formalism for effective Lagrangians involving spontaneously broken symmetries, the Callan Coleman Wess Zumino (CCWZ) formalism which is also employed in the structure of composite Higgs models [33, 34], packages the pions as

$$\Pi = e^{i\pi_i\sigma_i/f}, \quad (1.6)$$

which arises when the breaking $SU(2)_L \times SU(2)_R \rightarrow SU(2)_V$ occurs. Notice here that each $SU(2)_X$ group has three generators, and three are ‘lost’ in the breaking, leading to three pions. The breaking may be written as a spurion m_π which explicitly breaks the axial part of the two $SU(2)$ global symmetries, where

$$\mathcal{L}_M = m_\pi^2 f_\pi^2 \text{Tr}(\Pi). \quad (1.7)$$

Again, this will be mirrored in the composite Higgs model-building in later chapters. If the axial part is only broken by a small parameter, the natural lightness of pions is explained; the shift symmetry is restored if $m_\pi \rightarrow 0$. In this sense, spurion arguments explain why the pions are naturally light compared to the UV completion of QCD.

This can be understood even without a full understanding of the UV completion. In addition, two pions are charged, and therefore interact with photons; we find another spurion e which also breaks the shift symmetry, and leads to a modification of the pion mass Lagrangian, yielding further information on the size of Λ_{QCD} .

Let us now build on this idea, turning instead to the scalar at hand; the Higgs boson. In the case of the pions, electromagnetic couplings of the charged resonances break the shift symmetry, leading to expected corrections to the charged pion mass proportional to the QED gauge coupling e . In the Higgs case, we may imagine that there is a UV

explanation for its mass of 125 GeV (and, analogously, the origin of the weak scale), much like the light scalar pions.

The Higgs Lagrangian features two gauge couplings, the quartic interaction and the Yukawa couplings with fermions which break the shift symmetry. Following the reasoning of the pion case, one may expect that the UV would feature corrections to the Higgs mass proportional to each of these parameters squared, recalling eq. (1.3). We may then expect Higgs mass corrections of the form

$$\delta m_h^2 \approx \frac{g^2}{16\pi^2} \Lambda^2. \quad (1.8)$$

A perfect analogy with the pions would imply that new physics should be just around the corner, and that Λ should be around 500 GeV. This is the exact argument used to ascertain the scale of QCD. Even if the Higgs is a pNGB, if it's going to be light and avoid getting corrections from the UV theory, we will need new physics to not be too much larger than the weak scale. This turns out to be around a TeV. If the cut-off is really far away then the corrections to the Higgs mass are large, and precise cancellation, or fine tuning, is needed to accommodate the Higgs mass that we observe today.

1.5 Extending the scalar sector

One should bear in mind that, in finding a solution to the hierarchy problem, we should be left feeling like we understand the origin of the weak scale, and we should not be thrown off by a small amount of fine tuning being required. Some moderate sensitivity to an underlying parameter should not be a reason to give up on the theory at hand; maybe we do just live in a universe which is a little bit fine tuned. When we discuss the hierarchy problem, what we are really investigating is where the weak scale came from, and whether there are microscopic dynamics that explain why EW symmetry breaking happens. The key question of the hierarchy problem is not how to regulate a loop diagram, which cannot be solved with dimensional regularisation or by choosing a different fine tuning measure. The crux of the hierarchy problem is that we are searching for something which explains the origin of the EW scale, and the origin of EWSB is at the centre of the debate around the nature of the Higgs. It is for this reason that composite Higgs studies provide an encouraging solution, as the breaking of EW symmetry is taken care of within the theory through the mechanism of vacuum misalignment which is brought about by an effective potential. These features will be expanded upon in the following chapter.

To sum up, the appearance of the Higgs boson means that the SM is now structurally complete, and this picture is not invalidated by the hierarchy problem. However, these cracks in the SM may be able to lead us in our search for more fundamental theories at higher scales. In the following thesis, we will present theoretical and experimental examinations of a number of extensions to the SM scalar sector. Extended scalar sectors offer an interesting BSM avenue, and are popular for their model building prospects. The commonalities of the BSM scalar sector will be discussed, where composite Higgs models [31, 44–46] will be the main focus, but the emergence of BSM states in the contexts of other theories will also be discussed. In a composite Higgs model, the breaking of a global symmetry leads to the appearance of resonances that are bound states of the underlying fermions [47], leading to a new spectrum of particles in the theory, some of which may be expected to appear below the TeV scale. Indeed, the examination of extensions to the scalar sector presented in this thesis will cover a number of new resonances appearing in generic composite Higgs models, including pseudo-scalar axion-like particles, vector-like quarks, and dark matter. The composite Higgs models will be implemented in this work as effective models subject to a condensation scale on the order of 1 TeV [48], examining the phenomenology of the strongly interacting theory at low energies.

We begin with an overview of the common features of composite Higgs models in chapter 2, where the focus is on models featuring underlying fermions, discussing the theoretical motivations and making mention of existing constraints. We then move to phenomenology and case studies, beginning with chapter 3 where we present an investigation into a light pseudo-scalar which appears ubiquitously in composite Higgs models of this nature. The analysis features twelve possible composite Higgs model configurations, and makes use of machine learning techniques to improve on traditional *cut-and-count* analyses on a possible search channel at a future e^+e^- collider. We then outline, in chapter 4, a more in-depth discussion of the $SU(4)/Sp(4)$ composite model scenario, including a presentation of the relevant symmetry breakings and potentials present in the theory. We also outline a phenomenological study of the η resonance at current and future colliders. Finally, we present in chapter 5 an attempt to situate a heavy dark matter candidate within a composite Higgs model in an effective way, envisioning that the dark matter candidate arises as a scalar resonance. To this end, we add to an existing model a generic dimension-five term which may be expected to appear in a number of BSM theories, and examine its impact for detection prospects. We investigate the impact of an additional vector-like top partner, a fundamental component in many composite Higgs models, on the phenomenology.

Chapter 2

The composite Higgs solution

Whether the Higgs is an elementary particle or a bound state of other fundamental particles is a complex question. As described in the previous chapter, the Higgs is included in the SM as the only elementary scalar, but extending the theory by modifying its description is a viable avenue to address some questions which are raised by its existence. Composite Higgs models [49–51] strip the Higgs boson of its elementary nature, describing it instead as a bound state by postulating the existence of a new strong sector subject to high-scale fundamental gauge dynamics. In a composite Higgs scenario, we restrict external quanta with energies larger than $1/l_{Higgs}$ to interacting with its constituents directly, rather than with the Higgs state as a whole. As a result, the Higgs mass cannot be arbitrarily raised through interactions with high energy quanta. The same mechanism appears in QCD, which was the inspiration for models featuring non-elementary Higgses.

In the SM formulation with an elementary Higgs h , the dynamics responsible for EWSB are weakly coupled, where the non-zero condensate

$$\langle h^\dagger h \rangle = v^2/2$$

breaks the EW symmetry. Alternatively, one may postulate that the breaking is due to strong dynamics. The success of QCD in describing the breaking of the $SU(2)_L \times SU(2)_R$ chiral symmetry of the up and down quarks through the formation of the $\langle \bar{q}q \rangle$ condensate below the QCD condensation scale Λ inspired the introduction of technicolour models, discussed in section 2.1. So named to invoke their connection to QCD colour, this class of models was, in essence, a scaled-up version of QCD with condensation on the order of EWSB, and featuring a scalar resonance Higgs. While

technicolour does not appear to have been nature's choice, composite Higgs models have emerged as a middle ground between the SM and a full technicolour approach. The composite Higgs models we will consider implement gauge and fermionic degrees of freedom, with a condensate forming at a scale of $f \sim 1$ TeV [52]. The theory features a global symmetry group G which acts on a manifold of scalar fields, the origin of which describes the vacuum configuration Σ_0 . This group G can be dynamically broken [3, 53] to H_1 at the scale f , which results in $n = \dim(G) - \dim(H_1)$ Nambu Goldstone Bosons (NGBs) being produced in the G/H_1 coset [44]. The coset must contain at least one $SU(2)$ doublet. We consider also the gauging by external vector bosons of some subgroup $H_0 \subset G$ [54], where the unbroken gauge group is $H = H_1 \cap H_0$. Then $n_0 = \dim(H_0) - \dim(H)$ of the Goldstone bosons are 'eaten' in order to provide longitudinal degrees of freedom to the EW gauge bosons, as in conventional EWSB. The remainder are associated with the Higgs. The breaking of global flavour symmetries due to the chiral condensate leads to the formation of a pNGB Higgs boson, along with a number of other additional states. There exist a wide variety of possibilities for a composite Higgs model, including choices for the fundamental particles (where in some models, fundamental scalars are preferred to fermions), their gauge structure, and the group structure of the theory and its associated breaking. In the following, we will discuss the origin and structure of composite Higgs models, what they aim to fix, and how they fix it. We will examine only composite Higgs models enjoying an underlying fermion structure. There will exist two phase transitions; the first occurs at a high energy scale, at which hyperfermions condense into bound composite states such as the Higgs. The second occurs at the weak scale, at which the Higgs breaks the EW symmetry by developing a vev [51], which is induced by a vacuum misalignment by both the one-loop potential due to the SM gauge bosons and the top quark, as well as bare masses for the technifermions/hyperquarks [55]. In the following, we pursue an effective field theory approach to the description of a composite Higgs model, based on a Goldstone matrix composed of broken generators of the theory, preparing for later sections where we investigate the collider phenomenology of a variety of effective models. As we will see, the description of the Higgs within a composite model not only offers a solution to the hierarchy problem, but may also naturally generate a dark matter candidate in a multitude of ways. This will be discussed further in chapter 5, where we pursue a novel approach to including dark matter within a composite Higgs model. In a famous anecdote, a scientist giving a public lecture was confronted by an elderly lady, who insisted that his view of cosmology was all wrong, and that the world rested

on the back of a giant turtle. When the scientist asked smugly what the turtle was standing on, she replied *You're very clever young man, very clever. But it's turtles all the way down.* While we may turn our noses up at this incredible theory, we can imagine the turtles to be laws of physics at higher and higher energies, or equivalently at more fundamental scales. In this thesis, we move one turtle layer down, to examine the possibility of some more fundamental physics laws operating at higher energy scales. These laws, encoded in strong dynamics, may be responsible for the behaviour of the world we see around us.

In the following, we will give a mostly qualitative discussion of composite Higgs models and their key components, offering a broad overview before diving into phenomenology in later chapters. We begin with a brief introduction to technicolour theories, outlining the inspiration for the composite Higgs models which grew out of them.

2.1 Technicolour: a precursor to compositeness

The original model replacing the Higgs sector with fundamental gauge dynamics featuring fermionic matter fields was technicolour, which breaks EW symmetry via the fermion condensate [52]. In this idea, one imagines that the confinement scale is that of $SU(2)_L \times U(1)_Y$ breaking via a condensation of *technifermions*, realising EWSB fully dynamically with no need for the Higgs mechanism [50]. Relying heavily on Goldstone's theorem, technicolour followed the pattern of QCD very closely where the condensation of the colour force dynamically breaks the $SU(2)_L \times SU(2)_R$ symmetry to its vectorial subgroup, which featured Goldstone bosons which had obtained some mass. In QCD, this occurs as the degenerate minimum of the potential in a spontaneously broken symmetry forms a valley, and the Goldstone bosons parametrise motions along this valley; they span the coset G/H [56]. Their movement is described by the broken generators (of course, the unbroken generators of G will annihilate this vacuum by definition). However, when the initial symmetry is not exact, and is originally explicitly broken by some small amount, the spontaneous breaking of this symmetry would give rise to a pNGB. Three associated pions emerge as the Goldstone bosons, and their dynamics are described by a non-linear sigma model. If one turns on the weak interactions (that is, if one gauges the theory) by allowing the QCD sector to couple to external EW fields of $SU(2)_L \times U(1)_Y$, those external fields gauge part of the global symmetry of the quarks. That is, the flavour symmetry of QCD is gauged by coupling the gauge fields to the conserved currents of QCD, but the global symmetry has been broken to a vectorial subgroup by the dynamics of QCD, so only

part of it can be gauged. This introduces an explicit breaking of the global symmetry. The mass gap between the QCD pions and the other QCD composite states then exists because the pions are pNGBs, emerging from the breaking of the approximate symmetry $SU(2)_L \times SU(2)_R$. Technicolour postulated that the Higgs boson observed at colliders was a light scalar excitation of the fermion condensate, and other scalar resonances emerging in the theory could be much heavier.

The idea of technicolour is that the sector which is responsible for EWSB is strongly interacting; the fermion condensate breaks the EW symmetry and creates the Higgs via the same process. Technicolour tried to replicate the structure of QCD, introducing technipions as pNGBs, where the longitudinal polarisations of the W and Z are a linear combination of pions and technipions. Unfortunately, the theory does not allow for a scalar doublet acquiring a vev [51], and technicolour encountered additional problems with EW precision test data, including tensions with LEP data and flavour-changing neutral current bounds [57, 58]. Instead, a compromise between the technicolour idea and simple SM solution was introduced in the form of composite Higgs models.

2.2 Composite Higgs models

In analogy with technicolour, composite Higgs models replace the SM scalar sector with one governed by strong dynamics, where fundamental fermions are subject to a confining gauge sector often labelled hypercolour, and possess a global flavour symmetry. The hypercolour group is left unbroken in the theory, but the flavour group is broken to some subgroup. These models are described in terms of gauge and fermion degrees of freedom, confining at low energies. The Higgs boson is a bound state of fermions confined by a strong gauge interaction, which condense at the characteristic confinement scale [50]. Just like in QCD and in technicolour, the flavour symmetry is dynamically broken to a subgroup through a process of condensation. In contrast to technicolour, the EW symmetry is not broken by the condensate, but rather by vacuum misalignment. The misalignment of the condensate is controlled by the parameter θ , where

$$f \sin \theta \sim v. \quad (2.1)$$

The EW symmetry is restored for $\theta = 0$, the technicolour limit is observed in $\theta = \pi/2$, and the composite Higgs structure is realised for small θ . The dynamical scale $\Lambda_{HC} \sim 4\pi f$ is generated, with f the pion decay constant.

A composite Higgs model requires that the theory contains a continuous symmetry G , over which we have some choice, and whose manifold is described locally by group generators. No matter the choice of G , a global symmetry breaking occurs at the scale f , through which the vector bosons are given mass and a Higgs boson is generated. The global symmetry group G is dynamically broken to some subgroup H , yielding broken and unbroken generators, which are respectively non-linearly and linearly realised. That the symmetry is “broken” is actually a bit misleading - the symmetry is not changed or removed, and is still present. What changes is that the symmetry does not act in the ‘normal manner’ in the coset G/H , where it instead arises as a shift symmetry of a massless NGB. For every spontaneously broken continuous symmetry, the broken generators will be accompanied by an exactly massless scalar field. The massless NGB are ‘eaten’ in order to provide longitudinal degrees of freedom to the EW gauge bosons, as in conventional EWSB (as a consequence of the fact that only a subgroup of G has been gauged). The field that contains the Goldstones is parametrised as the vev that breaks the symmetry. In the case of the Higgs, the neutral component receives a vev which spontaneously breaks $SU(2)_L$. The broken generators are then those which, when acting on the vev, do not vanish.

Of course, the Higgs boson is not massless. While exact Goldstone bosons cannot have a potential under the shift symmetry acting on them (which dictates the only couplings that we may write are derivative couplings [31]), a non-derivative operator (a potential) can emerge in the effective theory to give mass to the Goldstone bosons in the presence of operators which explicitly break the global symmetry G . This explicit breaking allows the NGBs to become pNGBs, gaining mass (just as we saw with the pions), and is also responsible for vacuum misalignment. Explicit examples of this dynamically realised scalar potential are given in chapter 4, where a case study of an $SU(4)/Sp(4)$ composite Higgs model is presented.

Given the pNGB nature of the Higgs state, we expect a mass much smaller than the confinement scale, and explicit calculations of its potential are possible (as are calculations of its vev, which also lies well below the confinement scale) [50]. That the Higgs is a pNGB is a crucial component in composite Higgs theories, as we need to be able to lower the Higgs mass to below not only Λ , the confinement scale, but also below f , the scale at which condensation of fundamental fermions leads to the formation of the Higgs [31], which characterises a composite Higgs model. The scale Λ is a dynamically generated scale on the order of 10 TeV [55]. Below this scale, the strong IR dynamics of the ψ hyperquarks break the global symmetries which lead to the creation of the composite Higgs. These breakings are acceptable when v and f of

eq. (2.1) are not too far from each other; if you require a larger hierarchy between the two, a degree of fine tuning will be unavoidable [59].

Thus from our model will emerge a massive composite bound state Higgs, which solves the hierarchy problem. That is, when virtual corrections to its mass term occur with virtual momenta in the loop larger than the bound energy, the Higgs is no longer seen as a field but as its constituents (the hyper-fermions). In other words, the tension due to naturalness is removed by allowing these quadratically diverging contributions to the Higgs mass only up to some compositeness scale [48].

In a composite Higgs model with fermionic degrees of freedom, a UV completion is possible and has been recently investigated in Refs [29, 30, 60, 61]. Alternatively, one can describe the effective theory resulting from a given composite Higgs model below the confinement scale. This is the approach that we will follow, where by defining the group structures and making minimal assumptions about the behaviour of the model we are able to constrain its parameter space. In the following, we will describe the structure and crucial components of a composite Higgs model based on an underlying fermion representation. As we follow an effective model approach which leans more towards phenomenology, we will focus more heavily on possible observables at colliders and models which will prepare us for later sections of this thesis.

2.2.1 Fermions all the way down

This work will only investigate composite Higgs models which feature an underlying fermionic construction; that is, with purely fermionic matter content subject to a simple hypercolour group. With this approach, we avoid additional pitfalls which may occur through introducing more fundamental scalars into the theory.

A composite model featuring N_f Dirac fermions of the same species may only have one of two possible global flavour symmetries G , which is dependent on the nature of the fermion representation under the hypercolour group; $SU(2N_f)$ for a (pseudo-)real fermion representation, or $SU(N_f) \times SU(N_f)$ for a complex fermion representation [48]. The pattern of the symmetry breaking of the flavour group G occurring at Λ automatically follows the definition of the fermion content, where the irreducible representation of the hypercolour group in which the fermions lie fully defines the breaking. The breaking is achieved through the bilinear condensate of the underlying fermions [62]. In a simple QCD scenario we have left handed fermions only and n pairs of fermions (ψ_i, ψ^i) in a (R, \bar{R}) complex irreducible representation breaks the global symmetry like $SU(n) \times SU(n)' \rightarrow SU(n)_D$. After condensation we are left with $\langle \tilde{\psi}^i \psi_j \rangle \propto \delta_j^i$ [55]. Considering instead n single left-handed fermions in a

(pseudo-)real representation as in a composite Higgs model, we have $SU(n) \rightarrow SO(n)$ ($SU(n) \rightarrow Sp(n)$) since the condensate $\langle \psi_i \psi_j \rangle$ is symmetric(anti-symmetric) [55]. A complete discussion regarding the reason for this structure is given in Ref. [63]. The chiral symmetry breaking in a composite Higgs model may then follow one of two patterns; $SU(N_f) \rightarrow SO(N_f)$ for a real representation, $SU(N_f) \rightarrow Sp(N_f)$ for pseudo-real, or $SU(N_f) \times SU(N_f) \rightarrow SU(N_f)$ in the case of a complex representation [64].

Model building for a composite Higgs theory necessitates the choice of global symmetries for the fermions, as well as the choice of hypercolour (or gauge) group. All models contain at least two species of underlying fermions, χ and ψ , belonging to different irreducible representations of the confining hypercolour group. The need for two different representations arises from the requirement that the top partners be able to carry both EW and colour quantum numbers. Both representations carry hypercolour. The first, ψ , generate the Higgs and carry EW charge, whereas χ carry QCD colour and hypercharge. The latter fermions are also responsible for partial compositeness, the mechanism which generates masses for the SM top quark, and which will be further discussed in sec. 2.2.3. The inclusion of partial compositeness through the coloured fermion χ puts additional constraints on the gauge and matter content of the theory [65].

The composite Higgs coset is formed via the condensation of the hyperquarks ψ of the theory. Also present is a ubiquitous non-anomalous $U(1)$ factor arising from the spontaneous breaking of the G_{HC} -anomaly-free Abelian chiral symmetry. The two axial symmetries which give rise to this are $U(1)_A^\psi$ and $U(1)_A^\chi$, and this $U(1)$ symmetry appears through a non-anomalous linear combination of the two axial $U(1)$ symmetries rotating all of the ψ and χ by the same phase. The complex irreducible representations also come with a vector-like factor $U(1)_V^\psi$ or $U(1)_V^\chi$, as in QCD, which is anomaly free and unbroken [55]. It is this $U(1)$ symmetry which gives rise to a light pseudo-scalar, a , a bound state of ψ and χ fermions which is the subject of chapter 3. The most minimal example of a composite Higgs model is the structure

$$G = SU(4) \rightarrow H = Sp(4). \quad (2.2)$$

This model contains only one additional gauge singlet η (once four degrees of freedom combine as the Higgs doublet), and may be realised through an $SU(2)$ gauge symmetry. Lattice studies have shown that this minimal set-up leads to spontaneous symmetry breaking taking place [66, 67]. We parametrise the subgroup in terms of

$SU(2)_L \times SU(2)_R$,

$$6_{SU(4)} = 5_{Sp(4)}(\text{pNGBs}) + 1_{Sp(4)}(\text{heavy scalar}),$$

where

$$5_{Sp(4)} = (2, 2)_{SO(4)}(\text{Higgs}) + (1, 1)_{SO(4)}(\text{light scalar})$$

written as $SU(2)_L \times SU(2)_R$. We will also have $U(1)$ scalars originating from the symmetries

$$\psi \rightarrow e^{i\alpha}\psi, \quad \chi \rightarrow e^{i\beta}\chi.$$

For now, we think of G_F/H_F such that $H_F \supset G_{cus} \supset G_{SM}$, where $G_{cus} = SU(3)_c \times SU(2)_L \times SU(2)_R \times U(1)_X$ such that we can write the Higgs as $(1, 2, 2)_0$. The coset G_F/H_F [60]:

$$\begin{aligned} \frac{G_F}{H_F} &= \frac{SU(4) \times SU(3) \times SU(3)' \times U(1)_X \times U(1)'}{Sp(4) \times SU(3)_c \times U(1)_X} \\ &= \frac{SU(4)}{Sp(4)} \times \frac{SU(3) \times SU(3)'}{SU(3)_c} \times U(1)', \end{aligned} \tag{2.3}$$

where the $U(1)_X$ symmetry arises for partial compositeness. This $SU(4)/Sp(4)$ coset structure will be further examined in chapter 4, where we delve into the mechanics of the model and examine some simple phenomenology for the singlet η . Further classification of the allowed cosets and most minimal models is given in Ref. [29].

2.2.2 Vacuum misalignment

We now proceed to a discussion of a core principle of composite Higgs models. Vacuum misalignment is the mechanism through which the EW symmetry is broken in a composite Higgs model, taking over from the SM Higgs mechanism. The misalignment process is driven by explicit breaking terms, and encodes a key separation from technicolour models. Given a spontaneous breaking of a general continuous symmetry, the lowest energy state corresponds to a set of minima which can be any of a number of equivalent vacua, all of which have a one-to-one correspondence with points in G/H . However, given an explicit breaking of G , the vacuum is no longer degenerate and instead selects one point in the coset space. Through the introduction of a scalar which forms at the condensation scale and behaves like the SM Higgs in its couplings to SM fermions and hyperfermions, we are able to break the EW symmetry by vacuum misalignment [49]. The coupling of the Higgs forces the hyperquark

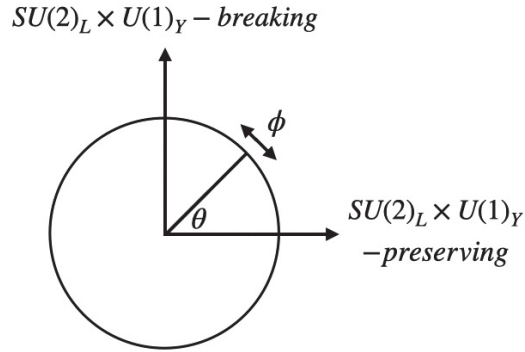


Fig. 2.1 Misalignment of the true vacuum of the composite Higgs theory with the $SU(2)_L \times U(1)_Y$ -preserving direction by an angle θ . The circle corresponds to a set of almost degenerate minima for the hyperfermion condensate, and the ϕ -field is the Higgs boson [51].

condensate to deviate (misalign!) from the $SU(2)_L \times U(1)_Y$ -preserving direction. We can then break EW symmetry far below the condensation scale [49]. In contrast, a theory featuring hyperquarks which obey the EW symmetry but have no Yukawa couplings or explicit masses would be unable to achieve the vacuum breaking $SU(2)_L \times U(1)_Y$, which is crucial for the functioning of the theory.

To construct a theory which undergoes vacuum misalignment, the representation of the fermions is chosen such that the condensate need not break the EW symmetry group. In fact, the potential of the condensate has a degenerate set of minima, some of which break $SU(2) \times U(1)$ and some that preserve it. It was proposed in Ref. [51] that we are able to lift this degeneracy such that the ground state points primarily in the direction which preserves EW symmetry, but with a small component in the breaking direction, allowing us the characteristic two scales in a composite Higgs theory, as is illustrated in fig. 2.1. We require that the EW gauge group be embeddable in H , the subgroup to which the global symmetry is broken. This ensures that whether or not the weak interactions are broken becomes a question of alignment [51], where the weak interactions are associated with a weakly gauged subgroup of the global flavour symmetry.

This misalignment can be imagined as a rotation, as illustrated in fig. 2.1, controlled by a broken generator which behaves like the Higgs doublet. The angle of rotation may be imagined as the vev of the Higgs, since pNGBs are just angular variables around the circle of nearly degenerate minima [51]. This process contributes to the potential of the theory, and therefore to the generation of the Higgs mass. By gauging not the full group G but only a subgroup of G , we are discriminating different

generators and therefore explicitly breaking the symmetry [31]. Without this gauging, the Higgs would be a true NGB. This induces a small potential, giving rise to a vev. The ability of the theory to “naturally” generate the Higgs mass allows us in turn to explain the scale of EWSB.

Clearly, the potential in a composite Higgs model is generated through a different mechanism to the SM, where in the latter case the negative μ^2 mass parameter makes the theory unstable and leads to spontaneous symmetry breaking, following which the Higgs field then acquires a vev and the Higgs phenomenon occurs. In this case, the driving force of the instability is not the negative mass term, but rather higher order effects involving virtual gauge bosons driving a loop-generated potential [68]. This loop-induced potential explicitly breaks the shift symmetry [55]. Additional contributions to the potential may emerge from mass terms for the fundamental fermions, as well as through contributions from the top quark mass. The potential will be presented and examined in more detail in chapter 4.

2.2.3 Fermion mass generation

The Higgs field performs two crucial functions in the SM; it provides the gauge bosons and the fermions with masses. As discussed previously, the generation of the gauge boson masses occurs during the gauging of the global group G , and is included in a generic composite Higgs model in a straightforward manner. The generation of fermion masses, however, emerges in a less straightforward manner. The possibility that all SM fermions are composite objects belonging to the strong sector has been all but ruled out by measurements at LEP [69], and two theories remain for the generation of fermion masses; four-fermion interactions [70] and partial compositeness [71]. In the latter, it is theorised that SM fermions appear linearly in the leading elementary-composite operator, while the former are effective terms encoding underlying strong dynamics. In much of the literature, and in this work, the strategy of partial compositeness for top mass generation is followed. The top is often regarded as ‘special’, as it possesses a mass so much heavier than those of its quark counterparts, and the ability of the top quark loop effects to naturally break EW symmetry through vacuum misalignment has been demonstrated [45]. Partial compositeness offers a solution to the challenge of generating the sizeable top mass through a mixing of elementary and composite states [72]. In this way, partial compositeness can be used to explain the disparity in fermion masses and the origin of the top mass without relying on fine tuning [55], where additional partners mix with

SM fermions ψ , separated by their chiralities [46];

$$\lambda_L \bar{\psi}_L \mathcal{O}_R + \lambda_R \bar{\psi}_R \mathcal{O}_L. \quad (2.4)$$

At low energies, the SM fermion is identified as a mixture of ψ and the lowest excitation of the composite operator; the vector-like quarks (VLQs). The fractional compositeness of the SM fermion is quantified by parameters $f_{L/R}$, which in turn depend on the above mixing matrices λ as well as the spectrum of composite fermionic resonances (their masses). The mechanism of partial compositeness requires the introduction of an additional $U(1)_X$ symmetry under which the top partners are charged [73], as included in eq. (2.3). This symmetry is inert in the symmetry breaking mechanism, but is needed in order to match the fractional hypercharges in generating the mixings of partial compositeness, where the physical mass eigenstates are superpositions between SM elementary states and fermionic resonances. The spin- $\frac{1}{2}$ top-partners are composed of fermions in two representations of the hypercolour group, of the form $\psi\chi\chi$ (or similar), and are therefore labelled chimera baryons. Given constraints on asymptotic freedom, we limit ourselves to partners for only the top quark for now [60].

Below the confinement energy the operator can excite a tower of composite states, leading to the low energy Lagrangian featuring a mixing of elementary and composite particles with Yukawa interactions. Consider a simple model where a composite singlet ψ with mass m^* couples to the third generation quark doublet q_L and the right-handed top quark, t_R . The expansion of the low energy Lagrangian pertaining to the top quark contains

$$y_L \bar{q}_L H^c \psi_R + y_R f \bar{t}_R \psi_L + h.c., \quad (2.5)$$

where diagonalisation of the masses illuminates that the right handed top quark mass eigenstate is partially composite as a mixture of both elementary and composite states with the same quantum numbers [74]

$$t_R^{SM} = \cos \phi_R t_R + \sin \phi_R \psi_R, \quad (2.6)$$

where the angle ϕ_R defines the degree of compositeness. The mass of the top quark emerges as

$$m_t \approx y_L y_R \frac{v}{\sqrt{2}} \frac{f}{m_{TP}}, \quad (2.7)$$

such that the mass of the top quark is inversely proportional to the mass of the composite resonance or top partner m_{TP} . As the top quark has the largest Yukawa

coupling, it will also be responsible for the largest source of the Goldstone symmetry breaking which pushes the Higgs vev to a non-zero value. The top quark is therefore a crucial component in the construction of the Higgs potential. Let us briefly discuss the fermionic top partners in greater detail, as they will appear in later chapters.

2.2.4 Vector-like quarks

Composite Higgs models predict the presence of a number of new states, some of which arise as pNGBs and some as bound state resonances of the underlying fermions. Of the second type are VLQs, or multiplets containing top partners of the vector-like type. The qualification “vector-like” refers to the fact that both VLQ chiralities share the same quantum numbers under the SM gauge symmetries, which is a feature not shared by the SM quarks [75], where left-handed SM quarks fall under the doublet representation of $SU(2)$, and the right-handed quarks are in the singlet representation. Instead, both the left and right handed chiralities of the VLQ belong to the same representation of the group G , where G is the SM group [76]. The non-chiral nature of VLQs mean they are subject to less stringent bounds [77], and their importance to a multitude of BSM scenarios is illustrated by the wide variety of collider searches performed in the hunt for massive vector-like fermionic states. These vector-like top partners are features in a number of BSM scenarios which address the hierarchy problem, or naturalness problem, including the ‘little Higgs’ scenario [78, 79], generic composite Higgs models [45], and modern resurrections of technicolour [80, 81]. In composite Higgs models, top partners arise as massive fermionic bound states. The decays and single production of the VLQs are generated through mixings with the SM quarks, which comes from Yukawa couplings with the Higgs, and they may then decay into massive bosons and the three SM quark generations. Two possible scenarios are envisaged for VLQs, where they may either mix and decay directly into SM quarks, or may be charged under some parity restricting their couplings. In the latter case, couplings to SM states may proceed via a mediator which may play the role of dark matter [77]. In a similar fashion, the model examined in chapter 5 outlines a case where a VLQ plays the role of mediator between dark matter and the SM. VLQs are the simplest example of coloured fermion resonances not yet excluded (unlike 4th generation quarks). They do not receive their masses from the Yukawa couplings, and are consistent with existing Higgs data. They may also introduce new sources of CP violation, which occurs in most SM extensions, and can be analysed in a model independent way.

The idea that VLQs may only couple to third generation quarks is motivated by the large Yukawa coupling of the top quark; however, model independent approaches such as Refs. [77, 76] consider the VLQs as coupling to all SM quarks. In such examples the VLQs may come as singlets, doublets, or triplets of $SU(2)$, with mass eigenstates $\{X_{5/3}, T', B', Y_{-4/3}\}$. In composite Higgs models, EWSB can then occur through the condensate of the top quark and VLQ singlet. Alternatively, we may also find explicit breaking terms in the potential. These resonances appear in the following chapters in a multitude of ways, but are primarily discussed in chapter 5, where heavy fermionic mediators feature in the theory.

2.3 Experimental constraints

Given the volume of data being achieved at experiments, BSM theories are subject to many varied constraints. In particular, composite Higgs models result not only in new resonances emerging but also in modifications of SM parameters which may be observed at experiments in cases where the confinement scale is not larger than $\Lambda \sim 10$ TeV. In these cases, the phenomena could be experimentally reached now or in the near future, with collider upgrades such as the proposed 100 TeV collider. In the case of composite models, typical processes such as Higgs production via gluon fusion and its decay to di-boson final states may be expected to be modified in comparison to the SM [82, 83]. However, given that strong constraints arise from electroweak precision tests (EWPTs) where allowed corrections to the S and T parameters severely limit BSM theories, these corrections should be expected to be marginal [84]. In fact, corrections to the EW parameters are a key reason to favour composite Higgs models over technicolour models, where embedding the full custodial group inside the subgroup H gives composite Higgs models safety from large corrections to the ρ parameter, unlike technicolour models. A more detailed description of EW constraints on composite models is available in Refs. [27, 44, 85, 86].

It should be noted also that, in composite models, corrections to the S parameter are suppressed by a factor $v^2/f^2 \ll 1$ [60]. Additionally, the mechanism of partial compositeness suppresses FCNCs and flavour violating terms, while avoiding additional fine tuning [60]. In order to satisfy EWPT constraints, strong sectors should typically have scales of roughly 3 TeV. In models such as the one examined in chapter 4, where a parameter θ controls vacuum misalignment, Higgs couplings and EWPTs require $\theta \leq 2.39$ degrees.

We have now outlined the generic qualities of a composite Higgs model, making mention of the underlying mechanisms and additional resonances which may emerge from such a theory. It is now time to turn to the phenomenological studies which we have undertaken with this theory, starting with an investigation into the light pseudo-scalar a emerging ubiquitously from fermion-constructed models of this nature.

Chapter 3

A light composite hint at future colliders

As outlined in the previous chapters, in looking to understand the hierarchy problem we are searching for the origin of the weak scale. For this, crucially, we will need high energy colliders which can improve on the performance of the LHC. A number of future colliders have been proposed, with lepton colliders viewed by many as the leading candidates, where the absence of large QCD backgrounds are favourable. Both linear colliders, such as the ILC, and circular colliders, such as the FCC, have been proposed, and each carries their advantages. Whichever set-up is chosen, the new colliders will be ‘factories’ for particles such as the Higgs, producing millions of collisions and allowing for precision measurements of its properties.

Another use for ‘factories’ such as the FCC-ee are targeted low mass searches which exploit large luminosities and minimal backgrounds at low centre of mass energies. This environment may be a perfect place to search for light, weakly coupled scalar particles which may generically appear in a composite Higgs model, or within a number of BSM theories. Extended scalar sectors featuring pseudo-scalars are of interest as they may be broadly modelled according to their properties and interactions, while featuring in many different BSM scenarios. While here we will consider the pseudo-scalar a which appears ubiquitously due to a broken $U(1)$ symmetry as a good candidate for such a search, these axion-like particles (ALPs) [87, 88] are typically very light particles which couple weakly to the SM [89]. They arise as pNGBS as a consequence of a broken global symmetry, and are therefore much lighter than the scale Λ at which couplings are generated in the effective theory. Axions were first introduced in the Peccei-Quinn mechanism [90, 91], as gauge-singlet extensions of the SM to explain the strong CP problem. In the Peccei-Quinn

mechanism a global chiral $U(1)$ symmetry is introduced and spontaneously broken through which the axion emerges as a Goldstone boson. Light ALPs of this nature may also appear in dark matter theories, as candidates [92, 93] or mediators [94–96]. Like the composite models here investigated, pNGBs may arise from the broken R-symmetry in supersymmetry [97] or through cosmic inflation [98]. This said, while a composite Higgs model will be used as a template for this analysis, the search outlined here may be translated to other ALP searches.

Generally expected to be light, the composite resonance of interest to this analysis falls within a poorly constrained area of parameter space which may be investigated through future lepton colliders. In the following, we will consider that it falls within the range $m_a \in [0, 100]$ GeV. For comparison, a search at the LHC has recently been proposed [99], where the recoil of a against initial state radiation jets was employed to target a boosted di-tau final state. In general, di-tau searches are useful for the considered ALP, as the branching ratio is usually quite large [99]. While this topology was chosen to escape the large irreducible QCD background which is present at hadron colliders, such a search for light states nonetheless poses a problem at hadron colliders. For this reason, we turn to future lepton colliders, considering both linear and circular colliders, until settling on a case study featuring the FCC-ee collider. The relative deficiency of LHC searches in lower mass regions thus far means that the presence of this light ALP is not yet excluded [48]. This analysis is significant given that it may complement existing low-mass resonance searches at the LHC, including di-jet [100, 101], di-muon [102, 103], di-photon [104–106] and di-tau [107] searches which have been performed in recent years. These searches yield poor constraints in the low ALP mass regions, where it has been shown that the sole constraint on the decay constant of this light resonance is the Higgs to BSM branching ratio [48]. Masses $m_a < 10$ GeV are ignored, due to strong experimental bounds [99]. Additionally, the associated results rely on older cross section predictions, ignoring bottom-quark loop effects.

The proof for extension of the scalar sector through the realisation of the Higgs boson as a composite object will likely not come through direct observations of the Higgs itself. Rather, the first signs of compositeness may emerge instead through the detection of light states, such as a , which are produced in conjunction with the Higgs boson. Also a pNGB, the ALP is expected to be light enough to be visible at future colliders, and could be the first of the composite Higgs zoo to be detected.

In defining the composite Higgs model from which the a emerges, we are faced with a number of choices for the hypercolour group, global symmetry group of the fermions,

and gauge group of the theory. As outlined in the previous chapter, many options exist for these group structures. In order to be as general as possible but also to make specific predictions, we have chosen to explore twelve possible models that have recently been proposed as the most minimal options for a composite high-scale dynamics, and where each features fundamental fermions in its new strong sector [29]. Notably, the models feature partial compositeness for top mass generation [71]. A striking and useful feature of these models is that, once the choices of groups have been made, the coefficients are completely determined, laying the base for an investigation into the phenomenology. The key features of each of the twelve models are given in table 3.1, where the representations of each of the fermion species and their corresponding cosets are outlined.

As discussed in the preceding chapter, a ubiquitous feature of these twelve models which feature partial compositeness is the appearance of additional pNGBs arising from the broken $U(1)$ axial symmetries associated to the two fermion irreducible representations. The two $U(1)$ axial symmetries emerge from the full symmetry breaking pattern, where one combination of the symmetries will be non-anomalous with respect to the confining hypercolour group [64], in this case resulting in two new resonances. One is expected to be very heavy, and the other very light (lighter than the confinement scale). This contrasts with the anomalous axial current in QCD. The lighter of the two, a , would be in essence a composite axion [108].

Axions of this nature are favoured in BSM models as they address an additional thorn in the side of SM: the strong CP problem. This phenomenon concerns the breaking of charge-conjugation parity (CP) symmetry via the strong interaction, which has never been observed experimentally although the term is allowed under SM symmetries. It arises because the following interaction breaks CP symmetry and arises in the SM,

$$\mathcal{L} = \theta \frac{g^2}{32\pi^2} \epsilon_{\mu\nu\alpha\beta} G_{\mu\nu}^a G_a^{\alpha\beta}. \quad (3.1)$$

Here, θ is some constant number which takes angular values, g is the QCD gauge coupling, ϵ is the fully antisymmetric tensor, and G is the field strengths of the gluons. The appearance of this term in the Lagrangian but not at experiment teaches us that sometimes a classical symmetry is not a quantum symmetry, or vice versa. True axions, which appear widely in the literature as a solution to the strong CP problem, should feature derivative couplings such that they respect the shift symmetry. In general axions are very weakly coupled so the only way to look for them is in high luminosity

M	HC	Coset	ψ	χ	$-q_\chi/q_\psi$
1	$SO(7)$	$\frac{SU(5)}{SO(5)} \times \frac{SU(6)}{SO(6)}$	$5 \times \mathbf{F}$	$6 \times \mathbf{Sp}$	5/6
2	$SO(9)$				5/12
3	$SO(7)$	$\frac{SU(5)}{SO(5)} \times \frac{SU(6)}{SO(6)}$	$5 \times \mathbf{Sp}$	$6 \times \mathbf{F}$	5/6
4	$SO(9)$				5/3
5	$Sp(4)$	$\frac{SU(5)}{SO(5)} \times \frac{SU(6)}{SO(6)}$	$5 \times \mathbf{A}_2$	$6 \times \mathbf{F}$	5/3
6	$SU(4)$	$\frac{SU(5)}{SO(5)} \times \frac{SU(3)^2}{SU(3)}$	$5 \times \mathbf{A}_2$	$3 \times (\mathbf{F}, \bar{\mathbf{F}})$	5/3
7	$SO(10)$		$5 \times \mathbf{F}$	$3 \times (\mathbf{Sp}, \bar{\mathbf{Sp}})$	5/12
8	$Sp(4)$	$\frac{SU(4)}{Sp(4)} \times \frac{SU(6)}{SO(6)}$	$4 \times \mathbf{F}_2$	$6 \times \mathbf{A}_2$	1/3
9	$SO(11)$		$4 \times \mathbf{Sp}$	$6 \times \mathbf{F}$,	8/3
10	$SO(10)$	$\frac{SU(4)^2}{SU(4)} \times \frac{SU(6)}{SO(6)}$	$4 \times (\mathbf{Sp}, \bar{\mathbf{Sp}})$	$6 \times \mathbf{F}$	8/3
11	$SU(4)$		$4 \times (\mathbf{F}, \bar{\mathbf{F}})$	$6 \times \mathbf{A}_2$	2/3
12	$SU(5)$	$\frac{SU(4)^2}{SU(4)} \times \frac{SU(3)^2}{SU(3)}$	$4 \times (\mathbf{F}, \bar{\mathbf{F}})$	$3 \times (\mathbf{A}_2, \bar{\mathbf{A}}_2)$	4/9

Table 3.1 The features of the models studied in this work are presented here, and described further in Refs. [48, 64, 99]. We name the models M1-M12, as indicated in the first column. The following columns indicate the confining hypercolour gauge group, the EW and QCD cosets, and the representations under the hypercolour group of the fermions ψ and χ which define the coset choice. The final column indicates the charges of the fermions under the non-anomalous $U(1)$ charge in each sector.

experiments. The SM alone can not accommodate the axion, which means that there must be an additional scalar present to break the $U(1)$ symmetry in the theory. In the following, we have constructed an analysis targeting a low mass search for such a resonance. We begin by describing the effective model constructed from a generic composite Higgs model, outlining the emergence of the light ALP, and defining its Lagrangians and couplings. Particular attention is paid to its couplings to gauge bosons, proceeding via a Wess-Zumino-Witten (WZW) anomaly [109, 110], which presents as an effective vertex, combined with a SM quark loop contribution. We will investigate modifications to phenomenology due to the inclusion of bottom quarks in these vertices, maintaining a general approach which is applicable across all colliders. We then move to an investigation of the phenomenology, considering a variety of future colliders, ultimately focusing on the FCC-ee as a case study for a ALP production mode featuring full leading order couplings to gauge bosons, i.e. including effects originating from loops of b quarks. Finally, we compare the use of a machine learning algorithm with traditional cut-and-count methods, displaying the utility of multivariate approaches for hard to reach signal regions such as those encountered here.

3.1 Singlet axial symmetry

Before motivating the appearance of this ALP in the effective model, let us first examine the form of the $U(1)$ symmetry from which it emerges. $U(1)$ symmetries encode a rotation in the complex plane, where fermions ψ and $\bar{\psi}$ share the same $U(1)$ charge because they transform in the same manner. Applying a flavour-singlet axial rotation to fermions in the theory results in the transformation [63] $\psi_i \rightarrow e^{-\theta\gamma_5}\psi_i$, and $\bar{\psi}_i \rightarrow \bar{\psi}_i e^{-\theta\gamma_5}$. The corresponding $U(1)_A$ current is [63]

$$A_\mu = \sum_{i=1}^N \bar{\psi}_i \gamma_\mu \gamma_5 \psi_i, \quad (3.2)$$

and similarly for Majorana fermions. The individual $U(1)_A$ currents are anomalous; however, out of two flavour singlet axial currents we can make one which is anomaly free. We write the non-anomalous current as [63] $A_\mu = \sum_r q_r A_{r,\mu}$. The axial charges of the two irreducible representations are defined by their generators and the number of fermions. The requirement that the current be anomaly-free fixes the ratio q_1/q_2 . For each irreducible representation the fermion condensate then carries twice the axial charge of a single field, which leads to the spontaneous breaking of the non-anomalous

$U(1)_A$ too. We therefore have an additional NBG, for which we introduce a new effective field [63]

$$\Phi(x) = \exp\left(\frac{i\xi(x)}{\sqrt{2}F_\xi}\right), \quad (3.3)$$

with covariant derivative

$$D_\mu\Phi = \partial_\mu\Phi + i\alpha_\mu\Phi = i\Phi\left(\frac{\partial_\mu\xi}{\sqrt{2}F_\xi} + \alpha_\mu\right). \quad (3.4)$$

Axions emerging from such a symmetry are a predictive solution to a difficult problem and so have been a prominent part of BSM theories for decades. In the following, we present a search for an axion-like particle which emerges generically from composite Higgs models.

3.2 Effective model

The model featuring the resonance a of interest is constructed from each of the set-ups described in table 3.1. The ALP is a singlet under all SM gauge symmetries, and its interactions are described by the effective Lagrangian [99]

$$\begin{aligned} \mathcal{L} = & \frac{1}{2}(\partial_\mu a)(\partial^\mu a) - \frac{1}{2}m_a^2 a^2 - \sum_f \frac{iC_f m_f}{f_a} a \bar{\Psi}_f \gamma^5 \Psi_f + \\ & \frac{g_s^2 \kappa_g a}{16\pi^2 f_a} G_{\mu\nu}^a \tilde{G}^{a\mu\nu} + \frac{g^2 \kappa_W a}{16\pi^2 f_a} W_{\mu\nu}^i \tilde{W}^{i\mu\nu} + \frac{g'^2 \kappa_B a}{16\pi^2 f_a} B_{\mu\nu} \tilde{B}^{\mu\nu}, \end{aligned} \quad (3.5)$$

featuring interactions with SM fermions proportional to their masses m_f and including a factor of $1/f_a$, where the decay constant f_a parametrises the relevant scale.

Couplings to all SM particles are included as the ψ and χ fermions in the a bound state carry both EW and colour charges. The anomalous couplings to gauge bosons includes both a BSM effective coupling with associated parameter κ_x and an additional coupling facilitated through a loop of SM quarks not included in the Lagrangian. The couplings to fermions and gauge bosons are parametrised by coefficients C_f and κ_V which are fully determined for each model, and are given in table 3.2. The coupling of the top quark, C_t , may depend on the representation chosen for the top partner under partial compositeness. In this study we have followed Ref. [99] and considered $C_t = C_f$. The BSM couplings to gauge bosons proceed through the WZW anomaly, and are therefore parametrised by effective coefficients. These couplings arise as a result of anomalies present in non-linear sigma models, and

	M1	M2	M3	M4	M5	M6	M7	M8	M9	M10	M11	M12
κ_g	-7.2	-8.7	-6.3	-11.	-4.9	-4.9	-8.7	-1.6	-10	-9.4	-3.3	-4.1
κ_W	7.6	12.	8.7	12.	3.6	4.4	13.	1.9	5.6	5.6	3.3	4.6
κ_B	2.8	5.9	-8.2	-17.	0.4	1.1	7.3	-2.3	-22.	-19.	-5.5	-6.3
C_f	2.2	2.6	2.2	1.5	1.5	1.5	2.6	1.9	0.7	0.7	1.7	1.8

Table 3.2 Couplings of the ALP to gauge bosons (κ_V) and fermions (C_f) in the twelve models of interest used as benchmarks in this study [99].

are strongly dependent on the UV structure of the model. Previous implementations of this class of theories [48, 99] have included loops of SM top quarks in such vertices, where lighter quarks running in the loops were considered to be negligible. In this work, we have considered both top and bottom quark contributions, which is shown to provide a non-negligible impact particularly for lower masses of a .

Additional couplings to the Higgs and Z bosons are included at loop level. The decay constant for the ALP a , defined as

$$f_a = \sqrt{\frac{q_\psi^2 N_\psi f_\psi^2 + q_\chi^2 N_\chi f_\chi^2}{q_\psi^2 + q_\chi^2}}, \quad (3.6)$$

was set at 1 TeV for this analysis. Here, $N_{\psi,\chi}$ denotes the multiplicity of the fermions, and $q_{\psi,\chi}$ their charges. The decay constants in each sector are indicated by $f_{\psi,\chi}$. The coupling of the ALP to SM particles is suppressed by a factor f_a , determining how weakly a interacts. In fact, the coupling term for a SM fermion Ψ is written

$$\mathcal{L} \supset \sum_f \frac{iC_f m_f}{f_a} a \bar{\Psi}_f \gamma^5 \Psi_f \Phi, \quad (3.7)$$

where Φ is the Higgs field, needed for gauge invariance and including couplings to the Higgs boson. In order to access each gauge-ALP vertex, we can rewrite the interaction Lagrangian in terms of the physical gauge bosons such that [48]

$$\mathcal{L}_{gauge} \supset \frac{a}{16\pi^2 f_a} \left(g_s^2 \kappa_g G_{\mu\nu} \tilde{G}^{\mu\nu} + g^2 \kappa_{WW} W_{\mu\nu}^+ \tilde{W}^{-\mu\nu} + e^2 \kappa_{\gamma\gamma} F_{\mu\nu} \tilde{F}^{\mu\nu} + \frac{e^2}{s_W^2 c_W^2} \kappa_{ZZ} Z_{\mu\nu} \tilde{Z}^{\mu\nu} + \frac{2e^2}{s_W c_W} \kappa_{Z\gamma} F_{\mu\nu} \tilde{Z}^{\mu\nu} \right), \quad (3.8)$$

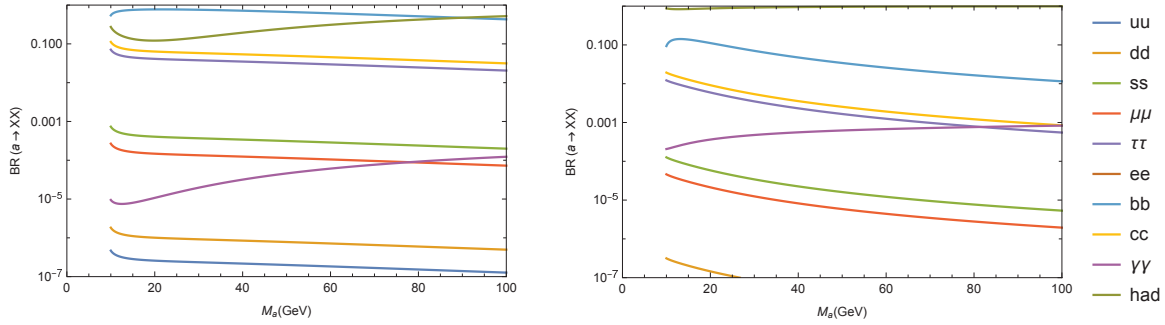


Fig. 3.1 Branching ratios of a for M8 (left) and M9 (right), which both feature the $SU(4)/Sp(4)$ coset.

where the couplings are written as

$$\begin{aligned}
 \kappa_{\gamma\gamma} &= \kappa_W + \kappa_B, \\
 \kappa_{Z\gamma} &= c_W^2 \kappa_W - s_W^2 \kappa_B, \\
 \kappa_{ZZ} &= c_W^4 \kappa_W + s_W^4 \kappa_B.
 \end{aligned}
 \tag{3.9}$$

Given the coupling of the ALP to all families of fermions, many decay chains are possible. The full spread of branching ratios is visible in fig. 3.1, which shows models M8 and M9, both of which feature the ψ flavour coset $SU(4)/Sp(4)$, and differ in their hypercolour group. The variation across models is evident, even when featuring the same EW coset structure. Given that the fermion couplings are proportional to masses, the heavier decay channel candidates result in the largest branching ratios. Branchings to hadrons are also significant. Irreducible background due to QCD effects at colliders make signals featuring low mass quarks and hadrons difficult to identify. In order to avoid having to isolate low energy jets, di-tau signals are considered a more favourable and achievable option.

In order to examine the phenomenology of the ALP at both hadron and lepton colliders, we have constructed a new FeynRules [111] implementation of a to full leading order, following the Lagrangian construction in eq. (3.5). In the following, we begin by investigating the modifications to the phenomenology through the introduction of b quarks into the triangle diagrams, following which we begin the investigation into the phenomenology at colliders.

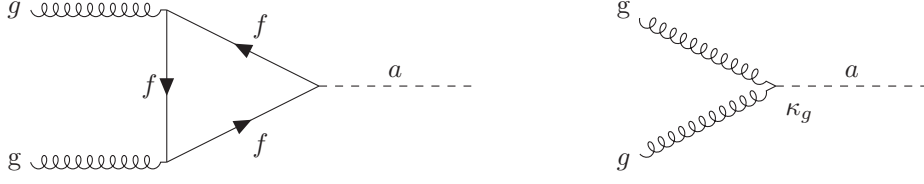


Fig. 3.2 The SM (left) and BSM (right) components of the ALP coupling to a pair of gluons featuring a loop of SM quarks and an effective vertex respectively, which is expected to be the dominant production mechanism at hadron colliders. The BSM vertex features an effective WZW structure, as given in eq. (3.5).

3.2.1 b -quark effects

The couplings of the ALP to gauge bosons V, V' , which may or may not be different species, proceed via a combination of BSM and SM vertices. As shown in fig. 3.2 where gluon couplings serve as an example, the right-hand case features the ALP coupling directly to the gauge bosons, parametrised by the WZW effective coupling κ_g which is fully determined by the model at hand. These couplings are included in the Lagrangian given in eq. (3.8). In the left-hand case, the ALP couples via a loop of SM quarks. While it has previously been assumed that only the top quark was heavy enough to warrant being included, we will in this section show that the inclusion of the bottom quark loop in couplings to gauge bosons considerably modifies the associated phenomenology, the accuracy of which is essential for low mass searches. The process is similar to that of Higgs production. This is the case for all gauge boson-ALP interactions which may be extracted from the Lagrangian, including (gga , $\gamma\gamma a$, ZZa , W^+W^-a and $Z\gamma a$).

As an example, we examine the gga vertex where the ALP couples to gluons, and calculate the partonic gluon-fusion production cross section of a ALP,

$$\sigma_0 = \frac{1}{256\pi f_a^2} \frac{g_s^4}{16\pi^2} \left| \kappa_g + \sum_f A(\tau_f) \right|^2 \quad \text{with} \quad \tau_f = \frac{4m_f^2}{m_a^2}. \quad (3.10)$$

This expression for σ_0 includes the anomaly contribution which is proportional to κ_g , as well as the sum over the contributions from each fermion considered, here including the top and bottom quarks. The function $A(\tau)$ is defined for a fermion f by

$$A(\tau) = \tau \begin{cases} -\frac{1}{4} \left[\log \frac{1+\sqrt{1-\tau}}{1-\sqrt{1-\tau}} - i\pi \right]^2 & \text{if } \tau < 1, \\ \arcsin^2\left(\frac{1}{\sqrt{\tau}}\right) & \text{if } \tau \geq 1, \end{cases} \quad (3.11)$$

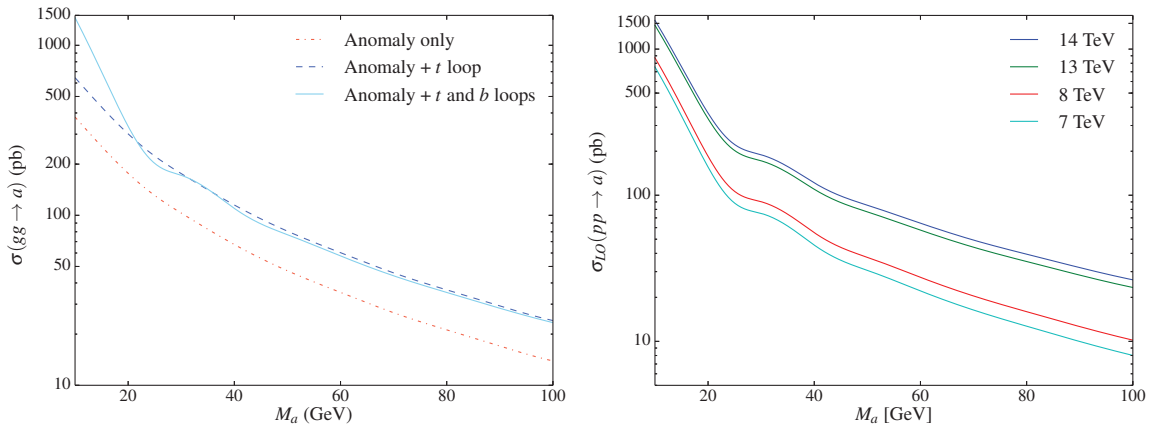


Fig. 3.3 Gluon fusion production cross section at the LHC showing contributions due to the anomaly and additional top loops in the gluon vertex (left) and showing the inclusion of both t and b quarks in conjunction with the anomaly for a variety of LHC energies (right).

whose form is due to the three-point scalar function of the quark loop propagator. The cases of eq. (3.11) for top quarks and bottom quarks are handled separately, with $\tau_t \geq 1$ and $\tau_b < 1$. In the top quark case, $A(\tau_t)$ is approximately constant (≈ 1) across the mass range m_a here considered. The resulting approximately constant increase in production cross section is presented in fig. 3.3. In this figure, we convolute the cross section of eq. (3.10) with a leading order set of NNPDF 2.3 parton densities NNPDF23_lo_as_0130_qed [112] with $m_a \in [10, 100]$ GeV. Along with the cross section of eq. (3.10), fig. 3.3 shows its modification due to the inclusion of the b quarks, where the presence of logarithms produces an undulation in the behaviour. Here, interplay between real and imaginary components yields the observed behaviour. A small decrease in the cross section is evident at higher masses due to destructive interference between top and bottom contributions. The figure also plainly displays the approximately constant increase in the cross section due to the top loop inclusion, but that the modifications due to the bottom quark are only significant for lower masses. We include only the effects due to the b quark and neglect all lighter quarks and all leptons, as their contributions are suppressed by their masses. This choice is supported by the observation that the c quark with mass $m_c = 1.275$ GeV, would impact the cross section at most by the effect the b quark has at $m_a \approx 33$ GeV in fig. 3.3 (left), due to the form of $A(\tau)$ for small τ . Given this effect can be judged as negligible by inspection, we can safely ignore the lighter quarks.

Additionally, we examine modifications to the branching ratios arising from the inclusion of the bottom and top quarks. Figures 3.4 and 3.5 detail the modifications to

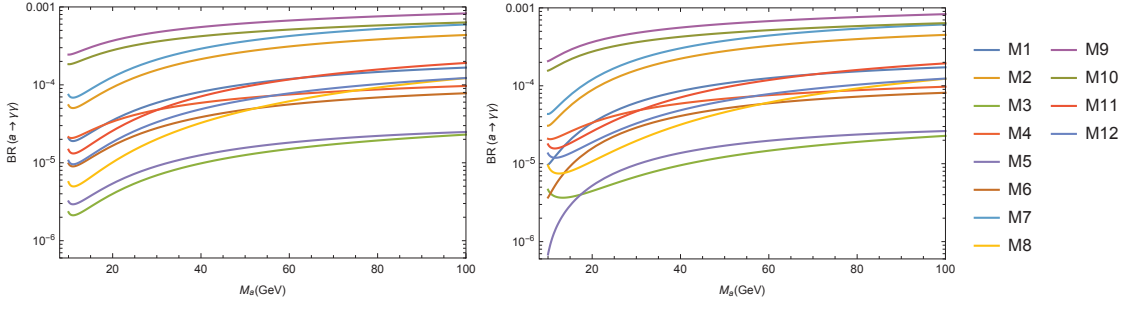


Fig. 3.4 Branching ratios of a to photons for each model without b quarks (left) and with both t and b quarks (right).

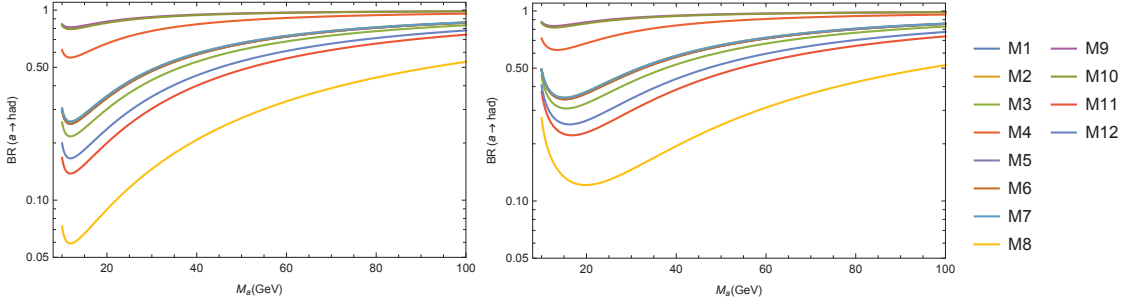


Fig. 3.5 Branching ratios of a to hadrons for each model without b quarks (left) and with both t and b quarks (right).

the di- γ and hadronic final states, where clear b -induced modifications are visible. In particular, modifications at lower masses are particularly evident, where the ‘flick’ upwards in the hadron branching ratio, present due to proximity to the $B\bar{B}$ threshold, is accentuated.

3.3 Collider phenomenology

A light ALP may be produced both at hadron and lepton colliders, where the production mechanisms will of course differ. At hadron colliders, gluon fusion is the dominant process through which production would occur. Currently, the ALP is expected to be produced at the LHC, and production will increase when the LHC begins its scheduled high luminosity run. The relevant diagrams for hadron collider production are illustrated in fig. 3.2, featuring a SM (that is, featuring SM quarks) and BSM component which should be summed for full gluon fusion production. As shown in the previous section, the two heaviest quarks should be summed in the SM

contribution to be added to the WZW term. In fig. 3.3 (right), the production of the ALP $gg \rightarrow a$ is presented including both quark species and the anomaly. Energies of Runs 1, 2, 3, and HL-LHC are displayed, and the oscillation as discussed in the previous section is clearly visible.

For reasons outlined in earlier sections, lepton colliders offer an attractive alternative to hadron colliders when searching for light weakly coupled resonances, as their high luminosities make searches for rare particles more achievable. In the following, we consider production at a number of future lepton colliders, choosing to focus on production modes featuring gauge boson interactions. Finally, we settle on the FCC-ee operating at the Z pole as a viable option, constructing a potential search for a low mass ALP.

3.3.1 Future lepton colliders

The production of the light a at lepton colliders differs significantly from production at hadron colliders. As the leptons are not coloured objects, gluon fusion is no longer the production mechanism, and the ALP may instead be produced in association with a neutral gauge boson. Relevant diagrams for this process are presented in fig. 3.6, where s -channel and t -channel diagrams may both be relevant. In the figure we include the gauge boson decay into a fermion-anti-fermion pair in the first line. The second line depicts extra non-resonant diagrams. The first two diagrams denote the SM and BSM components of the same process. The production of the ALP therefore includes contributions from the Z and γ channels, as well as the interference between them. Two channels are identified, to be considered separately, where a may be produced accompanied either by a pair of leptons or a pair of light jets,

$$e^+e^- \rightarrow \ell^+\ell^-a, \quad e^+e^- \rightarrow jj a. \quad (3.12)$$

Here, we require that $\ell = e, \mu$ and the jets do not originate from the fragmentation of a b quark. This strategy is designed to handle contributions from the Z, γ and any interference between them, as well as considering additional diagrams which may contribute.

In proceeding towards the collider phenomenology, we check the production cross section for our processes at each of the aforementioned future lepton colliders. Linear lepton colliders, such as the ILC and CLIC, offer benefits of beam polarisation, where chirality-dependent processes may be amplified. Circular colliders allow for an accumulation of larger luminosities, which is crucial when searching for timidly

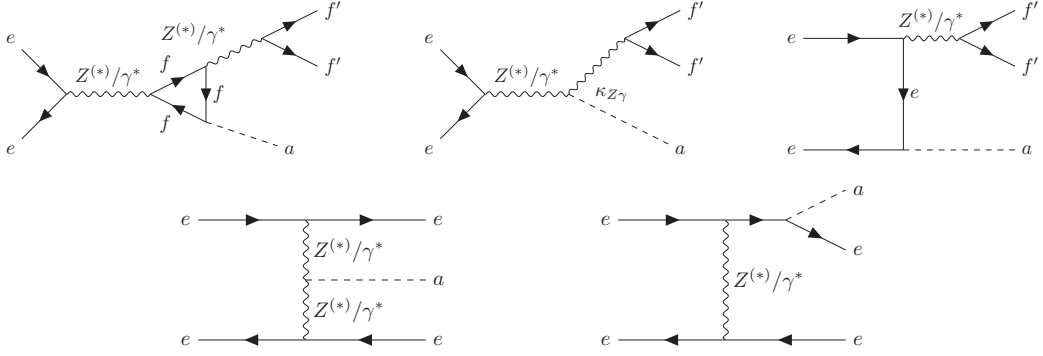


Fig. 3.6 Feynman diagrams, including both SM and BSM processes, showing the production of an ALP in association with a virtual photon or with a (virtual or real) Z -boson.

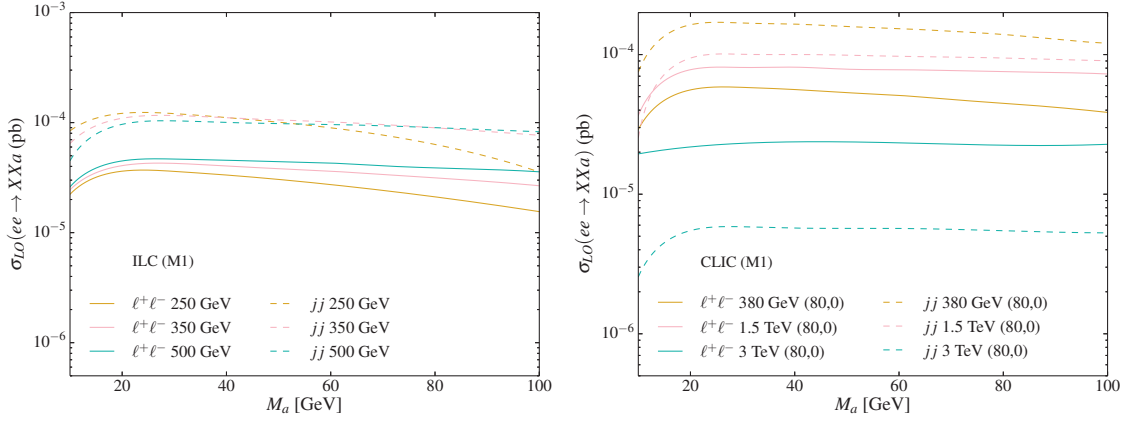


Fig. 3.7 Total leading order cross section for the production of the ALP a in association with a pair of leptons (solid lines) or jets (dashed lines) at the ILC and CLIC, for various centre of mass energies, where beam polarisations are included where relevant.

coupled particles such as a , but suffer from energy loss due to large Bremsstrahlung effects. The proposed collision energies and polarisations, where relevant, are presented in table 3.3, and we plot the production cross sections for the processes in eq. (3.12) in each case in figs. 3.7 and 3.8. In the cases where a number of polarisations are possible, we choose a sample, as no appreciable change for the production cross section was detected across polarisations.

Displaying the linear colliders in fig. 3.7 and the circular colliders in fig. 3.8, we rely on model M1 as a benchmark, and show leading order production of the ALP with leptons(jets) in solid(dashed) lines. The results include basic selections on the final

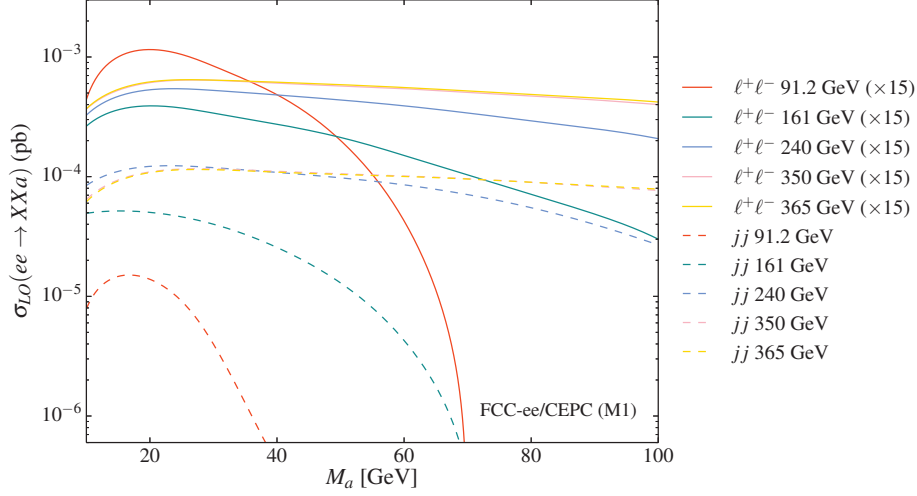


Fig. 3.8 Same as in fig. 3.7, but for the FCC-ee and CEPC circular colliders, where the production with leptons was multiplied by 15 for clearer observation.

state transverse momenta p_T and pseudorapidity η

$$p_T(j) > 20 \text{ GeV} , \quad |\eta(j)| < 5 ; \quad p_T(\ell) > 5 \text{ GeV} , \quad |\eta(\ell)| < 2.5 . \quad (3.13)$$

Additional requirements are placed on the angular separation ΔR of jets and leptons in the transverse plane, with

$$\Delta R(\ell, \ell') > 0.4 , \quad \Delta R(j, j') > 0.4 . \quad (3.14)$$

The centre of mass energies of the linear colliders all lie well above m_a , and the production cross sections display relatively constant behaviour across the considered mass range. The behaviour is modified in the case of the lower centre of mass energies in the circular colliders, where the production cross section dips sharply with the reduction in available phase space. However, the production at circular colliders at the Z pole, where a is produced with leptons, is found to be more attractive than the association with jets. For lower m_a , the cross section is larger than for higher centre of mass energies due to the resonant production of Z bosons. The large integrated luminosity predicted at this collision energy at the FCC, coupled with the minimal backgrounds expected at such a low centre of mass energy (where top and WW backgrounds will not feature) makes this an attractive prospect. Although the expected production falls off sharply from around 60 GeV, we are content to examine the mass range $m_a \in [10, 60]$ GeV.

Collider	Energy (GeV)	Int. Lumi (ab^{-1})	Pol. (%)
CEPC	91.2	8	-
	161	2.6	-
	240	5.6	-
FCC-ee	91.2	150	-
	161	10	-
	240	5	-
	350	0.2	-
	365	1.5	-
ILC	250	2	-
		1	(80,0)
		1	(-80,0)
		0.9	(-80,30)
		0.9	(80,-30)
	350	0.2	-
		0.05	(80,0)
		0.15	(-80,0)
		0.135	(-80,30)
	500	0.045	(80,-30)
		4	-
		2	(80,0)
		2	(-80,0)
CLIC	1500	1.6	(-80,30)
		1.6	(80,-30)
	3000	2	(-80,0)
		0.5	(80,0)
3000	4	(-80,0)	
	1	(80,0)	

Table 3.3 The variety of centre of mass energies and corresponding integrated luminosities over a number of proposed circular and linear future lepton colliders, including polarisations in the final column of the table where applicable [42].

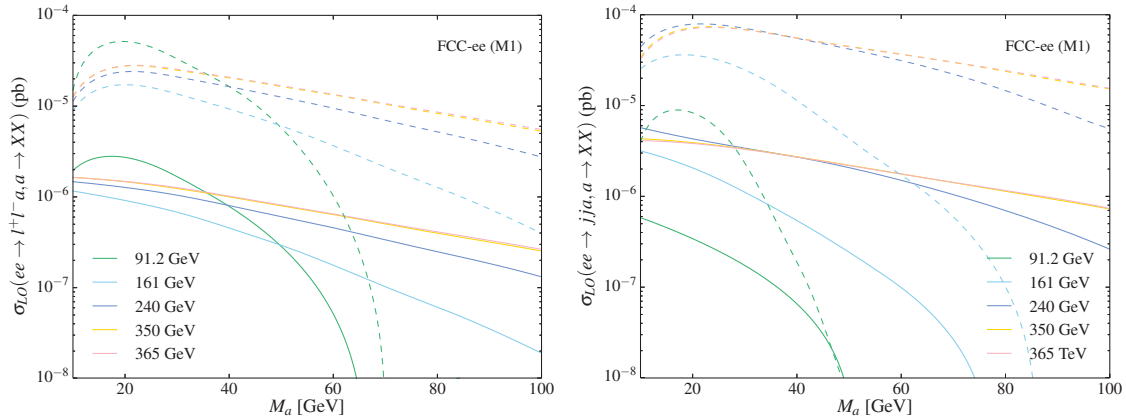


Fig. 3.9 Leading order cross sections including decays to $b\bar{b}$ (dashed) and $\tau^+\tau^-$ (solid).

Recalling fig. 3.1, branching ratios of a are highest to $\tau^+\tau^-$ or $b\bar{b}$ pairs, or jets originating from quarks, as the coupling of the ALP to fermions depends on the fermion mass. Following the production of the ALP in association with leptons or jets, a choice must be made as to whether we consider $a \rightarrow b\bar{b}$ or $a \rightarrow \tau^+\tau^-$ decays for our analysis. These decay modes are chosen for initial consideration due to their abundance, while still being reasonable final states in designing an analysis, as final states which rely on jets as a signal present difficulties at lower mass ranges due to possible convolutions with QCD backgrounds. In the following, we will refer to the search channels as $\ell\ell\tau\tau$, $\ell\ell b\bar{b}$, $jj\tau\tau$ or $jjb\bar{b}$. In fig. 3.9, we show the relevant expected cross sections for each decay mode.

While the production to $b\bar{b}$ is clearly more prolific, the signatures from the tau decay are a preferred final state to b -jets. In fig. 3.10, we present the number of expected hadronic and leptonic tau decays resulting from the production in association with leptons at the Z pole,

$$e^+e^- \rightarrow \ell^+\ell^-a \rightarrow \ell^+\ell^-\tau^+\tau^- . \quad (3.15)$$

Statistical error bars are indicated. Though the numbers vary across models, and the fall off for higher masses is evident, a significant number of new physics events may be expected, motivating our choice of search strategy. From here onwards, we focus our attention on the future collider proposed by the FCC-ee committee [40], featuring 150 ab^{-1} at the Z -pole, and choosing to tackle the hadronic tau final state.

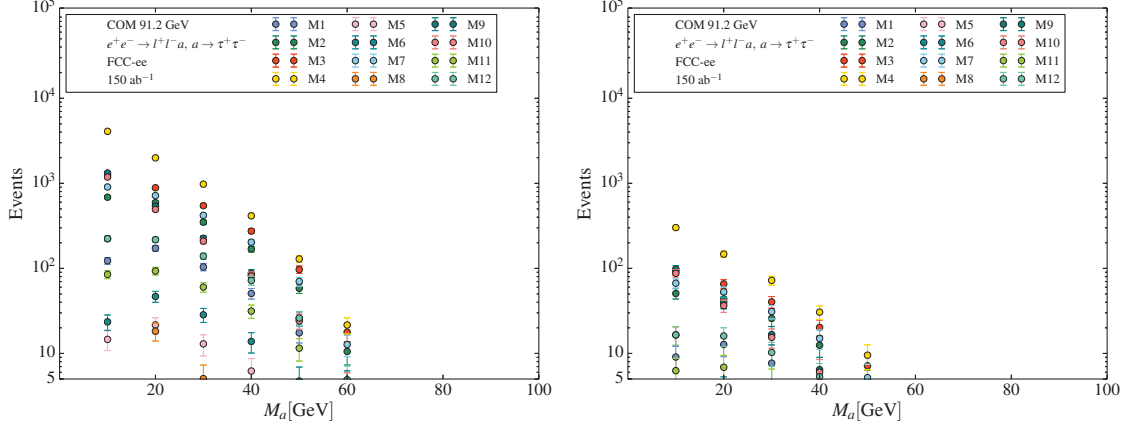


Fig. 3.10 The total number of $\ell\ell\tau\tau$ signal events that may be expected in 150 ab^{-1} of e^+e^- collisions at the Z -pole, where each of the 12 benchmark models are displayed, including hadronic decays of the τ lepton (left) and leptonic decays (right).

3.3.2 An FCC-ee case study

We proceed by simulating events at the FCC-ee collider for use in an analysis, where we include the IDEA detector concept for detector parametrisation. This is achieved using the MADGRAPH5_AMC@NLO (MG5_AMC) framework [113] for the calculation of predictions at colliders for both the signal and background processes. The UFO model files [114] for use with MG5_AMC have been created using the FEYNRULES [111] package. The simulation of collision events and reconstruction has been done in conjunction with the DELPHES 3 [115] software package, that includes the anti- k_T algorithm [116] as implemented in FASTJET 3 [117] for event reconstruction, and with PYTHIA 8 [118] to describe parton showering and hadronisation. Both latter codes are utilised through their interface with MADANALYSIS 5 [119, 120], that will be later employed for the phenomenological analysis.

In considering the background processes relevant to this analysis, we identify two classes thereof; processes leading to a true $\ell\ell\tau\tau$ background, and those leading to fakes. In the first case, we are likely to encounter true tau final states through the production of one or more Z bosons in association with a pair of leptons, as illustrated in fig. 3.11. Conversely, background events featuring fakes arise from jets misidentified as taus, appearing in events where the leptonic decay of a boson occurs with a pair of jets, including virtual production,

$$e^+e^- \rightarrow jj\ell^+\ell^- . \quad (3.16)$$

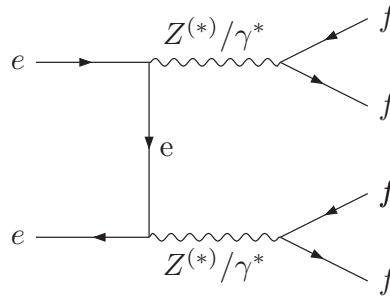


Fig. 3.11 Di-boson background relevant to this analysis, including decays to fermion pairs.

This background, referred to as Z +jets, covers virtual photons and interferences too. The corresponding cross section is 6.65×10^{-4} pb, which should then be multiplied by a fake factor characteristic of the detector. The DELPHES IDEA detector includes a 0.1% misidentification rate for jets faking hadronic taus and a tau identification efficiency of 60%. This leads to a ‘fake’ contribution on the order of 10^{-10} pb, which we safely ignore.

3.3.3 Testing a signal hypothesis

Before proceeding with the outline of the analysis, we take a brief interlude to outline the structure of a generic hypothesis test which forms the basis for a physics analysis, the type of which will be followed below and in later chapters. A high energy physics analysis is performed by separating signal events, whose number is denoted by s and which are characteristic of the process of interest, from background events b , which mimic the signal but arise from different processes. One performs a hypothesis test by comparing two cases; the existence of both signal and background, or background only. The goal is to test, and try to reject, the hypothesis that $s = 0$; that is, that the signal is not present. The outcome of the test is statistically significant if, according to a significance level, it would be unlikely to occur if the null hypothesis were true. The events will follow a Poisson distribution with a mean $n = s + b$, where the background-only hypothesis is rejected if $n \gg b$ [121]. In the design phase of an analysis, the expected number of background and signal events are estimated using Monte Carlo simulations. In order to quantify the significance of the discovery via rejection of the background-only hypothesis, the fluctuation Z of a standard Gaussian variable can be quoted. In the large b and small s limit, one can approximate $Z \sim s/\sqrt{b}$. In planning a statistical analysis in a particle physics setting, the aim is to

maximise the discovery significance for a given signal on the assumption that the signal is present [121].

Consider a test of some parameter θ (for example, proportional to the cross section). To define a test of θ , one identifies the critical region w_θ of the test as $P(x \in w_\theta | \theta) \leq \alpha$. In this manner, the probability to find the data in the critical region under the assumption of that parameter should be less than some α the significance level. Conventionally this is often chosen as 5%.

Confidence intervals for a parameter θ can be found by defining a test of the hypothesized value. A confidence interval is a set of θ values that are not rejected in a test of size α , and the associated confidence level is $CL = 1 - \alpha$. An upper limit of θ is the greatest value for which the hypothesis is not rejected.

The meaning of a confidence interval should be carefully understood, and it is often reported with the parameter itself θ . Consider a confidence interval from $\theta - c$ to $\theta + d$; the result is often reported θ_{-c}^{+d} . The quintessential property of a confidence interval is that it brackets the true value of the parameter with a certain confidence level. So if we consider the probability content of a Gaussian within $\pm 1 \sigma$, we define a confidence level $CL = 1 - \alpha = 68.3\%$. This should not be interpreted to mean that the parameter has a 68.3% chance to lie in this interval, but should be taken instead from a frequentist standpoint, where upon repetition of the measurement, the endpoints of the region fluctuate. The CL_s is the same idea, but instead of having a p -value less than α , it's a particular ratio of p -values. These concepts will be relied upon in the coming analyses.

3.4 Cut-and-count

As an initial approach, we investigate a cut-and-count-based method, a foundational method of physics analysis which applies thresholds to discriminating variables (cuts) for both signal and background, where one hopes to separate the signal from the background. For each variable of interest, a criterion is demanded, and the number of signal s and background b events that pass the selection are counted as in the previous section. Once the optimal cuts have been obtained, chosen to maximise signal kept and background rejected, the significance of the signal over the background can be measured using s and b .

Our objects undergo a preselection, designed to keep only ‘high-quality’ objects while following the expected signature of the signal events. Events are required to feature at least two leptons in the final state and at least two hadronic taus ($N_{\ell\ell} \geq 2$, $N_{\tau\tau} \geq 2$),

with the lepton p_T of at least 10 GeV and the tau p_T of at least 10 GeV. Additionally, a minimum invariant mass is enforced on the lepton pair and the hadronic tau pair, $m_{\ell\ell} > 12$ GeV and $m_{\tau\tau} > 10$ GeV, chosen to avoid low mass hadronic resonances which constitute a background. This selection has a significant impact on the visibility of the lower mass of a . Although it is advantageous to maintain low momentum thresholds for the taus, as we expect the invariant mass spectrum of the tau pair to peak below the ALP mass (as energy is carried away by the neutrinos), we are unable to avoid these stringent lower bounds. Following this minimal preselection, we are left with roughly 50,000 background events, which dwarfs the 10 – 40 events expected for ($10 \text{ GeV} \leq m_a \leq 50 \text{ GeV}$). For $m_a < 10$ GeV and $m_a > 50$ GeV, only a few events are expected, due respectively to preselection and the steeply falling cross section. In order to reject the background events, we investigate the properties of both the lepton and tau pairs, where potentially discriminatory kinematic distributions may be expected. For the following presentation we have chosen to present a selection of five models, $M2$, $M4$, $M7$, $M10$, and $M12$, which are chosen as a representative sample across a variety of group structures. The angular separation between the leptons, $\Delta R(\ell\ell)$, and the invariant mass of the lepton system, $m_{\ell\ell}$, are presented in fig. 3.12, where the five signal hypotheses are presented against the di-boson background. These plots suggest the use of selections

$$\Delta R(\ell\ell) < 3, \quad m_{\ell\ell} < 40 \quad (3.17)$$

as promising in isolating the signal. We see that the variation across models is not significant, with similar behaviour shown across the range of group structures and ALP masses.

The di-tau system also offers potential selection power, as displayed in the corresponding kinematic variables in fig. 3.13. It is notable that the kinematic distributions of the di-tau system show greater variations across masses m_a than was observed for the di-lepton system. As the taus are produced through the decay of the ALP, their kinematics and available phase space are directly correlated to the mass m_a , so this behaviour is expected. We define five regions of interest, each dedicated to an ALP mass hypothesis,

$$m_{\tau\tau} < 10, 20, 30, 40, 50 \text{ GeV}. \quad (3.18)$$

Less helpful in the lighter m_a scenario, this does eliminate some background for the heavier cases. We omit any cut related to the angular separation of the tau leptons

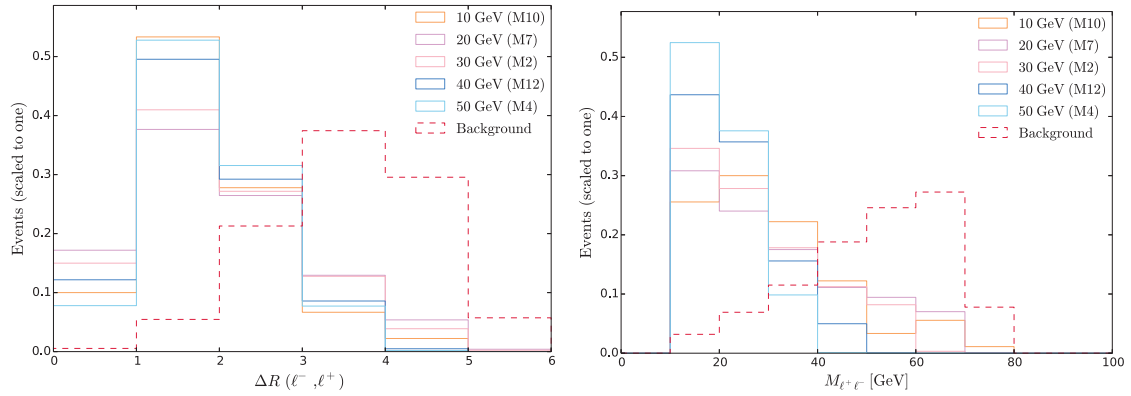


Fig. 3.12 The angular distance in the transverse plane between the two leptons (left), and their invariant-mass spectrum (right) relevant to the di-lepton system. Both signal and background events originating from electron-positron collisions at a centre of mass energy of 91.2 GeV are represented. The background is shown as a red dashed line.

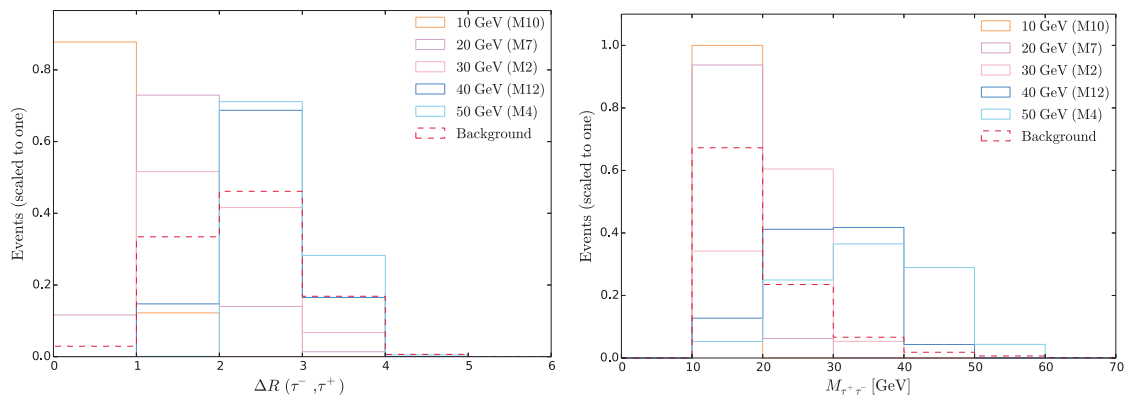


Fig. 3.13 Same as in fig. 3.12 but for the di-tau system.

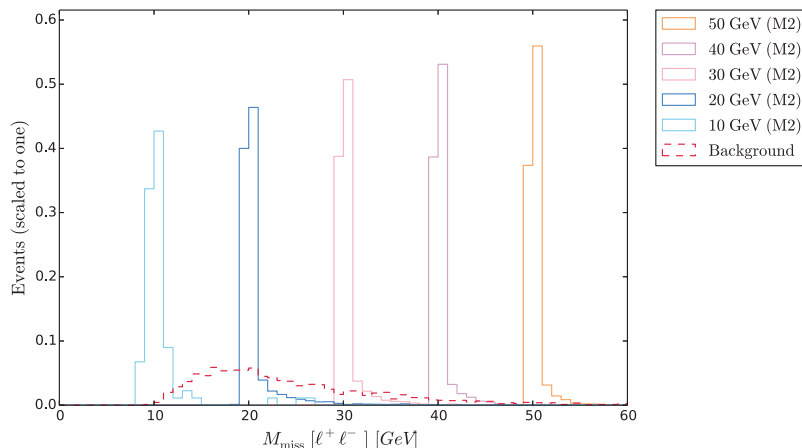


Fig. 3.14 We investigated the use of the missing mass variable to improve the cut-and-count, but the sheer volume of background overwhelms even this variable.

from our analysis, as no clear signal vs background separation is visible from the distribution.

Finally, we investigate the addition of the missing mass variable, $M_{\text{miss}}(\ell\ell)$, which is presented in fig. 3.14. This variable is useful when a part of the final state is observed (here, the leptons), while energy is carried away by invisible components (here, the neutrinos of the hadronic tau decay). The remainder of the final state is computable through the definition

$$M_{\text{miss}} \equiv E_{\text{tot}} - E_{\text{obs}}. \quad (3.19)$$

The initial beam energy \sqrt{s} is the total energy of the system, and E_{obs} is that of the lepton system. In cases where a large amount of energy is carried away in decays $M \rightarrow m_1 m_2$, it is often instructive to utilise the missing mass variable [122]. In the case at hand, the neutrinos are responsible for carrying a large amount of energy away, making this variable instructive. It is expected to be sharply peaked, as is clearly displayed in its distribution. The signal distribution of the missing mass variable is clearly well separated from the background distribution when viewed normalised to one, allowing us to include a selection

$$(m_a - 5) \text{ GeV} < M_{\text{miss}}(\ell^+ \ell^-) < (m_a + 5) \text{ GeV}. \quad (3.20)$$

However, due to the sheer volume of background overwhelming the signal, no significant gain on the significance is made thanks to its inclusion.

Model	10 GeV	20 GeV	30 GeV	40 GeV	50 GeV
M2	0.0015	0.13	0.090	0.049	0.020
M4	0.0013	0.42	0.26	0.12	0.040
M7	0.0024	0.14	0.11	0.061	0.023
M10	0.0042	0.11	0.055	0.023	0.0078
M12	0.00061	0.047	0.035	0.021	0.017

Table 3.4 The significance $s/\sqrt{s+b}$ for the cut-and-count analysis is presented for a representative selection of models, where 150 ab^{-1} of electron-positron collisions at the Z -pole were considered.

In table 3.4, we present the results obtained through the cut-and-count analysis executed with MADANALYSIS5. We again display a representative sample, and indicate the significance $s/\sqrt{s+b}$ obtained. Despite stringent cuts, due to the relative rareness of the signal, we are unable to obtain even a 1σ deviation from the background-only hypothesis. Given this result, we would be unable to confidently observe or rule out the ALP.

3.5 Machine learning

In order to improve our hypothesis test via traditional cut-and-count methods, we may turn to machine learning techniques, which have grown ever more popular in particle physics applications since they were first introduced some 30 years ago [123]. In particular, we will employ the multivariate technique offered by XGBOOST, a decision tree-based algorithm. Boosted decision trees (BDTs) were first shown to be powerful in particle identification applications in recent years [124, 125], and have since been shown to be a viable alternative to traditional methods.

It has previously been shown that BDT methods offer windows to new physics by separating signal from background in a more sophisticated way than standard cut-and-count methods. Indeed, recent analyses in Refs. [121, 126–134] (and others) have shown the possibility of improving the signal significance through the use of decision tree-based tools which provide an alternative to cut-and-count methods, relying on the algorithm to identify the optimal way to analyse the data. One may hope to improve on the shortcomings of a cut-and-count analysis featuring very few signal events, as in this case, as decision trees handle data which fails criteria more sensitively. The advantage of using a machine learning algorithm in place of a

cut-and-count arises through the treatment of events which do not pass a given selection. Rather than a hard rejection of an event which fails a criterion, as is the case in cut-and-count, a decision tree may not reject events when they fail one criterion, but will consider whether other criteria may help classify them better. This may prove invaluable in an analysis such as this one, where the signal events are low in number. Indeed, while the cut-and-count approach may result in very ‘pure’ samples, it may not be realistic to require that events pass every selection. Through noisy data or difficult-to-measure processes, one or more variables in a signal event may not pass a cut which is expected, and many events may not have all the characteristics of signal or background, and so we may not wish to reject every event that just fails one criterion.

Rather than throwing away that entire event, a machine learning algorithm may keep events failing one selection and check whether the other cuts can classify the event, sequentially building trees to classify events which previously failed selections. It is this non-linear cut sequence that makes decision trees more powerful than cut-based algorithms, and may result in improvements in hard-to-reach signal phase space. In the following, outputs of the classification task are restricted to a finite set of values or classes, where the model learns to index the object. The model will be trained on the same simulated events as in the previous cut-and-count section, where true signal events are labelled 0 and true background events are labelled 1.

In the following, we begin by offering a brief theoretical introduction to supervised learning via BDTs, before moving to the application of the model and comparison to cut-and-count methods.

3.5.1 Boosted decision trees

BDTs are a class of supervised learning algorithms, where data fed to the toolkit is labelled with the desired output for training. A supervised learning problem assumes there exists a map f , which may be stochastic or deterministic, relating elements of dataset \mathcal{D} ,

$$y = f(x), \quad \mathcal{D} = \{x_i, y_i\}, \quad (3.21)$$

where x_i are the input data, which have associated to them some features, and y_i the final outcome to be predicted, or the target. The algorithm then determines an approximation to f during training,

$$\hat{f} = \mathcal{A}(\mathcal{D}), \quad (3.22)$$

such that unlabelled data may be suitably classified in a test scenario. Associated to the algorithm is a loss function $\mathcal{L}(y_i, \hat{f}(x_i))$ which should be minimised. The application of the machine learning toolkit takes place over three stages; training, testing, and validation. The division of simulated data into training and testing sets allows for the assessment of the quality of the model, where the *training* set is used to fit and tune the model, and the *testing* set to measure the performance of the model. Finally, a validation subset is typically used in order to measure the accuracy of the model during its tuning.

BDT multivariate techniques are a family of supervised machine learning tools whose robust classification power [124] makes them a popular choice in high energy physics applications. They are built on simple decision tree algorithms, visualised as a set of nodes where a decision must be made to move left or right according to the value of the input data. Simply put, the nodes take an input x and return 0 or 1 if the predicate (for example, $f_1^x < t$, where f_1^x is a feature associated to input x) is respectively true or false in comparison to a threshold t . The splitting at each node should maximise the purity of the split or the separability of signal from background. The last step in each path is a leaf, which determines the classification of the input, and allows the model to make predictions. Decision trees have been in use for many years [135] but are known to be unstable, and so are referred to as weak learners because they do not perform well as standalone classifiers. However, boosting combines numerous weak learners, resulting in a powerful algorithm.

BDTs work from the concept that, while it is hard to make a very good learner, it's easy to make a weak one. BDT algorithms stack these weak learners one on top of the other, fixing any mistakes of the previous learner, which are built successively to improve on the failures of the predecessors. In this manner, a large number of weak learners h_k can be exploited, creating a general meta-algorithm $F(x)$ which can create a strong hypothesis from a weighted sum of weak learners [136]

$$F(x) = \sum_{k=1}^{N_{tree}} \alpha_k h_k(x), \quad (3.23)$$

with $\alpha_k \in \mathbb{R}^T$. A boosting algorithm proceeds by iteratively finding the next learner $h_n(x_i)$ to be added to the ensemble of decision trees for a dataset of size N . This is done through minimisation of the associated loss function $\mathcal{L}(y_i, \hat{f}(x_i))$. The events which are misclassified (signal as background, or *vice versa*), are given a larger weight (not to be confused with the weights present in high energy physics simulations), or *boosted*, and a new tree is built on the new weights. By finding appropriate values for

the weight α_n associated to the new learner $h_n(x_i)$, the loss function is minimised according to

$$\sum_{i=1}^N \mathcal{L}_n(y_i, F_{n-1}(x_i) + \alpha_n h_n(x_i)) \rightarrow \min_{\alpha, h},$$

where $F_{N-1}(x)$ is the function built up to that point. In this way, the boosting algorithm consecutively fits new models to improve the predictive power of the ensemble.

The power of boosting lies not with the strength of the final tree (which would be expected to have very undesirable performance on the full dataset) but rather on the combination of all the weak learners at once. In this work, we will consider binary trees, which output only two possible classes; s or b . The final learner is likely the worst of the lot as measured in performance on the whole data sample, designed to fix some very specific misclassification error. However, when applied as an ensemble, the combination of the weak learners gives a good result. Rather than relying on a single tree, boosting algorithms iteratively construct new base learners (trees) maximally inversely correlated with the gradient of the loss function of the entire ensemble of learners [137], and the discriminating model utilises the weighted average score from many decision trees.

Boosting may be achieved through a number of methods. The XGBOOST toolkit uses gradient descent [138] as a loss function, adding weak learners on each iteration that approximates the gradient of the loss function, a method which is termed *gradient boosting*. In order to utilise gradient descent, the gradient of the loss function is computed with respect to its predictions, using the residuals of the model, $y_i - F(x_i)$, which are the elements of training data where the model had the largest errors. The role of the next learner added is to compensate for the shortcomings of the existing model. In essence, the loss function to be minimised is simply a function of two variables: the true labels and the predicted labels.

3.5.2 Application of XGBOOST

We proceed with the XGBOOST toolkit, beginning with a simple feature selection. While the classifying power of decision trees does not suffer from correlated variables, the features have been reduced to the nine most ‘important’ variables. Reducing the number of features in an analysis minimises the complexity within the model and makes it easier to interpret. An additional advantage is a reduction in CPU time, and the removal of noisy features may assist in reducing overfitting. After removing highly correlated variables to perform an accurate feature importance assessment, the nine

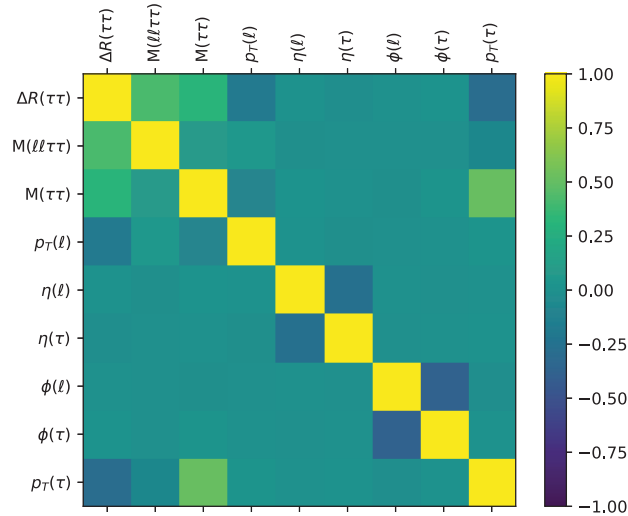


Fig. 3.15 The correlation plot showing the relationship between the nine kinematic variables chosen for our machine learning exercise, where the most ‘important’ variables were chosen. They include angular variables (the separation of the hadronic tau pair $\Delta R(\tau\tau)$), pseudo-rapidities η and azimuthal angle ϕ of the taus and leptons), the invariant mass of the combined lepton-tau system $\ell\ell\tau\tau$ as well as of the di-tau system, and the transverse momenta p_T .

variables selected offer a range of information across both the lepton and tau systems, consisting of both primary and derived variables. The variables are presented in the correlation plot of fig. 3.15, ordered from most important to least from left to right. The objective of XGBOOST was set to logistic regression for binary classification, and a hyperparameter optimisation was performed on the learning rate η , the maximum tree depth, and the minimum child weight, which controls the conditions for node splitting. The training was performed using an 80:20 train:test split, where for each model we tuned the hyperparameters using a k -fold cross validation, using the *auc* metric to assess model performance. Early stopping was employed to avoid overfitting. Each model was trained individually, but the same set of hyperparameters was found to work across the range of models. We thus employed a maximum depth of 3, minimum child weight of 1, and learning rate of 0.3 across all models.

3.5.3 Approximate median discovery significance

Given that the signal and background distributions are simulated using a finite number of events, they have associated to them some statistical uncertainty, where for discoveries only the uncertainty on the background Δb is relevant. The objective

function to be used in the following multivariate analysis is labelled the *approximate mean significance (ams)* [139], and is defined using the profile likelihood ratio test when substituting the Asimov value $n = s + b$. It will be used to estimate the sensitivity of the analysis to our signal, where for known b the median discovery significance is given by [139]

$$ams = \sqrt{2 \left((s + b) \ln \left(1 + \frac{s}{b} \right) - s \right)}, \quad (3.24)$$

where s and b can also be seen as the true and false positives respectively. This formula replaces the simple s/\sqrt{b} significance measure derived from the expected Gaussian behaviour. It is derived from the likelihood ratio statistic for testing $s = 0$, which for b known is

$$q_0 = -2 \ln \frac{L(0)}{L(\hat{s})} = 2 \left(n \ln \frac{n}{b} + b - n \right) \text{ for } n > b, 0 \text{ otherwise.} \quad (3.25)$$

Here $L(x)$ is the likelihood function, and $L(\hat{s})$ is given by the Poisson probability. Assuming sufficiently large $s + b$, we have that the significance $Z = \sqrt{q_0}$. The expected significance is then the expectation value of Z . Finally, we replace n by $s + b$ to create an Asimov data set, where we replace each bin of the histogram with its expected value. For $s \ll b$, this reduces to s/\sqrt{b} . For the background associated to an uncertainty Δb , the Asimov significance is instead defined by

$$ams = \sqrt{2 \left((s + b) \ln \left(\frac{(s + b)(b + \Delta b^2)}{b^2 + (s + b)\Delta b^2} \right) - \frac{b^2}{\Delta b^2} \ln \left(1 + \frac{\Delta b^2 s}{b(b + \Delta b^2)} \right) \right)}. \quad (3.26)$$

In a particle physics context, a significance of 2σ is considered acceptable for exclusion, 3σ for hints of a discovery and 5σ for a full discovery. The *ams* represents the significance, and therefore discovery potential, of a given analysis. It has been argued that the instability of the *ams* make it an unsuitable choice as the optimisation metric for reweighted events during training, although it has been employed as a direct optimization metric with success [121]. As an alternative, a model may be trained using a metric such as *auc*, after which the *ams* on the trained model can be evaluated.

3.5.4 XGBOOST results

In table 3.5, we present the results obtained through this method. Not only do they illustrate an encouraging improvement over the cut-and-count analyses, but also an

	Metric	10 GeV	20 GeV	30 GeV	40 GeV	50 GeV
M2	<i>auc</i>	0.98±0.003	0.87 ± 0.006	0.84 ± 0.0013	0.94 ± 0.0058	0.95 ± 0.0066
	<i>ams</i>	0.22	2.96	2.41	0.29	0.11
M4	<i>auc</i>	0.98±0.0045	0.95±0.0029	0.87±0.020	0.88±0.042	0.89±0.061
	<i>ams</i>	1.16	2.83	1.69	0.54	0.15
M7	<i>auc</i>	0.98±0.0018	0.86±0.0082	0.88±0.0011	0.90±0.0012	0.94± 0.019
	<i>ams</i>	0.22	3.20	2.58	0.27	0.14
M10	<i>auc</i>	0.98±0.003	0.92± 0.0057	0.90±0.019	0.96±0.0078	0.96±0.0050
	<i>ams</i>	0.37	4.08	2.35	0.14	0.042
M12	<i>auc</i>	0.98±0.0075	0.92±0.003	0.92± 0.013	0.95±0.0044	0.96 ± 0.0082
	<i>ams</i>	0.066	1.26	0.98	0.11	0.046

Table 3.5 The outcomes of the XGBOOST evaluation metric and significances obtained for the same representative set of models and ALP masses, using 150 ab^{-1} of electron-positron collisions at the Z -pole.

interesting variation across models and masses. As expected from the shape of the cross section, the significance peaks at $m_a = 20 \text{ GeV}$. This is due to the number of events in this signal hypothesis, but also perhaps due to the fact that the hyperparameter training was done on this mass choice for each model. The poor results for $m_a = 10 \text{ GeV}$ are due to the preselection cuts rejecting a large portion of the signal. The low significances obtained for the larger masses is largely due to the drop off of the cross section. In addition, larger m_a leads to variations in the kinematics; in particular, one's attention is drawn to the $\Delta R(\tau\tau)$ variable of fig. 3.13, where for larger ALP masses the signal and background distributions behave similarly, leading to more difficult discrimination. The difference in trends across models should also be noted, which result from differing Lagrangian parameters fixed by the underlying fermion dynamics of the models.

In comparing the significance trends across the cut-and-count and machine learning methods, we observe similar performance rankings across models, with the exception of M4. With the highest cross section, one could have expected better results in the BDT training. However, we encountered some overtraining in our model and had to employ early stopping to control it, resulting in a lower significance.

Finally, in table 3.6, we translate our results into the required luminosities needed to achieve significances of 2σ or 3σ , where the first is regarded as sufficient to exclude regions of phase space, and the latter is the minimum requirement to claim evidence

for new phenomena. These luminosities are quoted for a circular lepton collider operating at the Z pole, and display the gain in sensitivity made through the employment of the multivariate techniques. Crucially, our results show that, for the $m_a \in [20, 30]$ GeV mass range, an achievable luminosity would yield promising significances. The largest and smallest masses remain largely out of reach.

3.6 Conclusion

The work in this chapter has focused on the four-lepton final state as a lesser-studied signature, where similar studies [140] have shown the $e^+e^- \rightarrow a\gamma(a \rightarrow \ell\ell)$ channel to be more constraining for axion-like particles. In focusing on the weaker channel, we demonstrate the power of machine learning tools. Broad reviews have been done [140, 141] on the existing bounds of axion-like particles such as this one, including future collider prospects. Our search falls into the unconstrained parameter space in those studies, and is complementary to the channels there investigated. The analysis will also complement proposed studies at the LHC in Ref. [99], and is additionally complementary to existing di-photon searches [104]. Further, it could extend the current 90 GeV lower bound [142] observed for di-tau searches. In the case of the di-photon searches, it was also shown [99] that the di-photon and di-tau searches feature inverse sensitivity behaviours for the models and the mass range considered here. A recent summary of the bounds on ALPs for photon final states [143] collates the exclusions on axion-like particles, characterised by the coupling to photons there defined as $g_{a\gamma}$. We find that, in our case, our parameter space lies below the space constrained by LHC searches. We find, in summary, that the resonance evades all existing bounds, and could be accessed through channels harnessing machine learning capabilities. Complementary works have recently been proposed exploring the light a through Z -portal channels [144], where production in association with a photon is examined at both the FCC-ee and CEPC, and the precision with which future lepton colliders can examine composite Higgs scenarios is discussed.

The introduction to this chapter outlined the myriad of ways such an ALP may occur in nature. If such a particle is identified at colliders, how could it be pinned down to a composite (or indeed, any other) theory? The answer to this may not exist yet, as the compositeness of such a state could not be ascertained through coupling measurements. In general, we could expect multi-particle vertices to arise within a generic composite model at the effective level, as occurs with pions, which could offer clues.

Model	m_a [GeV]	Cut-and-count		Machine Learning	
		2σ	3σ	2σ	3σ
M2	10	2.67×10^8	6.00×10^8	1.24×10^4	2.79×10^4
	20	3.55×10^4	7.99×10^4	68.5	154
	30	7.41×10^4	1.67×10^5	103	232
	40	2.50×10^5	5.62×10^5	7.13×10^3	1.61×10^4
	50	1.50×10^6	3.38×10^6	4.96×10^4	1.12×10^5
M4	10	3.55×10^8	7.99×10^8	446	1.00×10^3
	20	3.40×10^3	7.65×10^3	74.9	169
	30	8.88×10^3	2.00×10^4	210	473
	40	4.17×10^4	9.38×10^4	2.06×10^3	4.63×10^3
	50	3.75×10^5	8.44×10^5	2.67×10^4	6.00×10^4
M7	10	1.04×10^8	2.34×10^8	1.24×10^4	2.79×10^4
	20	3.06×10^4	6.89×10^4	58.5	132
	30	4.96×10^4	1.12×10^5	90.1	203
	40	1.61×10^5	3.63×10^5	8.23×10^3	1.85×10^4
	50	1.13×10^6	2.55×10^6	3.06×10^4	6.89×10^4
M10	10	3.40×10^7	7.65×10^7	4.38×10^3	9.86×10^3
	20	4.96×10^4	1.12×10^5	36.0	81.1
	30	1.98×10^5	4.46×10^5	109	244
	40	1.13×10^6	2.55×10^6	3.06×10^4	6.89×10^4
	50	9.86×10^6	2.22×10^7	3.40×10^5	7.65×10^5
M12	10	1.61×10^9	3.63×10^9	1.38×10^5	3.10×10^5
	20	2.72×10^5	6.11×10^5	378	850
	30	4.90×10^5	1.10×10^6	624	1.41×10^3
	40	1.36×10^6	3.06×10^6	4.96×10^4	1.12×10^5
	50	2.08×10^6	4.67×10^6	2.84×10^5	6.38×10^5

Table 3.6 Respective integrated luminosities in ab^{-1} which would be required to obtain a 2σ and 3σ significance for the ALP signal over the backgrounds considered at a future electron-positron collider operating at the Z -pole. We compare results for our cut-and-count (third and fourth columns) and machine learning (fifth and sixth columns) methods, for an illustrative selection of models, where the latter displays superior performance.

Having outlined a potential search channel for the ubiquitous ALP over twelve models, we now move to an examination of the most minimal of those models, and examine possible phenomenology at colliders.

Chapter 4

An $SU(4)/Sp(4)$ case study

As we have outlined in the previous sections, composite Higgs models may take many forms, where a number of models allow for the EW symmetry to be dynamically broken. In the following, we will more closely examine a minimal composite Higgs model, $SU(4)/Sp(4)$, recognised as the most fundamental model achievable with an underlying fermion structure. The EFT description of the model will contain the light pNGBs, including the Higgs, where the heavier states are integrated out. We will use this opportunity not only to examine some related phenomenology, but also to present a more thorough explanation of the workings of a generic composite Higgs model, including the spontaneous and explicit symmetry breaking and their physical consequences.

The model at hand features the EW coset $SU(4)/Sp(4)$ and the coloured coset $SU(6)/SO(6)$, with an $SU(4)$ hypercolour gauge group. Emerging from the chiral theory are two pNGBs, both bound states of ψ hyperfermions, and which are identified as the Higgs h and an additional light singlet η . Additionally, and to build upon previous studies, we will include the light pseudo-scalar a of the previous section, always present in these models. It is notable that lattice studies [66, 67, 145] have shown that the breaking of $SU(4)$ to $Sp(4)$ occurs dynamically. We will base our model on the smallest asymptotically free gauge group featuring the minimal number of fermions needed for model building.

We will follow an effective Lagrangian approach, and investigate the status of the theory at current and future colliders. In particular, we would like to assess how realistic an analysis searching for the η resonance may be, particularly in the context of future colliders. The coupling of η to SM fermions is controlled by a free parameter in the theory, and in certain scenarios may be switched off. Consequently we consider both fermiophobic and fermiophilic states for the η . In the following, we first outline

the fundamental Lagrangian pertaining to the underlying fermions in section 4.1, and follow it with a description of the effective theory in section 4.2. We then outline the prospects for phenomenology at future lepton colliders, focusing on the scenario where η is heavy.

4.1 The underlying model

We begin by describing the dynamics of the fundamental fermions of the theory. The model closely follows the structure presented in Ref. [47], and features an $SU(2)$ strongly coupled gauge group which is generalised to $Sp(2N)$, with $N = 2$ [47]. The fundamental fermions lie in a pseudo-real representation of the hypercolour group, and are described as four Weyl fermions Q^i , with a global $SU(4)$ flavour symmetry. The Lagrangian related to the underlying fermions is written as [47]

$$\mathcal{L} = -\frac{1}{4}F_{\mu\nu}^a F^{a\mu\nu} + Q_j (i\sigma^\mu D_\mu) \bar{Q}_j - M_Q^{ij} Q_i Q_j + h.c. \quad (4.1)$$

with $F_{\mu\nu}^a$ the field strength of the gauge group, and M_Q is a mass matrix for the quarks which will feature in the explicit symmetry breaking terms. Recall that the condensate, which breaks the global symmetry, can be decomposed as $\langle Q^i Q^j \rangle = \mathfrak{6}_{SU(4)} \rightarrow \mathfrak{5}_{Sp(4)} \oplus \mathfrak{1}_{Sp(4)}$. This shows that we may expect the coset space to be parametrised by five Goldstone bosons, with an additional singlet. The mass matrix can be written as

$$M_Q = \begin{pmatrix} \mu_L i\sigma_2 & 0 \\ 0 & \mu_R i\sigma_2 \end{pmatrix}, \quad (4.2)$$

where for $|\mu_L| = |\mu_R|$ the global group is explicitly broken to $Sp(4)$. The most general vacuum depends on the broken generators X^j , of which there are 5, and may be written as

$$\Sigma_0 = e^{i\theta X^4} \cdot \Sigma_B, \quad (4.3)$$

where Σ_B is the EW preserving vacuum aligned with the mass matrix,

$$\Sigma_B = \begin{pmatrix} i\sigma_2 & 0 \\ 0 & -i\sigma_2 \end{pmatrix}. \quad (4.4)$$

While this theory dictates the behaviour of the fundamental fermions, the observables at colliders are governed by the low energy theory. In the following, we outline the framework responsible for the phenomenology.

4.2 The Effective Field Theory framework

Generically, the Lagrangian resulting from such an EFT, to be added to the generic SM Lagrangian, will take the form

$$\mathcal{L} = \mathcal{L}_\pi + \mathcal{L}_M + \mathcal{L}_Y - V_t, \quad (4.5)$$

where \mathcal{L}_π encodes the kinetic terms for the pNGBs, and where additional kinetic terms should be included for scalar resonances which are not pNGBs but which are light enough to be considered. The mass terms of \mathcal{L}_M are a source of explicit symmetry breaking and are proportional to $f^2 M^2 \text{Tr} [\Sigma + \Sigma^\dagger]$, arising due to the Dirac mass given to the underlying fermions. The kinetic term for the pions is proportional to the scale of spontaneous flavour symmetry breaking f , and is of the form $\text{Tr} [D_\mu \Sigma (D^\mu \Sigma)^\dagger]$. It is through this term that the couplings of the pNGBs to gauge bosons arise via the covariant derivative. It is common practice to consider only the SM top quark as being included in the EFT formalism, encoded through \mathcal{L}_Y possibly through top partial compositeness. This term can be written as

$$\mathcal{L}_Y \sim f (\bar{Q}_L^\alpha t_R) \text{Tr} [P_\alpha \Sigma] + \text{h.c.}, \quad (4.6)$$

where $H_\alpha = \text{Tr} [P_\alpha \Sigma]$ transforms as the SM Higgs doublet, and where P_α is the projection operator. This interaction also generates a potential

$$V_t \sim C_t \sum_{\alpha=1}^2 |\text{Tr} [P_\alpha \Sigma]|^2. \quad (4.7)$$

As discussed in section 2.2.2, the pNGB component of the Higgs boson has a degree of freedom θ , the vacuum misalignment angle, which relates the EW symmetry breaking scale v to the scale of global flavour breaking f . In order to obtain the large separation between v and f , which is enforced by compositeness not yet appearing at colliders, a very small misalignment angle is needed. In fact, while the Higgs couplings enforce an upper bound of 0.71 (CMS) and 0.61 (ATLAS), EWPTs related to LHC Run 1 results require $\theta < 0.239$ radians for an $SU(2)$ underlying gauge group [47] in the decoupling limit.

We will now expand the Lagrangian of eq. (4.5), beginning with the kinetic and Yukawa-type terms which emerge from a chiral Lagrangian governed by the CCWZ [33, 34] formalism, and then discussing the emergence of the potential for the pNGBs. The explicit breaking via the mass term is outlined in section 4.2.3, and

	g_{hXX}	g_{hhXX}	$g_{\eta XX}$	$g_{\eta\eta XX}$
WW	$\sqrt{2}g^2 f s_\theta c_\theta$	$\frac{g^2 c_{2\theta}}{4}$	—	$-s_\theta^2$
ZZ	$\sqrt{2}(g^2 + g'^2) f s_\theta c_\theta$	$\frac{g^2 c_{2\theta}}{c_W^2 4}$	—	$-s_\theta^2$
$f\bar{f}$	$\frac{m_f}{v} c_\theta$	$\frac{s_\theta m_f 2\sqrt{2}}{16fv}$	—	$\frac{s_\theta m_f 2\sqrt{2}}{16fv}$

Table 4.1 Couplings emerging from the chiral Lagrangian. Notably, linear couplings of the η state are absent.

finally non-standard couplings via WZW and triangle couplings are discussed in section 4.2.4.

4.2.1 The chiral effective model

In the following, a chiral Lagrangian formalism will be employed to describe the phenomenology and kinematics of the resonances emerging due to the symmetry breaking, where the physics of the five Goldstone bosons emerging from the theory can be described by the CCWZ formalism. In this set-up, the pNGBs are governed by the linearly transforming matrix

$$\Sigma = e^{i \sum_{j=1}^5 Y^j \chi_j / f} \cdot \Sigma_0, \quad (4.8)$$

where χ_j are the pNGB fields and $Y^j = e^{i\theta/2X^4} \cdot X^j \cdot e^{-i\theta/2X^4}$ are the broken generators in the Σ_0 vacuum. The chiral Lagrangian, encoding the kinematics and Yukawa-type Lagrangian, is then given by

$$\begin{aligned} \mathcal{L}_{CCWZ} = & f^2 \text{Tr} \left[(D_\mu \Sigma)^\dagger D^\mu \Sigma \right] + \\ & f \left(y_u^{ij} (Q_{L,i} u_{R,j}^c)^\dagger_\alpha + y_d^{ij} (Q_{L,i} d_{R,j}^c)_\alpha + y_l^{ij} (L_i l_j^c)^\dagger_\alpha \right) \text{Tr} [P^\alpha \Sigma] + h.c. \end{aligned} \quad (4.9)$$

Here, the first term is purely kinematic. The second term describes the effective couplings of the condensate to SM fermions, taking the place of the Yukawa terms in the SM Lagrangian. It is notable that the chiral Lagrangian results in linear couplings only for the Higgs-like state h to SM fermions, while the other light pNGB, η features quadratic couplings to the SM fermions. For this reason, linear couplings of the η state to SM fermions will be handled separately in section 4.2.3 below. The terms emerging from this Lagrangian will feature interactions between the two states, η and

h . The expansion of the chiral structure also yields kinematics and masses for the EW gauge bosons W and Z , and is expanded (to $\mathcal{O}(f^2)$) as [52]

$$\begin{aligned}
f^2 \text{Tr} \left[(D_\mu \Sigma)^\dagger D^\mu \Sigma \right] &= \frac{1}{2} (\partial_\mu h)^2 + \frac{1}{2} (\partial_\mu \eta)^2 \\
&+ \frac{1}{48 f^2} \left[-(h \partial_\mu \eta - \eta \partial_\mu h)^2 \right] + \mathcal{O}(f^{-3}) \\
&+ \left(2g^2 W_\mu^+ W^{-\mu} + (g^2 + g'^2) Z_\mu Z^\mu \right) \left[f^2 s_\theta^2 + \frac{s_{2\theta} f}{2\sqrt{2}} h \left(1 - \frac{1}{12 f^2} (h^2 + \eta^2) \right) \right] \\
&+ \frac{1}{8} (c_{2\theta} h^2 - s_\theta^2 \eta^2) \left(1 - \frac{1}{24 f^2} (h^2 + \eta^2) \right) + \mathcal{O}(f^{-3}).
\end{aligned} \tag{4.10}$$

The couplings produced from the expansion are recorded in table 4.1, and the masses of the gauge bosons are revealed to be

$$m_W^2 = 2g^2 f^2 s_\theta^2, \quad m_Z^2 = 2(g^2 + g'^2) f^2 s_\theta^2 = m_W^2 / c_W^2, \tag{4.11}$$

leading to the vacuum expectation value $v = 2\sqrt{2} f s_\theta$. Additionally, the condensation of the fundamental fermions generates the second term in eq. (4.9), which can be expanded as

$$f \left(y_u^{ij} (Q_{L,i} u_{R,j}^c)^\dagger \right) \text{Tr} [P^\alpha \Sigma] \sim y_u^{ij} \left(f s_\theta + \frac{1}{2\sqrt{2}} c_\theta h - \frac{1}{16 f} s_\theta (h^2 + \eta^2) + \dots \right) u_{R,i} u_{L,j}^c \tag{4.12}$$

for up-type quarks, and similarly for the down-type quarks and leptons.

4.2.2 Scalar potential

In addition to kinetic terms, the scalar potential in a composite Higgs model is a crucial component of the theory. Recall that, unlike in technicolour models, the subgroup H featuring in composite Higgs models can accommodate the EW group. However, H can be misaligned within G such that only the $U(1)$ symmetry lies in H ; that is, H and the EW symmetry group are misaligned. This misalignment is generated through the effective scalar potentials which arise for the pNGBs, where minimising the potential then yields the misalignment of H with the EW group. In this section we will identify the form of a generic scalar potential.

The masses of the physical states whose physics is governed by the chiral Lagrangian, h and η , emerge from a potential which explicitly breaks the global symmetry at tree

and loop levels,

$$V_{scalars} = V_{top} + V_m. \quad (4.13)$$

The first term is generated by top loops, and the second by the masses of the techniquarks, directly breaking the global flavour symmetry. As in Ref. [47] we neglect the term originating from loops of EW gauge bosons, as it is smaller than the contribution from the top. The contributions are described in detail in Refs. [47, 52], such that here we just quote the result employed in the model. The contribution to the potential resulting from the explicit breaking of $SU(4)$ by the mass matrix is expanded as

$$V_m \sim C_m \left(-4f^4 c_\theta + \sqrt{2}f^3 s_\theta h + \frac{1}{4}f^2 c_\theta (h^2 + \eta^2) + \dots \right), \quad (4.14)$$

and the contribution from the loops of tops is given as

$$V_{top} \sim C_t y_t'^2 \left[f^4 s_\theta^2 + \frac{1}{\sqrt{2}}f^3 c_\theta s_\theta h + \frac{1}{8}f^2 (c_{2\theta} h^2 - s_\theta^2 \eta^2) + \dots \right]. \quad (4.15)$$

In each case the coefficients C_t and C_m are of $\mathcal{O}(1)$ and are determined by the underlying dynamics, and $y_t'/2\sqrt{2} = m_f/v$ [52]. The potential is minimised for

$$C_m = \left(\frac{y_t}{v} \right)^2 \frac{C_t c_\theta}{2}, \quad (4.16)$$

which corresponds to EWSB, and the masses of the (massive) pNGBs are found to be

$$\begin{aligned} m_h^2 &= \frac{y_t'^2 C_t f^2}{4} s_\theta^2, \\ m_\eta^2 &= \frac{y_t'^2 C_t f^2}{4}. \end{aligned} \quad (4.17)$$

In this manner, clear differences with the SM are demonstrated as had been described in previous sections; here, the Higgs boson acquires a mass as a consequence of this scalar potential, which itself arises due to the explicit breaking of symmetries in the theory.

4.2.3 Explicit symmetry breaking: fermion couplings

As we have demonstrated in the previous section, explicit symmetry breaking terms in a composite Higgs model are crucial to the functioning of the theory, as they lead to physical consequences that are required in any given model. The linear coupling of η

to fermions is another feature which arises from an explicit breaking term, as it does not naturally emerge from the chiral structure. As with the potential V_m above, the explicit breaking emerges due to the masses of the fundamental fermions and the top Yukawa coupling. At leading order, an operator which gives rise to a linear coupling of η with fermions appears as

$$\mathcal{O}_1 = (Qt^c)_\alpha^\dagger \text{Tr} [M_Q \Sigma P^\alpha \Sigma], \quad (4.18)$$

and is expanded as

$$\mathcal{O}_1 = (\mu_L - \mu_R) c_\theta s_\theta t_L^c t_R^c + \frac{1}{2\sqrt{2}f} [h(\mu_L - \mu_R) c_{2\theta} + i\eta(\mu_L + \mu_R) s_\theta] t_L^c t_R^c + \dots, \quad (4.19)$$

including a correction to the top mass and the coupling of the Higgs to the top. For $\mu_L = -\mu_R$, the coupling to η vanishes. A similar operator can be written for all fermions, leading to a modification of the fermion masses of at most

$$\delta m_f = (\mu_L - \mu_R) \cos \theta \sin \theta. \quad (4.20)$$

In the following, we fix the modification to the fermion masses to be at most 10% of the fermion mass. In particular, a change of more than 10% to the top mass would lead to modifications of the scalar potential in the previous section, warranting a reconfiguration of the structure of the model. We can use this to set the value of μ_L , where

$$0.1 m_t = 1.82 \mu_L \cos \theta \sin \theta \implies \mu_L = \frac{0.1 m_t}{1.82 \cos \theta \sin \theta}. \quad (4.21)$$

We identify two independent cases; that the η state is fermiophobic, where $\mu_L = -\mu_R$, and the case where the coupling of η to fermions is non-zero. For the latter case, we will need to make a choice about the magnitude of μ_L , and we will consider the explicit breaking of $SU(4)$ to be maximal, such that

$$\tau = \frac{\mu_L - \mu_+}{\mu_L - \mu_R} = 0.1. \quad (4.22)$$

Thus far we have demonstrated the need to combine the terms emerging from the effective Lagrangian with those introduced through explicit symmetry breaking. Before moving to a study of the phenomenology for fermiophobic and fermiophilic η , we complete the linear couplings for the η by investigating the effective terms which facilitate its coupling to the gauge bosons.

4.2.4 WZW and triangle boson couplings to η

The couplings of the η to the gauge bosons is accounted for in an anomalous WZW form which also does not emerge from the chiral structure. In particular, couplings to the EW gauge bosons arise as

$$g_{\eta WW} = \frac{g^2 s_\theta c_\theta}{16\sqrt{2}\pi^2 v}, \quad g_{\eta ZZ} = \frac{(g^2 - g'^2) s_\theta c_\theta}{16\sqrt{2}\pi^2 v}, \quad g_{\eta Z\gamma} = \frac{gg' s_\theta c_\theta}{16\sqrt{2}\pi^2 v}, \quad (4.23)$$

and are included as effective couplings in the Lagrangian. Direct couplings to gluons vanish as the fundamental fermions ψ are colourless, and any coupling to photons vanishes as $U(1)_{em}$ is fully embedded in $SU(4)$. However, both couplings are generated by a top quark loop in a triangle diagram, in a similar fashion to the pseudo-scalar gauge boson couplings of the previous chapter. The bottom quark loop contribution to the triangle couplings has been included in the model as well. The couplings proceeding through a triangle diagram can be included in an effective fashion, where in particular the $\eta - gg$ coupling is of the form

$$\begin{aligned} F &= -i^3 (-ig_s)^2 \left(0.01 \frac{m_f}{v} \tan \theta\right) \text{Tr} \left(T^a T^b\right) \frac{i\pi^2}{16\pi^4} \frac{8m_f}{\sqrt{2}} (1 + (1 - \tau)A(\tau)) \\ &= i\alpha_s \delta^{ab} \frac{1}{4\sqrt{2}\pi} 0.01 \tan \theta \frac{m_\eta^2}{v} \tau (1 + (1 - \tau)A(\tau)), \end{aligned} \quad (4.24)$$

where m_f is the mass of the fermion in the triangle loop. The relation of the operators in position and momentum space $F P_T^{\mu\nu} A_{1\mu} A_{2\nu} = F (-G^{\mu\nu} G_{\mu\nu}) / (\sqrt{2}m_\eta^2)$ [146], with $P_T^{\mu\nu}$ the transverse tensor, yields the relevant coupling for η as

$$\mathcal{L}_{\eta gg} = \frac{\alpha_s}{8\pi} \frac{0.01 \tan \theta}{v} \tau (1 + (1 - \tau)A(\tau)) \eta G^{\mu\nu} G_{\mu\nu}, \quad (4.25)$$

with τ_f and $A(\tau)$ as featured in eqs. (3.10) and (3.11). Like the hgg coupling, the factor in front of the dimension-five operator is $1/v$, such that this term does not decouple for heavy quarks. Similarly, the effective $\eta\gamma\gamma$ coupling is

$$\mathcal{L}_{\eta\gamma\gamma} = \frac{\alpha}{4\pi} N_c Q_f^2 \frac{0.01 \tan \theta}{v} \tau (1 + (1 - \tau)A(\tau)) \eta F^{\mu\nu} F_{\mu\nu}, \quad (4.26)$$

with $N_c = 3$ the number of QCD colours in the theory, and Q_f the electric charge of the fermion in the loop. As discussed in the previous chapter, the $U(1)$ pseudo-scalar a is a ubiquitous presence in models of this nature. As such, its inclusion in the model

warrants an additional coupling ηaa of the form

$$\mathcal{L}_{\eta aa} = \frac{3C_t^2 m_t^2 (0.01 \tan \theta)}{8\pi^2 f^2 v} \log \frac{\Lambda^2}{m_t^2} \eta (\partial_\mu u a) (\partial^\mu a) \quad (4.27)$$

facilitating an additional decay channel for the η .

4.3 Phenomenology at colliders

With all terms accounted for, with the notable inclusion of linear couplings for the η , we now proceed to investigate the phenomenology of the η state at colliders. We will make a distinction between fermiophobic and fermiophilic η models as outlined above, and also initially consider possible studies for both heavy and light η . In the following we begin with a naive investigation of the production at the FCC-ee circular collider for lighter η , and production at CLIC, including higher collision energies and polarised beams, for all masses of η , which may be produced in association with a photon or with a Z -boson. As in the previous chapter, we employ the FEYNRULES [111] package for model-building and for the generation of UFO model files [114] as inputs into the MG5_AMC Monte Carlo generator framework [113]. We simulate collisions at colliders for both signal and background processes using PYTHIA 8 [118] to describe parton showering and hadronisation and the DELPHES 3 [115] software package with the anti- k_T algorithm [116] as implemented in FASTJET 3 [117] for event reconstruction. We employ the MADANALYSIS 5 platform [119, 120] for analysis and cut and count selections. As previously, we apply detector-level pre-selections to the objects to ensure that they are of good quality. We require

$$p_T(\ell) > 10 \text{ GeV}, \quad |\eta(\ell, j)| < 2.5, \quad p_T(j) > 20 \text{ GeV}. \quad (4.28)$$

We also reject leptons where $\Delta R(j, \ell) < 0.4$ (that is, where leptons and jets are not well-separated). These selections ensure that the simulated objects would be accounted for in a real-life detector setting, and that their properties are able to be correctly measured.

A study of the case where all couplings are included (referred to here as fermiophilic) has been conducted in Ref. [47], where it is shown that the η is produced more copiously at hadron colliders, with pair production being the dominant mechanism. In the following, we will consider future lepton colliders as an alternative to production via proton collision. As a naive initial investigation we examine production cross

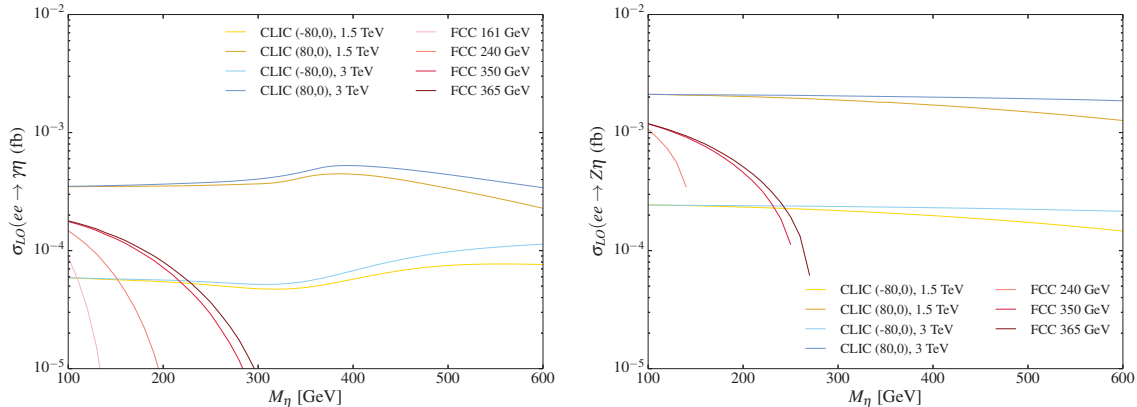


Fig. 4.1 Production in association with a photon (left) and Z boson (right) at CLIC and FCC-ee. In these plots the decay constant f was set to 1 TeV, and the angle θ chosen to reproduce SM masses ($\theta = 0.09$).

sections of η in association with neutral gauge bosons at CLIC and the FCC-ee in fig. 4.1, where the cross section for production in association with a Z is larger but will be subject to a reduction due to the Z decay which is not included here. The scenario depicted here encompasses all possible couplings, where a representative value of θ is chosen. Given that the $\eta\gamma\gamma$ vertex appears through a triangle diagram of quarks as in eq. (4.26), while the $\eta Z\gamma$ and ηZZ vertices appear as an effective interaction, the shapes of the diagrams are significantly different, with some undulation visible in the $\eta\gamma$ final state which is reminiscent of those in chapter 3. We refer to those results regarding the top and bottom quark contributions to the fermion triangle contributions. The different polarisations of CLIC also make a significant impact, although unfortunately the positive polarisation is expected to have a lower integrated luminosity, which will counteract the larger cross section illustrated in the figure. We note also that the cross sections for the lower centre of mass energy colliders at the FCC-ee fall off quickly as the phase space diminishes, as expected. While initially we placed no restrictions on the mass m_η , in the minimal case the free parameters m_η and θ are related by the equation

$$m_\eta \approx m_h / \sin \theta. \quad (4.29)$$

This relation will be considered going forwards. Given that EWPTs enforce a strict upper bound on θ with $\theta \leq 0.24$ degrees, the mass of η is enforced to lie above roughly 500 GeV. As a result, production at the FCC-ee is ruled out and production at CLIC, as a higher centre-of-mass alternative, will be studied. Given previous studies

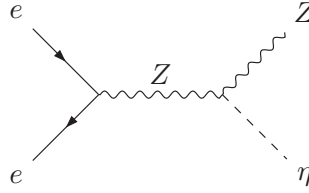


Fig. 4.2 Feynman diagram illustrating the production of fermiophobic η with a Z boson.

considering the fermiophilic case [47], we will focus on the fermiophobic case, where $\mu_L = -\mu_R$ such that the coupling to tops (and fermions) of the form $\eta f f$ vanishes.

4.3.1 Fermiophobic phenomenology

In the fermiophobic scenario, where η does not couple to SM quarks, the disappearance of fermion couplings implies that the $\eta g g$ and $\eta \gamma \gamma$ couplings vanish as they rely on couplings to fermions for the quark loop. In this limit, the dominant decays of η will then be to heavy gauge bosons which proceed through the Wess-Zumino-Witten anomaly. As a start, we check the production of η with a Z -boson at CLIC, as illustrated in fig. 4.2, where further decays are not illustrated. Both $e^+e^- \rightarrow \eta Z$ and $e^+e^- \rightarrow \eta\eta$ signatures are possible under the $\mu_L = -\mu_R$ constraint, but production in association with a Z boson is found to be dominant. In the heavy η mass range, we find that the dominant decay modes are those into Z and W bosons (whereas dominant decay mode in the all-couplings scenario was to a pair of top quarks).

Considering the scenario where a heavy η is produced in association with a Z boson, we envisage a scenario where η then decays to two Z bosons, which is the channel with the largest cross section. This would result in a ZZZ final state which is expected to have a minimal SM background: a naive estimate of the relevant background reveals that the process, $e^+e^- \rightarrow ZZZ$ is produced with cross section of 0.0003 pb (excluding the Z decays). Full studies of this nature should carefully treat photon misidentification rates, as discussed in detail in Ref. [144], which may constitute a dominant background here. We will consider the scenario where two Z bosons decay to leptons, and the third decays to jets. The signal process

$$e^+e^- \rightarrow Z\eta, (Z \rightarrow jj), (\eta \rightarrow ZZ, Z \rightarrow \ell^+\ell^-, Z \rightarrow \ell^+\ell^-) \quad (4.30)$$

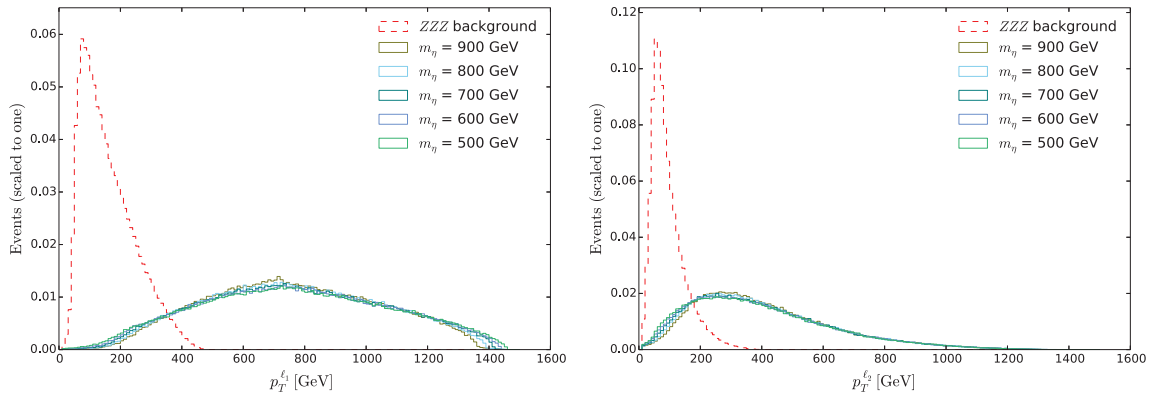


Fig. 4.3 Transverse momenta p_T of the first (left) and second (right) lepton in the system. The background (red dashed line) is clearly peaked at low energies, while the signal appears spread out towards higher energies.

is chosen in hopes of isolating $M(4\ell) \approx m_\eta$, but will experience interference with the process

$$e^+e^- \rightarrow Z\eta, (Z \rightarrow \ell^+\ell^-), (\eta \rightarrow ZZ, Z \rightarrow jj, Z \rightarrow \ell^+\ell^-), \quad (4.31)$$

and will be subject to triple- Z production in the SM as a background process, where two Z s decay to leptons and one to jets. This is a relatively rare SM process.

As such, we shall consider a mass scan for η in the range $m_\eta \in [500, 900]$ GeV, with θ calculated accordingly. We find that the background cross section is of the order of 5×10^{-6} pb, and the signal varies between 3×10^{-8} pb for the lightest m_η to 1×10^{-8} pb for the heaviest. The most clear discrimination between signal and background arises in the invariant mass of the four lepton system and the transverse momenta of the first and second leptons. The latter are visible in fig. 4.3, indicating a selection to be introduced for

$$p_T^{\ell_1} > 400 \text{ GeV}, \quad p_T^{\ell_2} > 200 \text{ GeV}.$$

Further distinctions are visible through the invariant mass plot $M(\ell_1^+\ell_1^-\ell_2^+\ell_2^-)$, shown in fig. 4.4, motivating a selection

$$m_\eta - 100 \text{ GeV} < M(\ell_1^+\ell_1^-\ell_2^+\ell_2^-) < m_\eta + 10 \text{ GeV}.$$

Fig. 4.4 illustrates that, for lighter η , the background may be almost entirely removed. However, the rarity of the signal results in at most 0.032 signal events for 4.63 background events at CLIC with a collision energy of 3 TeV and a polarisation of (80,0), which is associated to a total integrated luminosity of 1 ab^{-1} . The paucity of events at the collider will result in this channel being difficult to pursue unless a much

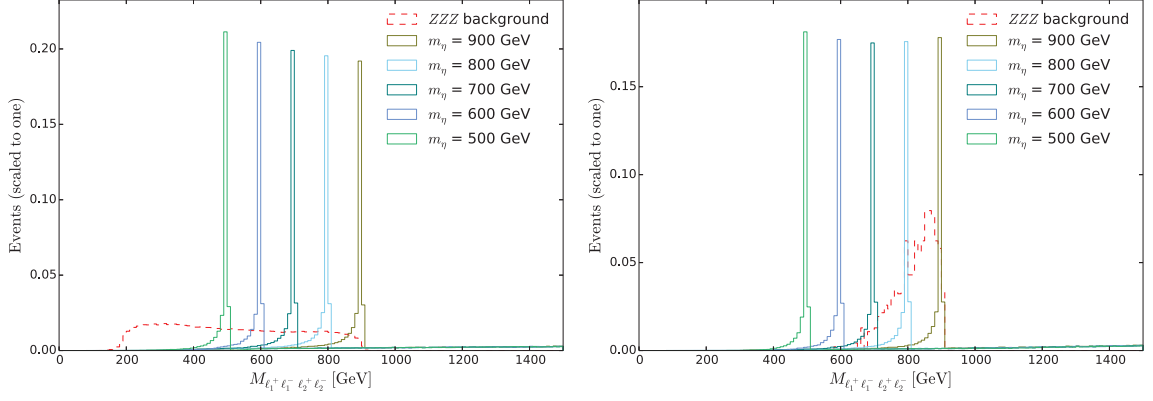


Fig. 4.4 Invariant mass plot for the fermiophobic search case before and after the lepton p_T cuts, where sharp peaks are visible at the mass of η in each case. A flat tail extends to 3 TeV.

m_η	n		Cut 1		Cut 2		Cut 3		Z
	s	b	s	b	s	b	s	b	
500	0.032	4.63	0.028	0.040	0.023	0.016	0.0055	0.0	0.074
600	0.024	4.63	0.021	0.040	0.018	0.016	0.0043	0.000023	0.066
700	0.018	4.63	0.016	0.040	0.014	0.016	0.0033	0.00058	0.053
800	0.014	4.63	0.013	0.040	0.011	0.016	0.0026	0.0037	0.033
900	0.011	4.63	0.0094	0.040	0.0081	0.016	0.0020	0.0071	0.021

Table 4.2 Discovery significances $Z = s/\sqrt{s+b}$ obtained after three selections, where cut 1 is $p_t^{\ell_1} > 400$, cut 2 is $p_t^{\ell_2} > 200$, and cut 3 is $m_\eta - 100 \text{ GeV} < M(\ell_1^+ \ell_1^- \ell_2^+ \ell_2^-) < m_\eta + 10 \text{ GeV}$.

higher integrated luminosity is achieved. Nevertheless, we proceed with the cut and count to illustrate possible avenues for future high luminosity colliders. In table 4.2, in particular, we note the 500 GeV mass case, where all background events may be eliminated by the cuts presented here. While this still leads to a small significance due to the sheer paucity of signal, one could imagine a scenario where a high enough luminosity yields reasonable significance in that mass region.

4.4 Conclusion

This chapter focused on a minimal composite Higgs model, $SU(4)/Sp(4)$, which we used as an example to illustrate the key features of a compositeness theory. While the Higgs couplings emerge from the chiral Lagrangian, linear couplings of the η state to fermions and gauge bosons rely on explicit breaking terms to generate them, underlining the need for both spontaneous and explicit symmetry breaking in such a theory.

In an investigation of the $SU(4)/Sp(4)$ phenomenology prospects, we examined the potential for a heavy η search at a future lepton collider, which must necessarily have a large collision energy. In addition to the fermiophobic scenario we investigated the all-couplings (fermiophilic) case, but the lepton collider results were found to be equally poor, with very few signal events present as in the fermiophobic case.

Moreover, a naive investigation of the proton-proton production of an η pair decaying to four tops at the HL-LHC yields fewer than one signal event. We find, then, that the examination of a heavy η at a future lepton collider will necessitate a much larger luminosity than is currently forecast for the higher energy lepton colliders, and may therefore remain out of bounds. This study was a naive one, relying on orders of magnitude and simple background estimations to gain an understanding of how realistic such a search for heavy η may be. We find that, while the background is well distinguished from the signal in the kinematic distributions, we are again in a scenario with very few signal results. It would appear from these results that the currently projected CLIC luminosities would not be sufficient to warrant such a search.

In this chapter and the one preceding it, we have presented a wide range of phenomenology emerging from models of compositeness. While a large range of models is possible, it is evident that many model-independent similarities are also shared between them. Having studied in detail several composite Higgs group structures, we now turn to dark matter, and examine how an extension of the scalar sector may resolve the outstanding question of its nature.

Chapter 5

Top-philic dark matter in a composite model

Of all the reasons to pursue extensions or modifications to the SM, the problem of dark matter is arguably the least abstract. While the hierarchy problem motivating the previous sections is one of symmetries and subtleties, it is hard to overlook the fact that about 26% of the universe's energy budget is made up of matter which cannot fit into the SM. Such is the nature of the prize that BSM theories work hard to include predictions for dark matter into their models. A number of candidates have emerged in recent years, which are split into non-particle and particle solutions. Candidates for the former category include MAAssive Compact Halo Objects (MACHOS), which are astronomical bodies such as neutron stars made of ordinary baryonic matter and have largely been excluded as dark matter candidates [147], or modified gravity. Particle candidates for dark matter include sterile neutrinos, axions, and Weakly Interacting Massive Particles (WIMPS). In the following, we will motivate the inclusion of a WIMP in a composite Higgs model. While a number of composite Higgs models incorporate a light dark matter candidate as a pNGB of the theory [62, 148, 149], this is heavily model-dependent, and many of the most elementary models do not include such a candidate. In the following, we will instead motivate the inclusion of a dark matter candidate as a heavy scalar resonance of the theory. This novel approach, as opposed to the well studied pNGB dark matter approach, has the advantage that it may be included in a composite Higgs model featuring any coset of choice. Like many other models, we include a \mathbb{Z}_2 symmetry in the theory, under which the dark matter candidate will be odd, and all SM particles will be even. The candidate is top-philic, and its effective model was proposed in Refs. [150, 151]. Here, we extend the model by motivating that the candidate be situated within a composite Higgs model, by

including a dimension-five contact operator and interaction with a top partner. Such dimension-five couplings are characteristic of strongly interacting BSM theories, where the higher order operators are not suppressed in the low energy regime due to the emergence of features such as anomalous dimensions.

Dark matter has been known of and observed for several decades. It was initially hypothesised by Fritz Zwicky in 1937 [152], but the first direct evidence was published by Vera Rubin in 1970 [153] in observations of the Andromeda spiral galaxy. This showed that the rotations of the spiral galaxies could not be explained by the luminous matter alone, as the radial velocity of the matter observed did not follow the expected distribution. The phenomenon could be explained by the inclusion of a halo of additional matter throughout the galaxy. Further evidence emerged through the observation of elliptical galaxies [154] and through gravitational lensing [155, 156]. Since then, compelling evidence [157–159] has been established for the existence of dark matter, and the quest to identify it has become one of the foremost goals of particle physics.

A leading branch of particle dark matter solutions is that of “cold” dark matter, which postulates that the dark matter has been non-relativistic since the earliest galaxies formed, with its evolution as the universe expands governed by the Boltzmann equation. In the early universe, SM particles and dark matter were in thermal equilibrium. As the universe expanded and thereby cooled, the dark matter collisions dropped to the rate of the Hubble expansion, at which point the particles “froze out” and decoupled, and the observed dark matter density, or relic density $\Omega_{DM}h^2$, became constant. Dark matter therefore continues to be non-relativistic to present day. Had the dark matter not decoupled from the thermal bath, it would have no relic abundance today, having rapidly annihilated or decayed when it was no longer relativistic. Any model featuring candidates for cold non-baryonic dark matter is therefore strongly constrained by the relic density which should be satisfied, which has been measured to be [160]

$$\Omega_{DM}h^2 = 0.1186 \pm 0.0020, \quad (5.1)$$

and which is controlled by the annihilation cross section of the dark matter candidate. This relic abundance is a crucial number which must be matched by any successful dark matter theory. A dark matter candidate which does not interact with any other particle would maintain a number density equal to its initial value, and be slowly diluted by the expansion of the universe.

A number of candidates for dark matter have been proposed, but the WIMP, coupling to the SM through a weak interaction with masses ranging from several GeV to a few TeV [161], continues to be of interest. There is, of course, no generic reason for a dark matter candidate to couple to the SM, but we postulate (and hope) that it does. In this work we model a dark matter S coupling to the SM top sector via a heavy fermionic mediator T via a t -channel interaction, as the mediator is also \mathbb{Z}_2 -odd. This mediator T is a coloured VLQ, and such a fermion is a feature of many BSM models facilitating interactions between the dark matter sector and the SM. Direct detection, indirect detection and colliders are complementary probes of this model.

We have constrained the mass of our real scalar dark matter particle S to have a mass larger than that of the top quark, focusing on candidates S with $200 \text{ GeV} \lesssim m_S \lesssim 3 \text{ TeV}$. Like the dark matter candidate, the heavy mediator T is postulated to be a resonance emerging from a composite Higgs model. For this reason, we constrain m_T to be at most one order of magnitude larger than m_S as we expect bound-state resonances to be similar in mass. This is much heavier than the typical mass of a pNGB, where we envision that the mass of these resonances lie near to the compositeness scale. In this mass range the dark matter annihilation $SS \rightarrow tt$ dominates, and the threshold effects which would arise in m_S and m_t mass-degenerate regimes can be avoided. Recent investigations [150, 151] have shown that next-to-leading-order (NLO) corrections to the annihilation cross section lead to significant modifications in the relevant parameter space, and should not be neglected for heavy dark matter. Up to this point in this thesis, we have only considered the first term in the perturbative QCD expansion in α_s at the partonic scattering level when calculating the cross section. In addition to those leading order (LO) terms we now move to next-to-leading-order (NLO) considerations which include both the first and second terms in that series. Truncating the series introduces uncertainties into theoretical predictions, so NLO computations are more precise than their corresponding LO results, but are sometimes negligibly different to LO calculations and are often computationally heavy.

In constructing such a model with a scalar S with odd parity we can draw inspiration from a \mathbb{Z}_2 symmetric Higgs portal theory [162–167], a well-studied simple extension of the scalar sector by adding to the SM a \mathbb{Z}_2 symmetry and an additional scalar, S . If S is heavier than $m_H/2$ and \mathbb{Z}_2 -odd, it can be a dark matter candidate. This theory is phenomenologically challenging with the sole S communication with the SM facilitated through the Higgs sector. The addition of a heavy mediator T , also \mathbb{Z}_2 -odd, allows for an additional coupling to the SM through the top sector, and further

enhances the potential phenomenology. We may also imagine situating these new resonances within a composite Higgs model, where energy scales are on the order of the compositeness scale $\Lambda \sim 5 - 10$ TeV and the symmetry breaking scale $f \sim 1$ TeV. We keep this in mind when considering the size of the C/Λ parameter discussed below, and when discussing the mass of S and T , which should not be too far from the scale of the breaking f if they are both to be composite resonances. Additionally, we could envisage adding one more VLQ, T' , which would act as a \mathbb{Z}_2 -even top partner and form part of a very basic composite Higgs set-up. This addition will be discussed at the end of this chapter, and for simplicity we begin with the addition of S and T to the SM Lagrangian, and assess the behaviour of the model due to the dimension-five term. In contrast to the \mathbb{Z}_2 symmetric Higgs portal theories, we turn the loop-generated Higgs- S connection off, and allow the sole communication to the SM to proceed via the top coupling in order to focus on the phenomenology arising from the presence of the vector-like mediator. The removal of the term $\frac{1}{2}\lambda S^2\phi^\dagger\phi$ is motivated in Ref. [150]. Many scalar dark matter models including a t -channel fermionic mediator have previously been studied [168–171], as have top-philic dark matter models [172–177, 170, 178] and heavy dark matter with masses ranging up to several TeV have been discussed in the literature [179]. However, the situation of such candidates within a composite Higgs model have, to our knowledge, not been attempted. We begin this endeavour with the inclusion of a generic dimension-five operator, which is a common feature of a broad range of BSM theories. For models emerging from strong dynamics where higher dimensional operators do not decouple [180], such as the composite Higgs models at hand, those higher dimensional operators may be relevant at colliders and in detection experiments. Instead of focusing on a particular theory, we have constructed an effective theory by adding to the existing models [150, 151] an additional contact interaction through a dimension-five operator $SS\bar{t}t$ with an unknown $\mathcal{O}(1)$ coefficient C . The sign and magnitude of this Wilson coefficient, which is dependent on the underlying model, could substantially modify the existing limits obtained through only dimension-four operators constrained by a Yukawa-like coupling \tilde{y}_t . Recall also from earlier discussions of EFTs that the dimension-five operator will be attached to a factor of $1/\Lambda$ for dimensional reasons.

In the following, we begin by outlining the effective theory in section 5.1, including an investigation of the relic density and an analytical fit to the simulated data. We then investigate direct and indirect detection in sections 5.3 and 5.4 respectively, and

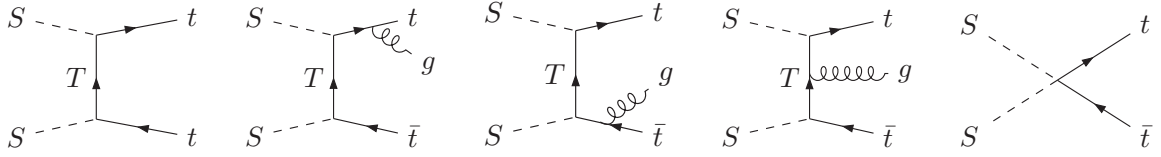


Fig. 5.1 Feynman t -channel diagrams depicting the diagrams contributing to the relic density calculation. The LO (left), contact term (right) and NLO contributions (middle) are displayed, where the second and third diagrams feature final state radiation (FSR) and the fourth diagram displays an example of virtual internal bremsstrahlung (VIB). The final diagram is due to the contact term.

examining the collider constraints in section 5.5. Finally, we add to the model a top partner and discuss potential phenomenology in section 5.7.

5.1 Heavy dark matter and a t -channel mediator

We begin by an examination of the Lagrangian dictating the effective model, featuring the interaction of the \mathbb{Z}_2 -odd sector with the SM states. The heavy T mediates interactions between the dark matter candidate and the SM through the operator STt [150, 151], and the additional contact term $SS\bar{t}t$ is included. Thus, we add to the SM the minimal Lagrangian

$$\mathcal{L} = i\bar{T}\not{\partial}T - m_T\bar{T}T + \frac{1}{2}\partial_\mu S\partial^\mu S - \frac{1}{2}m_S^2 S^2 + [\tilde{y}_t S\bar{T}P_R t + h.c.] + \frac{C}{\Lambda}SS\bar{t}t, \quad (5.2)$$

where m_T is the mass of the mediator, and m_S is the mass of the dark matter candidate. The STt vertex mediating the t -channel interaction is parametrised by a Yukawa-type parameter \tilde{y}_t . Building on the previous models, the contact term $(C/\Lambda)SS\bar{t}t$ has an associated Wilson coefficient of $\mathcal{O}(1)$, C . As before, Λ parametrises the scale of the effective theory, such as the compositeness scale.

Diagrams relevant for the calculation of the relic density mediating the interaction $SS \rightarrow t\bar{t}$ are shown in fig. 5.1, where the first four diagrams are relevant to the NLO cross section shown by previous authors to be non-negligible [150, 151]. This full cross section σv_{NLO} , excluding the dimension-five term contribution, can be well approximated by a sum of the leading order cross section $\sigma v_{q\bar{q}}$ and the cross section related to virtual internal Bremsstrahlung $\sigma v_{VIB}^{(0)}$ [151]

$$\sigma v_{NLO} \approx \sigma v_{q\bar{q}} + \sigma v_{VIB}^{(0)}, \quad (5.3)$$

where

$$\sigma v_{t\bar{t}} = \frac{y_F^4 N_c}{4\pi m_S^3} \frac{m_t^2 (m_S^2 - m_q^2)^{3/2}}{(m_S^2 + m_T^2 - m_t^2)^2} \quad (5.4)$$

and

$$\begin{aligned} \sigma v_{VIB}^{(0)} = \frac{N_c \tilde{y}_t^4}{8\pi m_S^2} \frac{\alpha_S C_F}{\pi} \left[(r' + 1) \left(\frac{\pi^2}{6} - \log^2 \frac{1+r'}{2r'} - 2\text{Li}_2 \left(\frac{1+r'^2}{2r'} \right) \right) \right. \\ \left. + \frac{4r'^2 + 3}{r'^2 + 1} + \frac{4(r' - 3r' - 1)}{2r'} \log \frac{(r' - 1)}{r' + 1} \right], \end{aligned} \quad (5.5)$$

where m_t is the mass of the top quark, and $r' \equiv m_T^2/m_S^2$. Additionally, N_c denotes the number of colours, and Li_2 denotes a dilogarithm. The structure of the NLO cross section is such that it is undefined for $m_S > m_T$, as a dark matter candidate cannot be heavier than another \mathbb{Z}_2 -odd state.

The final diagram in fig. 5.1, emerging from the $SS\bar{t}t$ term, will modify the relic density, and possibly the detection prospects, perhaps in a non-negligible way. The general form of the matrix element owing to the cross section from this term is

$$\mathcal{M} = \frac{C}{\Lambda} (\bar{u}_1 \Gamma \nu_2), \quad (5.6)$$

and where the generic Γ is the identity or γ^5 in order to avoid uncontracted Lorentz indices. After considering what kind of mediator would lend itself to producing a γ^5 at the vertex, which would then lead to two γ^5 in the effective operator, we settle on the scalar vertex being the only plausible choice, much as in standard ϕ^4 theory. The full matrix element is written as

$$-i\mathcal{M} = \bar{u}(p_1) \Gamma \delta_{ij} \left(-i \frac{C}{\Lambda} \right) v(p_2), \quad (5.7)$$

where δ_{ij} carries the $SU(3)$ structure of the outgoing quarks. The calculation of the amplitude is as follows:

$$\begin{aligned} \sum_{\text{colours}} |\mathcal{M}|^2 &= \left(\frac{C}{\Lambda} \right)^2 \sum [\bar{u}(p_1) \Gamma t^A (p_2)] [\bar{u}(p_1) \Gamma t^B v(p_2)]^\dagger \\ &= 2 \left(\frac{C}{\Lambda} \right)^2 N_c (s - 4m^2). \end{aligned} \quad (5.8)$$

Then the s -wave contribution to the cross section can be written as

$$\begin{aligned}
 a &= \frac{1}{m_S^2} \left(\frac{N_c}{32\pi} \sqrt{1 - \frac{4m_t^2}{s}} \frac{1}{2} \int_{-1}^1 d\cos\theta |\mathcal{M}|^2 \right)_{s=4m_S^2} \\
 \implies \langle\sigma v\rangle_{SStt} &= \left(\frac{C}{\Lambda}\right)^2 \frac{N_c}{4\pi} \left(1 - \frac{m_t^2}{m_S^2}\right)^{3/2} + \mathcal{O}(v^2),
 \end{aligned} \tag{5.9}$$

where the thermally averaged cross section then emerges as $\langle\sigma v\rangle_{SStt}$. In principle, the relic density contains dimension-four contributions, dimension-five squared contributions, and their interference. In adding the contact term contribution to the cross section, the interference between the dimension-five amplitude and the leading order amplitude is found to be at most 2 %. This means that the thermally averaged cross section contributions are additive to a good approximation, and interference is neglected in the following.

As a first investigation, we aim to investigate the modification of the parameter space due to the addition of the contact term. In order to simulate the dark matter relic density including the desired NLO effects, we have employed the MICROMEGAS [181] framework to determine the relic density numerically after the construction of a FEYNRULES [182] model file. The CALCHEP [183] model file was generated using the FEYNRULES/CALCHEP interface [184]. The MICROMEGAS framework allows for the computation of the relic density of a cold dark matter candidate obeying a discrete symmetry, including all relevant annihilation and co-annihilation channels.

MICROMEGAS calculates the relic density by utilising the precise relativistic single-integral formula for the velocity averaged cross section, and solving the corresponding Boltzmann equation to estimate the abundance of dark matter at the present time [185]. For this, the code relies on the computation of the matrix elements by CALCHEP. In this work, we have improved the estimation of $\langle\sigma v\rangle$ by including the NLO form of the cross section within the framework. The free parameters of the scan are varied with m_S (m_T) between 200 GeV and 3000 GeV (3500 GeV), $\tilde{y}_t \in [10^{-4}, 6]$, and $C/\Lambda \in [10^{-3}, 10^{-5}] \text{ GeV}^{-1}$. The scan ranges for the masses are chosen such that both masses lie above the mass of the top quark, and up to an envisioned compositeness scale, which typically lies around 3 TeV. The Yukawa parameter bounds are borrowed from previous investigations [150]. Finally, to establish the bounds for the contact term coefficient, we checked the values of C/Λ supplanting the Yukawa term ($\tilde{y}_t \sim 0$) in producing the correct relic density, as well as the largest value of C/Λ which does not modify the relic density due to the Yukawa term.

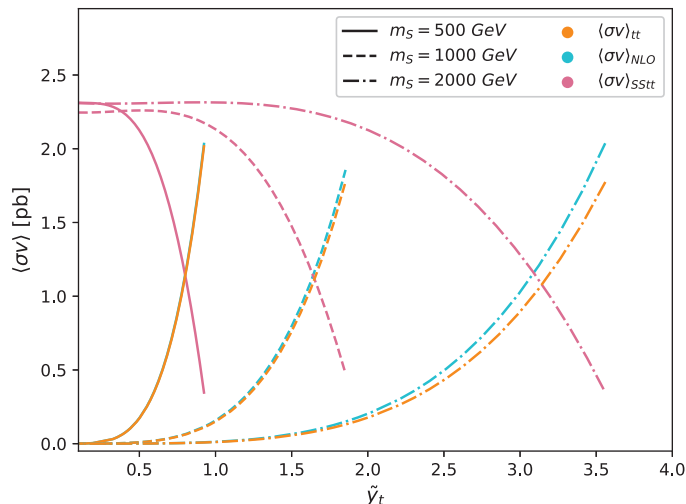


Fig. 5.2 A comparison of the cross sections against the strength of the Yukawa coupling \tilde{y}_t , showing the interplay of the dimension-five, NLO, and LO cross sections. The deviation of the NLO away from the leading order contribution is apparent from roughly 1 TeV. All points yield the correct relic density.

In fig. 5.2, we show the relative contributions of the LO, NLO, and dimension-five cross sections for a sample of three dark matter masses. In each, the mass of the mediator is fixed such that $r = m_T/m_S - 1 = 0.6$. The Yukawa coupling was varied, and the C/Λ coefficient was updated to match the relic density observed in the universe. The interplay between the cross sections is clear, with the contact term taking over from the Yukawa term for low \tilde{y}_t . The maximum strength of the contact term is on the order of $C/\Lambda \simeq 0.2 \text{ TeV}^{-1}$ (or less, if the cross section is dominated by the NLO contribution). It is clear that the inclusion of the contact term extends the parameter space by allowing smaller values of the Yukawa parameter. In the following section, we determine a semi-analytic approximation for the value of C/Λ required to reproduce the observed dark matter relic density of S , mapping the interplay between the variables.

5.2 Fitting the relic density curve

The relic abundance of dark matter is governed by the simple Boltzmann equation [186]

$$\frac{dn}{dt} = -3Hn - \langle\sigma_{eff}v\rangle (n^2 - n_{eq}^2), \quad (5.10)$$

where H is the Hubble parameter, n is the number density of the dark matter, and n_{eq} is the equilibrium number density. In its entirety, the abundance of S can be obtained through solving the Boltzmann equation, yielding [187]

$$\Omega_{DM}h^2 \approx \frac{1.04 \times 10^9}{M_{Pl}} \frac{x_F}{\sqrt{g_*(x_F)}} \frac{1}{a + 3b/x_F}, \quad (5.11)$$

for $\langle\sigma v\rangle = a + \mathcal{O}(v^2)$, where M_{Pl} is the Planck mass, g_* is the total number of effectively massless degrees of freedom, and x_F is the freeze-out temperature. The a and b coefficients are functions of the masses in the theory, and emerge from the non-relativistic annihilation cross section, which is expanded as

$$\langle\sigma v\rangle = a + b\langle v^2\rangle. \quad (5.12)$$

The annihilation rate features contributions from partial waves of the scattering amplitude, where the first term on the right hand side of eq. (5.12) corresponds to the velocity-dependent s -wave term, and the second represents the p -wave contribution, and scales with v^2 . In simple dark matter models, the s -wave contribution to the annihilation cross section dominates, and higher partial waves are minimal [188]. Given, then, that the relic density depends inversely on the annihilation cross section

$$\Omega_{DM}h^2 \propto \langle\sigma v\rangle_{full}^{-1}, \quad (5.13)$$

we may write

$$\Omega_{DM}h^2 \sim \frac{b'(x_F, g_*(x_F))}{\langle\sigma v\rangle_{full}} = \frac{b'(x_F, g_*(x_F))}{C^2/\Lambda^2 \langle\sigma v\rangle_{SStt} + y^4 \langle\sigma v\rangle_{NLO}}. \quad (5.14)$$

As the full thermally averaged cross section has been written as the sum of its components, it follows that

$$\frac{C^2}{\Lambda^2} = \frac{1}{\sqrt{\langle\sigma v\rangle_{SStt}}} \sqrt{\frac{b'(x_F, g_*(x_F))}{\Omega_{DM}h^2} - y^4 \langle\sigma v\rangle_{NLO}}. \quad (5.15)$$

This is the motivation for the fit to the relic density being pursued, as the relationship between the dimension-five term coefficient and the Yukawa coefficient appears clearly defined. The relation between C/Λ and \tilde{y}_t is presented in fig. 5.3, where the slope depends on both m_S and m_T for its shape, and each point matches the relic density

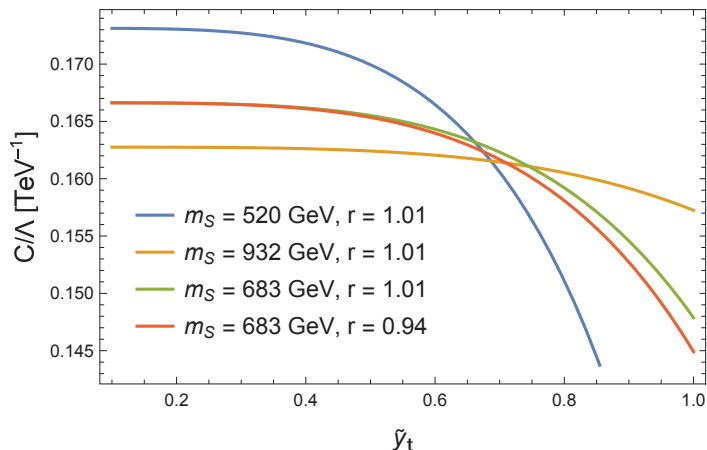


Fig. 5.3 A comparison of the \tilde{y}_t vs C/Λ curve yielding the correct relic density for a number of benchmarks, where the function is defined $f(r, m_S, \tilde{y}_t)$. A consistently shaped curve is observable, but the gradient and shift of the curve is clearly dependent on the mass parameters m_S and r .

given by Planck data. The function in fig. 5.3 is of the form

$$\frac{C}{\Lambda} = f(m_S, m_T, \tilde{y}_T), \quad (5.16)$$

where the function f is to be determined.

In fig. 5.3, the function is studied for a number of benchmarks, with the mass ratio held relatively constant. In these scenarios the masses are well separated. Notably, it is the value of m_S which determines the size of the dimension-five coupling which takes over entirely from the Yukawa term. This is expected, as the mediator T does not feature in the dimension-five cross section. The dependence is visible in the green and red lines, where a modified mass ratio changes the slope but not the y -axis intersection of the curves. In fig. 5.3 it is also evident that the modified m_S with constant r changes the y -axis intersection.

The dependence on the couplings \tilde{y}_t and C/Λ can be factored out, so that

$$\langle\sigma v\rangle_{NLO} = \tilde{y}_t^4 B(m_S, m_T) \quad \text{and} \quad \langle\sigma v\rangle_{SStt} = (C/\Lambda)^2 A(m_S). \quad (5.17)$$

We are thus able to determine the relationship between the four parameters $(m_S, m_T, \tilde{y}_t, C/\Lambda)$;

$$c = \frac{C}{\Lambda} = f(r, m_S, \tilde{y}_t) = \frac{1}{A(m_S)} \sqrt{b - B(m_S, m_T)} \tilde{y}_t^4. \quad (5.18)$$

The mass-defined functions $A(m_S)$ and $B(m_S, m_T)$ are given below, obtainable directly from eqs. (5.3) and (5.9);

$$\begin{aligned}
A(m_S) &= \frac{\Lambda^2 \langle \sigma v \rangle_{SStt}}{C^2} = \frac{N_c}{4\pi} \left(1 - \frac{m_t^2}{m_S^2} \right)^{3/2}, \\
B(m_S, m_T) &= \frac{\sigma v_{q\bar{q}} + \sigma v_{VIB}^{(0)}}{\tilde{y}_t^4} \\
&= \frac{N_c}{4\pi m_S^2} \left(\frac{m_t^2 (m_S^2 - m_t^2)^{3/2}}{m_S (m_S^2 + m_T^2 - m_t^2)^2} \right. \\
&\quad \left. + \frac{\alpha_S C_F}{2\pi} \left[(r' + 1) \left(\frac{\pi^2}{6} - \log^2 \frac{1+r'}{2r'} - 2\text{Li}_2 \left(\frac{1+r'}{2r'} \right) \right) \right. \right. \\
&\quad \left. \left. + \frac{4r'+3}{r'+1} + \frac{4(r+1)^2 - 3r' - 1}{2r'} \log \frac{r'-1}{r'+1} \right] \right), \\
b'(x_F, g_*(x_F)) &= \left(7.19 \times 10^{-10} \text{ GeV}^{-2} \right) \frac{x_F}{\sqrt{g_*(x_F)}}.
\end{aligned} \tag{5.19}$$

The parameter b' was found from the fit in all cases to be

$$(6.00 \times \pm 0.2) \times 10^{-9}.$$

The constant nature of this parameter is expected from eq. (5.11).

5.2.1 Parametrising the shift due to coannihilations

The result in eq. (5.18) neglects the presence of coannihilations, which should be considered when S and T are nearly mass-degenerate. In this case, the relic abundance of dark matter is not only controlled by the process $\sigma(SS \rightarrow \text{SM})$, but also by $\sigma(ST \rightarrow \text{SM})$. The rate of annihilation of dark matter may then also be indirectly impacted by annihilations of the mediator, $\sigma(TT \rightarrow \text{SM})$. This phenomenon modifies the behaviour of the relic density, since it is not only the self-annihilations $SS \rightarrow TT$ controlling the abundance of S . While the simulation by MICROMEGAS handles coannihilation effects, the function in eq. (5.18) leads to an underfitting of the data, visible as the red lines in the first three panels of fig. 5.4, which shows the behaviour of the curve for constant m_S and varying m_T . The figure displays good agreement for greater m_T , but when the mass difference between S and T is small the function deviates from the observed values which produce the correct relic density. The coannihilation effects become increasingly large for smaller r , as visible in fig. 5.4. For smaller values of r (where the ‘‘smallness’’ that is relevant depends on the masses of

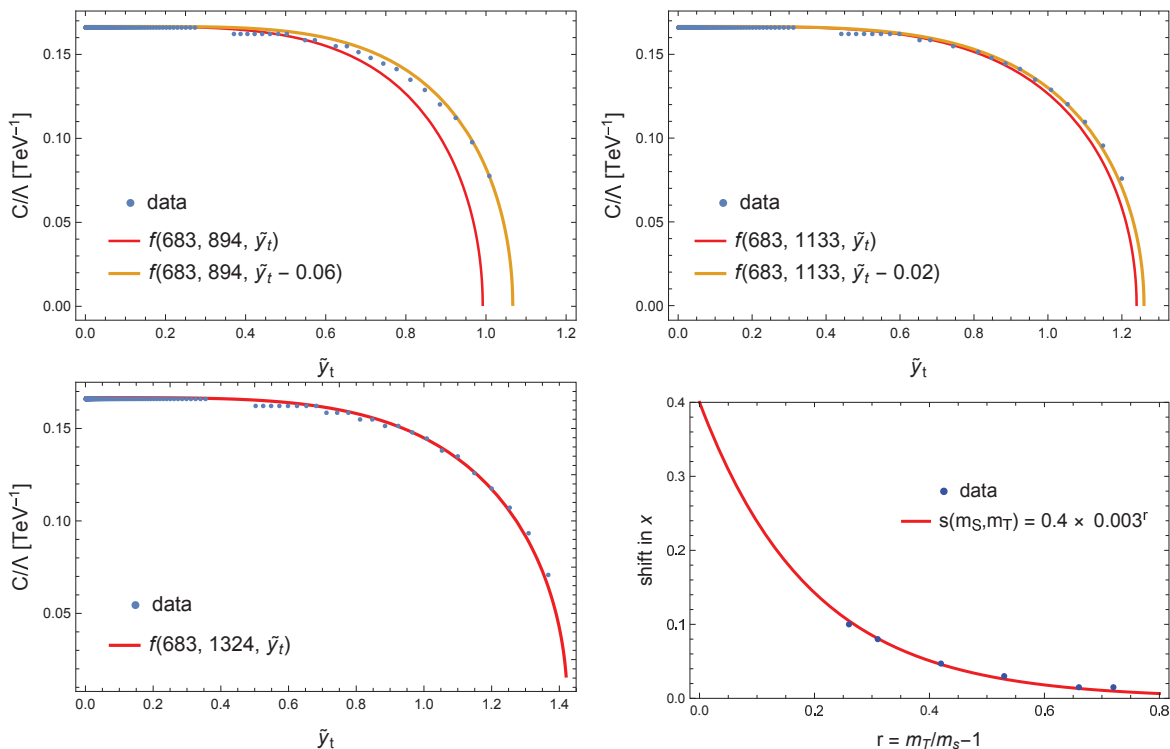


Fig. 5.4 The functional fit is displayed for an example mass benchmark, $m_S = 682.6$ GeV, with varying r values (top row and bottom left plot), and the corresponding exponential fit to the deviation (bottom right). The bottom right plot shows that the deviation follows a decreasing exponential, where smaller r necessitates larger shifts in \tilde{y}_t , and the shift becomes negligible above $r = 0.8$.

the particles), we find that the data is subject to a shift in \tilde{y}_t . The function can be shifted in the positive x direction (that is, in \tilde{y}_t) in order to re-establish agreement with the simulated data, indicated by the yellow line. These coannihilation effects can also be treated semi-analytically.

The calculation of the relic density [187] can be modified to the coannihilation case in a generalised fashion [189, 186, 190] according to the Boltzmann equation given in eq. (5.11), where $\langle\sigma_{eff}v\rangle$ replaces the annihilation cross section with

$$\begin{aligned}
 \sigma_{eff}(x) &= \sum_{ij} \sigma_{ij} \frac{g_i g_j}{g_{eff}^2} (1+r_i)^{3/2} (1+r_j)^{3/2} \exp(-x(r_i+r_j)), \\
 g_{eff}(x) &= \sum_{i=1}^N g_i (1+r_i)^{3/2} \exp(-x r_i), \\
 r_i &= \frac{m_i}{m_S} - 1,
 \end{aligned} \tag{5.20}$$

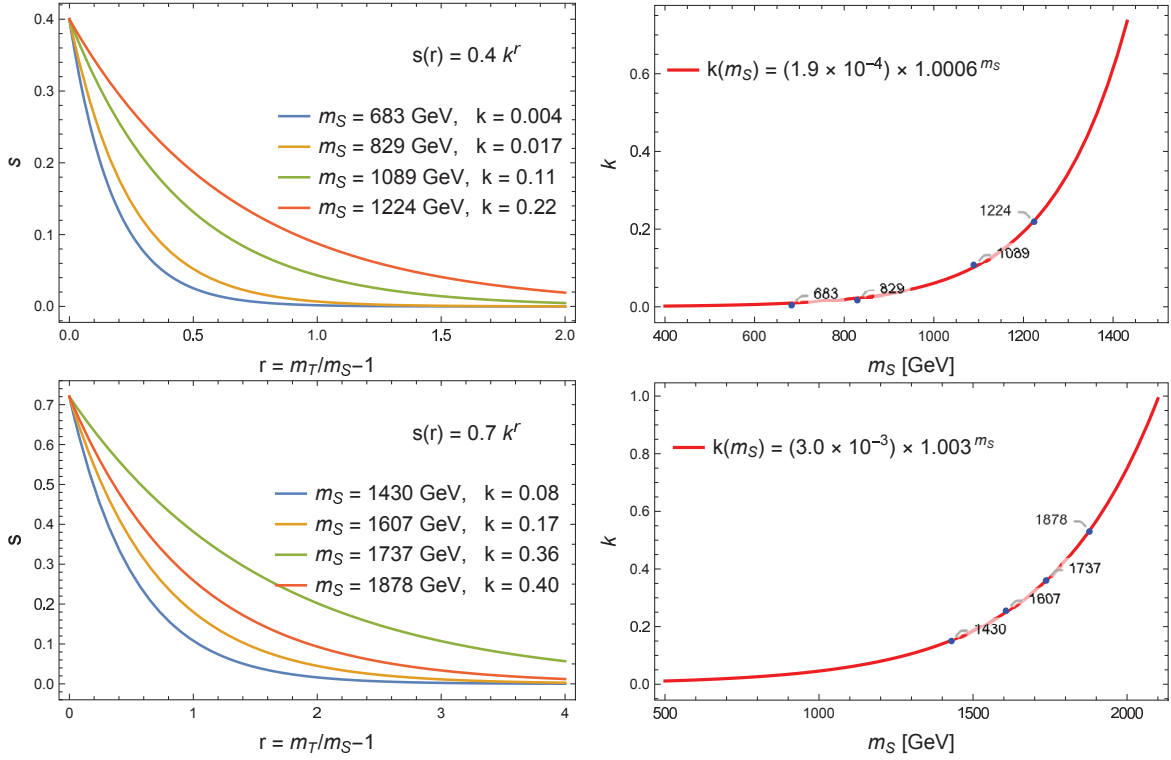


Fig. 5.5 Top row: the left plot shows the deviation function (analogous to fig. 5.4) for several m_S benchmark points, each following the function $s(r) = 0.4 k^r$. The right plot fits the value of k across the mass points, again finding an exponential structure. The bottom row shows the analogous plot for the higher mass fits, with $s(r) = 0.72 k^r$

for $x = m_S/T^*$, where T^* is the temperature. Here, $\sigma_{ij} \equiv \sigma(\chi_i \chi_j \rightarrow \text{SM})$ for states χ_i with g_i internal degrees of freedom. In this case, with only two states $S = \chi_i$ and $T = \chi_j$ being relevant, the effective annihilation cross section which governs the additional coannihilations simplifies to

$$\sigma_{eff}(x) = \sigma_{SS} + \sigma_{ST} \frac{g_S g_T}{g_{eff}^2} \left(\frac{m_T}{m_S} \right)^{3/2} \exp[-x r], \quad (5.21)$$

where $\sigma_{ST} \propto \tilde{y}_t^2$. It is apparent from the form of this function that we may expect exponentially larger deviations from the fit for smaller r .

In examining the behaviour of the deviations, we observe two separate regimes separated around 1 TeV. The separation of behaviours at approximately 1 TeV is motivated by the NLO behaviour of the system. Below 1 TeV, NLO effects are sub-dominant, and appear only above 1 TeV, where influences by VIB become apparent. In fig. 5.5, we examine a number of m_S benchmarks across the r range of interest, measuring their shifts (left) and plotting the behaviour of the shifts against

the scalar mass m_S . Separating the mass regimes at 1 TeV, we find that the shift s for a mass point (m_S, m_T) takes the form

$$s(m_S, m_T) = \begin{cases} 0.4k^r & m_S \leq 1.2 \text{ TeV} \\ 0.7k^r & m_S > 1.2 \text{ TeV} \end{cases}, \quad (5.22)$$

where $k(m_S)$ is an unconstrained parameter of dimension 1 which is constant for a given scalar mass. The value of k was determined from a fit to a number of data points. In fact, we find that the value for $k(m_S)$ may also be fit to a function, where

$$k(m_S) = \begin{cases} (1.9 \times 10^{-4}) (6.2 \times 10^8)^{m_S/\Lambda} & m_S \leq 1.2 \text{ TeV} \\ (3.0 \times 10^{-3}) (1.8 \times 10^4)^{m_S/\Lambda} & m_S > 1.2 \text{ TeV} \end{cases}, \quad (5.23)$$

for $\Lambda = 3.5 \text{ TeV}$, which is the maximum value for m_T used in the parameter scan, and which provides an indication of the scale of the effective theory. With the full semi-analytical fit now in hand, we replace eq. (5.18) by

$$\frac{C}{\Lambda} \approx f(m_S, m_T, \tilde{y}_t) = \frac{1}{\sqrt{A(m_S)}} \sqrt{b' - B(m_S, m_T) \left(\tilde{y}_t - \alpha \left[\beta \gamma \frac{m_S}{\Lambda} \right]^r \right)^4}, \quad (5.24)$$

where $A(m_S)$ and $B(m_S, m_T)$ are as in eq. (5.19). As presented in eqs. (5.22) and (5.23), the other coefficients which parametrise the co-annihilation effects are fitted to $(\alpha, \beta, \gamma) = (0.4, 1.9 \times 10^{-4}, 6.2 \times 10^8)$ for $m_S \leq 1.2 \text{ TeV}$, and $(\alpha, \beta, \gamma) = (0.7, 3.0 \times 10^{-3}, 1.8 \times 10^4)$ for $m_S > 1.2 \text{ TeV}$. In fig. 5.6, we present on the left the curves for the benchmark point $m_S = 1089 \text{ GeV}$, including shifts agreeing with data. The right-sided plot of the figure presents a number of mass benchmarks, displaying the simulated data and an ‘unseen’ fit showing good agreement. In the following sections, we move to an examination of the astrophysical constraints for the dark matter candidate, beginning with direct detection.

5.3 Direct detection constraints

Detection of dark matter via ‘direct’ experimental methods relies on the scattering of dark matter off SM nuclei. The absence of valence top quarks in protons and neutrons means that the scattering rate will be controlled only through the interactions between the gluon and dark matter which arise at loop level, illustrated in fig. 5.7.

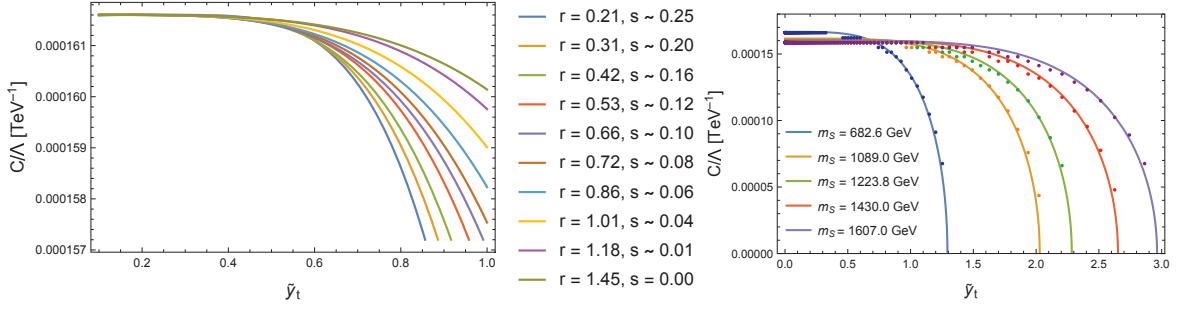


Fig. 5.6 The coefficient curves for mass point $m_S = 1089$ GeV for varying m_T , left, and the coefficient curves including coannihilation shifts for a range of mass benchmarks all with $\frac{m_T}{m_S} - 1 = 0.72$, right. As the masses move towards degeneracy, the curves become steeper, but the value of c which takes over from the Yukawa term remains constant due to its m_S dependence. Note there is a slight under estimation by the curves relative to the dots.

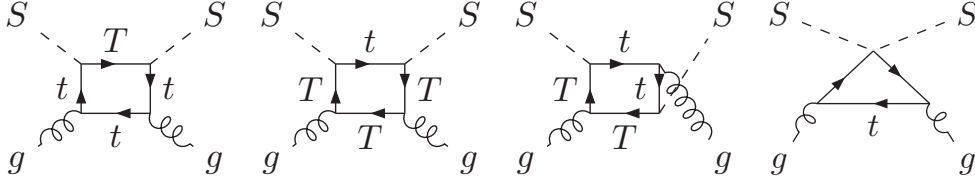


Fig. 5.7 Feynman diagrams to be considered in coupling the dark matter candidate to a nucleus via the gluons, where the final diagram emerges after the addition of the dimension-five operator.

Given the addition of the dimension-five contact term, an additional interaction arising through the fourth diagram in fig. 5.7 should be considered.

The dark matter scattering rate can be obtained in the following manner; first, we calculate the effective operators in the EFT by integrating out the heavy particles (in our case, by integrating out T). The Wilson coefficients of the effective operators are then evolved according to the renormalisation group equations down to the scale $\mu_{had} \approx 1$ GeV, which is the scale at which the nucleon matrix elements are evaluated, using tree-level matching conditions. The DM-nucleon effective coupling is then expressed in terms of Wilson coefficients and the nucleon matrix elements. Terms proportional to the momentum transfer and velocity may be neglected [185].

In evaluating the scattering cross section with a nucleon we have followed Ref. [191], where in the case of a scalar dark matter candidate only the spin-independent cross section is relevant [191]. Since the low velocity of the dark matter leads to a small momentum transfer [192], the following effective Lagrangian fully describes the

interaction between the dark matter and nucleons

$$\mathcal{L} = C_S^g \mathcal{O}_S^g = C_S^g \frac{\alpha_s}{\pi} S^2 G^{\mu\nu} G_{\mu\nu}, \quad (5.25)$$

where the effective operators are defined at the mass scale of the mediators [191]. The interaction of the scalar boson ϕ with the nucleons is given by

$$\mathcal{L} = \bar{\psi}_T (1 + \gamma_5) \tilde{y}_t q \phi + \text{h.c.}, \quad (5.26)$$

where our vector-like mediator T is denoted ψ_T .

We begin by reproducing the results of Ref. [150] and neglecting the dimension-five coupling, obtaining the coefficient C_S^g by considering the loop-level amplitudes $f^{(i)}$ given in Ref. [191] which contribute to the DM-gluon scattering. In this case

$$C_S^g = \frac{\tilde{y}_t}{8} \left(f_+^{(a)}(m_S, m_t, m_T) + f_+^{(b)}(m_S, m_t, m_T) + f_+^{(c)}(m_S, m_t, m_T) \right), \quad (5.27)$$

where in our notation $a_Q = b_Q = \tilde{y}_t/2$ and the mass of the top quark is not negligible. Following the same method in adding the effective interaction due to the new diagram, the coupling to be added is written as

$$f^{d5}(m_t) = -\frac{C}{\Lambda} \int \frac{d^4 p}{(2\pi)^4} \text{Tr}[iS(p)]|_{GG}, \quad (5.28)$$

where the quark propagator in the gluon background is given as [193]

$$iS(p) = \int d^4 x e^{ipx} \langle T\{\psi(x)\bar{\psi}(0)\} \rangle. \quad (5.29)$$

In the limit of zero gluon momentum, the integral reduces to a factor of $1/m_t$ [193], such that $f^{d5} = -\frac{C}{\Lambda} \frac{1}{m_t}$. The spin-independent DM-nuclear cross section σ_A and DM-proton cross section σ_p can then be written as [191]

$$\sigma_A = \frac{1}{\pi} \left(\frac{m_A}{m_S + m_A} \right)^2 |n_p f_p + n_n f_n|^2, \quad \sigma_p = \frac{1}{\pi} \left(\frac{m_p}{m_S + m_p} \right)^2 f_p^2, \quad (5.30)$$

for n_p protons and n_n neutrons in a nucleus of mass m_A , where for a nucleon field N with only gluon interactions being relevant we have

$$f_N/m_N = -\frac{8}{9} C_S^g f_{T_G}^{(N)}, \quad f_{T_G}^{(N)} = 1 - \sum_{q=u,d,s} f_{T_q}^{(N)} \quad (5.31)$$

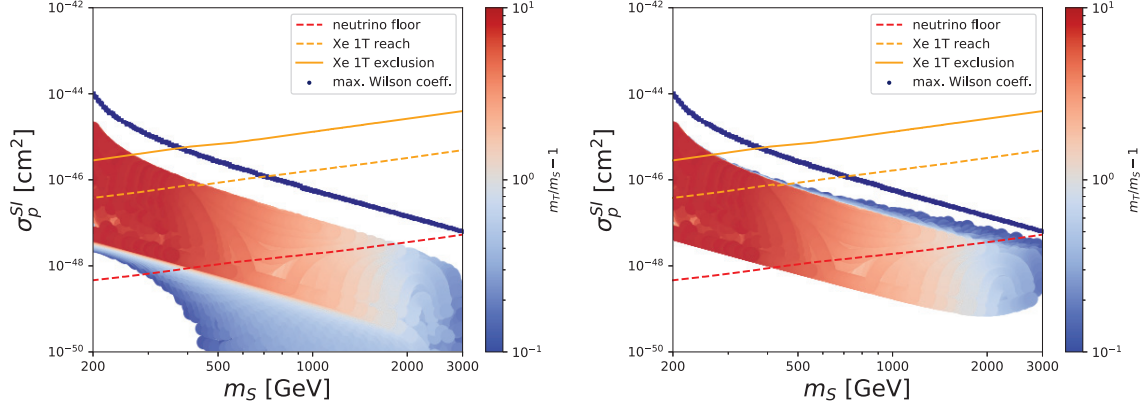


Fig. 5.8 The DM-proton cross section for negative (left) and positive (right) C/Λ considered separately, and for the maximum Yukawa value, where the combination of C/Λ and \tilde{y}_t in the plots give the correct relic density at a given mass. An interval of $m_T/m_S - 1 \in (0.1, 10)$ has been chosen, where the bottom limit ensures we are in a well-understood region, and the upper limit is chosen such that the scalar and fermionic resonances are not too different in mass. Additionally, we display the cross section obtained through use of the maximum possible Wilson coefficient $|C|$, which is displayed in bright blue, and dominates the contribution from the Yukawa term. Also displayed in the plot is the red dashed line representing the neutrino floor [194], the orange dashed line indicating the Xenon 1T reach [195], and the red solid line showing the 90% confidence exclusion of the Xenon 1T experiment [196].

with the mass fractions $f_{T_q}^{(N)}$ given in Ref. [191]. The contributions from the strong coupling constant are implicit in the definition of f_N .

The sign of the Wilson coefficient is not fixed at the EFT level, and the dark matter scattering cross section receives a contribution proportional to $-C/\Lambda$. In the following, we therefore consider both signs of C , which are displayed separately in the scattering cross section presented in fig. 5.8. The parameter space considered here results in non-zero contributions from both the dimension-five and Yukawa terms. Also indicated on the plots are detection bounds from the Xenon experiment and the neutrino floor, the latter of which represents a ‘hard limit’ for dark matter detection. Fig. 5.8 displays several limiting cases, all of which satisfy the correct relic density; the points indicated by the red/blue two-dimensional histogram indicate the cases where the coupling C/Λ is at its minimum value in the range $[10^{-5}, 10^{-3}]$, with the Yukawa coefficient being correspondingly at its highest value. It should be noted that the Wilson coefficient is non-zero. The value of the mass ratio r is indicated by the colour-scheme. Conversely, the dark blue line indicates the maximum C/Λ and minimum \tilde{y}_t value, where the dimension-five term takes over entirely from the Yukawa.

Exclusion	Max. \tilde{y}_t		Max. C/Λ	
	$C > 0$	$C < 0$	$C > 0$	$C < 0$
Xe-1T exclusion	248 GeV	246 GeV	376 GeV	
Xe-1T reach	405 GeV	393 GeV	706 GeV	
ν -floor	2476 GeV	1631 GeV	> 3000 GeV	

Table 5.1 The masses m_S at which the experimental bounds indicated in fig. 5.8 intersect the regions of interest defined by the coupling parameters.

Of course, there exist a great number of intermediate scenarios which also give the correct density, and which would fill the space between the two extremes. It is evident from the figure that there exists a band of scenarios which are unchanged under a sign flip of C , which are found to be cases with $r \geq 1$. In these cases, we observe that the contribution from the dimension-five term dominates that of the Yukawa, leading to negligible change under the sign flip. For smaller values of r , the scalar mass m_S dictates the behaviour. A representative point $r = 0.1$ reveals that, for light S , the sign flip of C does not impact the cross section, but either sign of C improves the Yukawa-only cross section. For heavy S , we find instead that the positive C increases the cross section due only to the Yukawa, but $C < 0$ leads to destructive interference. We find also that, for each mass point, the maximal cross section is achieved with the maximal Wilson coefficient. The limiting values for the detection prospects are given in Tab. 5.1, indicating the mass of the scalar at which each exclusion limit intersects the distribution of scenarios obeying the correct relic density. Finally, in fig. 5.9, we investigate the viable scenarios with respect to the neutrino floor, which is the region of parameter space below which the irreducible background due to neutrinos makes direct detection almost impossible. In the figure we present six classes of benchmarks across the $C/\Lambda - \tilde{y}_t$ parameter space, indicating the regions corresponding to under- and over-abundance. A dark matter model is still viable if it leads to under-abundance, as the observed relic density may result from a number of contributions. However, if a scenario leads to over-abundance, the model can be ruled out. The solid black line indicates the correct relic density in a region accessible by detectors, and the dashed line indicates the correct relic density lying below the neutrino floor.

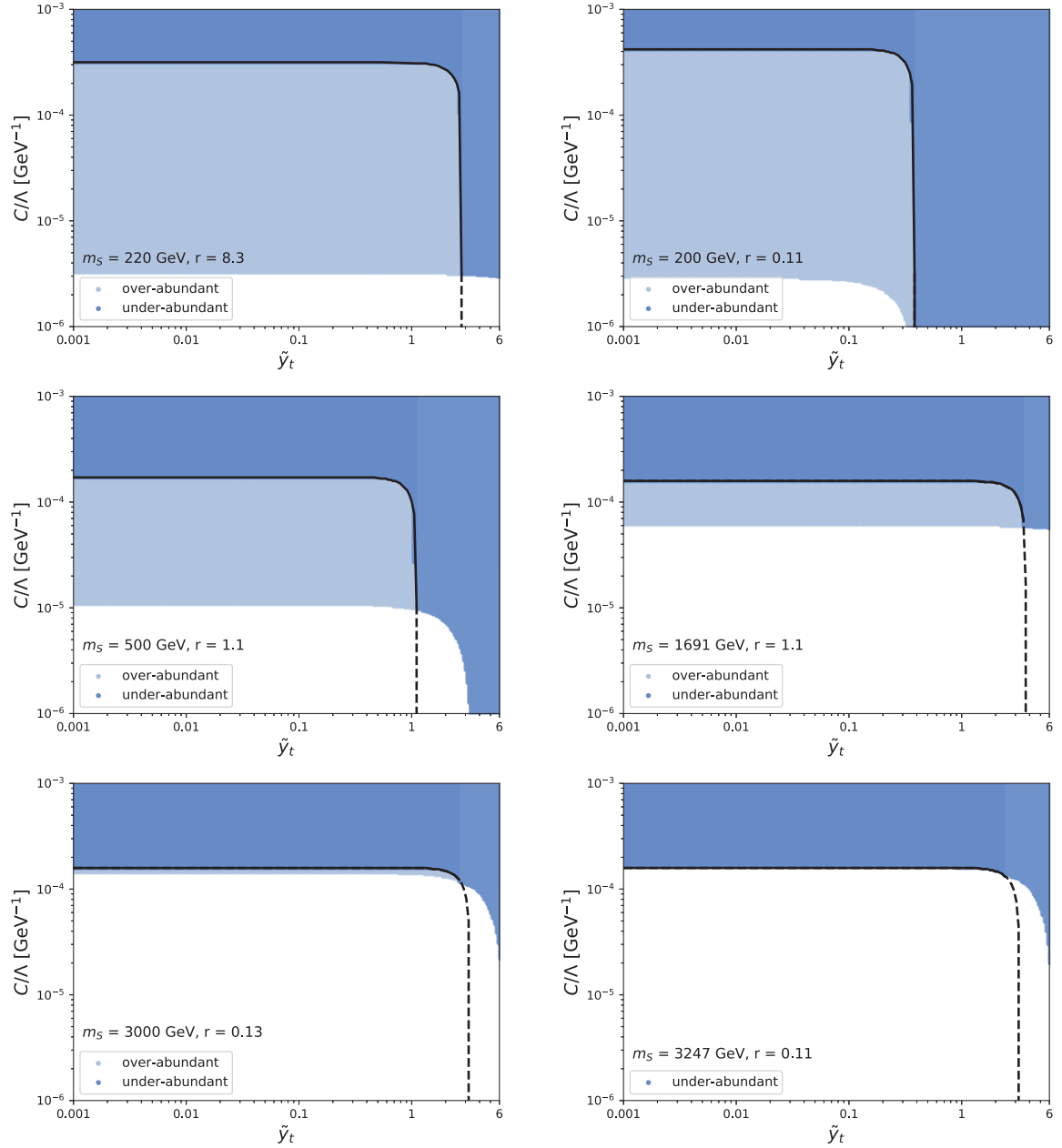


Fig. 5.9 Six benchmarks defined by m_S and m_T showing a variety of regimes, including both compressed and separated scenarios for light and heavy mass points. The blue area denotes the area in the $C/\Lambda - \tilde{y}_t$ plane which corresponds to a dark matter-proton cross section which is larger than the neutrino floor and therefore potentially experimentally reachable. While the shaded blue areas do not necessarily replicate the correct relic density, the relationship between the two parameters which does lead to the correct relic density $\Omega_{DM} h^2 = 0.1186 \pm 0.0020$ is plotted as a black line, where the solid line corresponds to parameter space lying above the neutrino floor, and the dashed line represents the parameter space hidden below the neutrino floor.

5.4 Indirect detection constraints

Indirect detection experiments of dark matter aim to measure the annihilation or decays of WIMPS via the SM particles produced during these processes [197]. We begin with an assessment of whether the indirect detection bounds may be expected to differ from those in previous works [150]. We again utilise FEYNRULES for the generation of UFO model files [114], this time using them as input into MADGRAPH5_AMC@NLO (MG5_AMC) [113] to simulate dark matter annihilation at close to 0 velocity. Following the simulation of production at colliders, we employ PYTHIA 8 [118] to describe parton showering and hadronisation. The results of the gamma spectra for the limiting cases are presented in the left plot of fig. 5.10, where a clear difference is seen due to the addition of the dimension-five term. We are therefore motivated to examine the indirect detection prospects. The same figure displays similar behaviour between the gamma spectra originating from $b\bar{b}$ and $t\bar{t}$ final states, indicating a rescaling of the Fermi-LAT [198] bounds, which are generated for the $b\bar{b}$ channel of dwarf spheroidal galaxy data in the 15 year limit, is reasonably written as

$$\sigma v_{t\bar{t}} = \sigma v_{b\bar{b}} \frac{N_{\gamma}^{b\bar{b}}}{N_{\gamma}^{t\bar{t}}}. \quad (5.32)$$

We focus on the $t\bar{t}$ final state, as annihilation into pairs of gluons is only relevant for $m_S < m_t$ [150], which we do not consider. In addition, previous results [150] also show that QCD emissions only play a role for higher dark matter masses; for very small r , NLO corrections are important above approximately $m_S = 2$ TeV, and for larger r differences between LO and NLO behaviour only appear for $m_S \geq 3$ TeV. Annihilations into $t\bar{t}$ systems can be constrained with proton anti-proton cosmic ray data. Given that the $t\bar{t}$ and $b\bar{b}$ spectra display the same behaviour as in fig. 5.10, we can employ Fermi-LAT constraints. The shape of the gamma ray spectrum is unlikely to be of help in our mass region, as $m_t < m_S < 5$ TeV are expected to be overwhelmed by the annihilation products hadronising before they are detected [150]. The plot on the right of fig. 5.10 displays the $\langle\sigma v\rangle$ at zero velocity, which is to be added to the full NLO result of Ref. [150]. The constraints resulting from the full cross section, including the NLO results, is given in the exclusion plots in fig. 5.13.

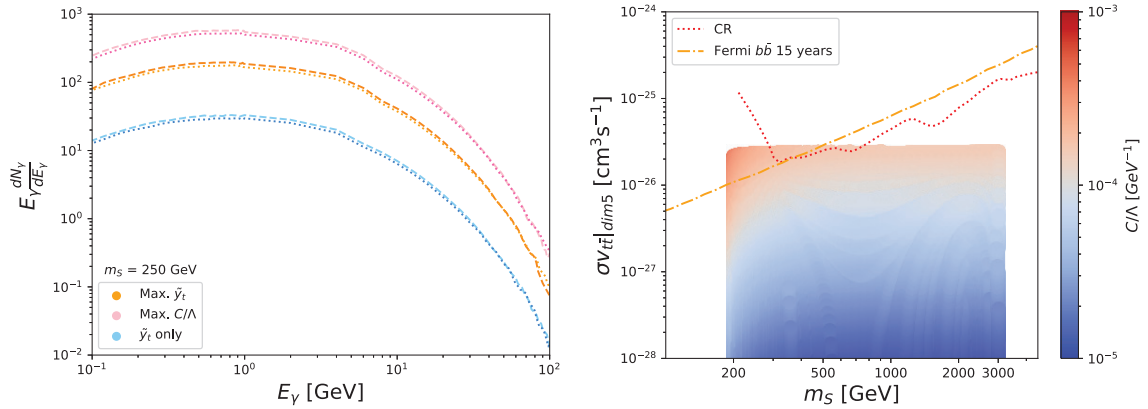


Fig. 5.10 *Left*: $SS \rightarrow t\bar{t}$ (dashed line) and $SS \rightarrow b\bar{b}$ (dotted line) photon spectra as obtained with PYTHIA for a benchmark $m_S = 250$ GeV. *Right*: All points correspond to the correct relic density, and show the NLO cross section for dark matter annihilation, including all possible Yukawa and C/Λ combinations.

5.5 Collider constraints

Finally, we investigate the possibility that the additional vertex due to the dimension-five operator may modify constraints at colliders. Experimental searches for dark matter form an important part of new physics searches at colliders such as the LHC, and there exist a number of previous physics searches which have been performed at colliders which may be reinterpreted to constrain the model examined here. The reinterpretation of previous analyses through recasting, described below, allows bounds to be estimated for a given model without a dedicated analysis at colliders. Generic searches for a fermionic mediator decaying to dark matter feature missing transverse energy in the final state, matching signatures from searches for SUSY. We will examine the production of a pair of top quarks with a pair of dark matter candidates in proton proton collisions, or the production of a pair of dark matter candidates with one or more jets,

$$pp \rightarrow t\bar{t}SS, \quad pp \rightarrow SSj(j).$$

The first channel is labelled $t\bar{t} + \cancel{E}_T$, and the channels featuring jets may be mono-jet or multi-jet plus missing transverse energy, after accounting for initial state radiation. In fig. 5.11, we present the diagrams relating to each of these processes, where the mono-jet/multi-jet processes are given by figs (1a) and (1b), and the $t\bar{t}$ processes by figs. (2a-2c).

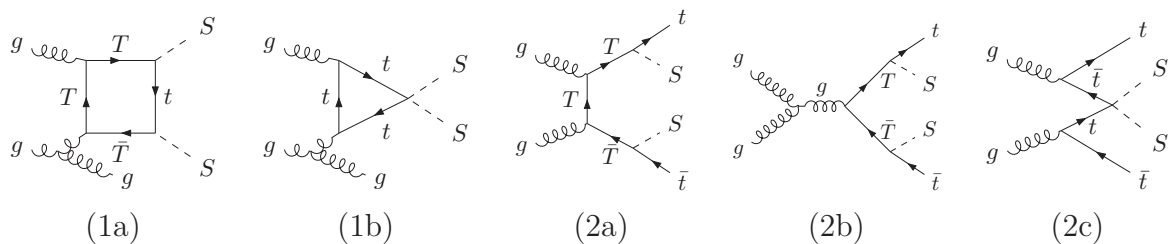


Fig. 5.11 Amplitudes contributing to the collider process with a SS (1a and 1b) or $t\bar{t}SS$ final state (2a - 2c), where the first, third and fourth diagrams are the pure NLO contributions, and the second and fifth diagrams arise due to the dimension-five operator and do not feature the heavy mediator.

Our model will feature behaviour produced by three phenomena which we factorise to handle separately; the pure NLO (QCD) component proportional to α_s , the pure EFT component proportional to C^2/Λ^2 , and the interference proportional to C/Λ . To that end, we investigate the scenario where the T width is small with respect to its mass, allowing the scattering amplitude to be factorised into production and decay. This approximation is valid in the case where the T pairs are produced via QCD processes, where the production cross section depends only on the mass of the T mediator, and where the number of decay modes for T are few [199]. This is a widely used approach, but other approaches have been explored using large width [199, 200]. In the narrow width case, the full $pp \rightarrow jSS$ and $pp \rightarrow t\bar{t}SS$ cross sections can thus be expanded as

$$\begin{aligned}\sigma_{jSS}(m_T, m_S) &= \tilde{y}_t^4 \hat{\sigma}_{jSS}^0(m_T, m_S) + \frac{C \tilde{y}_t^2}{\Lambda} \hat{\sigma}_{jSS}^{\text{int}}(m_T, m_S) + \frac{C^2}{\Lambda^2} \hat{\sigma}_{jSS}^{\text{dim5}}(m_S), \\ \sigma_{t\bar{t}SS}(m_T, m_S) &= \tilde{y}_t^4 \sigma_{t\bar{t}SS}^0(m_T, m_S) + \frac{C \tilde{y}_t^2}{\Lambda} \hat{\sigma}_{t\bar{t}SS}^{\text{int}}(m_T, m_S) + \frac{C^2}{\Lambda^2} \hat{\sigma}_{t\bar{t}SS}^{\text{dim5}}(m_S),\end{aligned}\quad (5.33)$$

where we neglect the higher order terms. The first terms in each expansion are the LO and NLO pieces, where the diagrams feature a T mediator as shown in the first three diagrams of fig. 5.11. The second piece of eq. (5.33) is dimension-five, representing the interference between “1” and C/Λ amplitudes. The third piece is the squared amplitude represented in the fourth diagram of fig. 5.11. The remaining pieces will be neglected. Concerning the validity of the effective operator at colliders, relevant scales in the phase space regime currently pursued by LHC searches are on the order of 1 TeV or less. Given $C \sim \mathcal{O}(1)$, we find a range of validity of 5 – 100 TeV for the relevant parameter space which yields the correct relic density, and are therefore satisfied that our predictions may be trusted in the range of validity of the EFT

theory when considering LHC Run-2 analyses. Application to future colliders of higher energy, such as the LHC 100 TeV run, should be treated with caution.

These events will result in collider signatures of a pair of top quarks produced in association with missing energy ($pp \rightarrow t\bar{t} + \cancel{E}_T$), and can be probed using existing dark matter searches featuring mono-X probes, focusing on the monojet searches, as well as with multi-jet analyses. This can be achieved through ‘recasting’ [120] analyses, where an existing analysis may be re-used to investigate an alternative signal hypothesis. Using the observed yield in data recorded in the original analysis along with the expected background, and in combination with the expected yield for the new signal background, it is possible to determine whether the signal has already been excluded. When making a measurement, the CL_s method of presenting the result, introduced in section 3.3.3 and expanded upon in the following section, is complementary to the traditional frequentist confidence interval, and has here been used to evaluate the relevant exclusion limits. We will now proceed to outline the recasting of ATLAS and CMS analyses from the LHC in order to analyse the visibility of our signal at colliders. To begin, we present an overview of the techniques of use.

5.5.1 Recasting an analysis and the CL_s technique

The recasting of an experimental physics analysis exploits the sensitivity of existing searches to a broader class of models. While experiments are designed to identify certain physics events or occurrences, testing predictions at the energy frontiers of colliders, they can often be extended through a process called *recasting* [201]. Through recasting an analysis, an existing analysis may be re-used to investigate an alternative signal hypothesis. Through recasting one may assess whether a given signal has already been excluded by a previous analysis.

In order to recast an analysis, one only needs the expected signal yield for the new model. It is not necessary to have access to the original data, and new event selection criteria do not need to be designed. Additionally, background estimates and systematic uncertainties can be reused from the original analysis. In order to estimate the new expected signal yield, one simulates data, hadronisation, detector effects and reconstruction. In testing the new theory one then uses the observed yield in data from the original analysis, the expected yield from the new signal process, and the expected yield from background processes, and also includes the uncertainties [201]. After the recasting, areas of the parameter space which are excluded by the original search have an associated high efficiency, and areas which are not covered have a low efficiency. That is, the efficiency of the original search in different signal scenarios is

evaluated. An analysis may then be tuned to target the not-yet-excluded portions of parameter space [201].

In a typical experimental analysis, the data undergoes a series of *cuts* which are intended to select only the most ‘interesting’ events, as discussed in chapter 3. These cuts are designed to identify specific physics events, and are crucial in reducing the amount of data to a level that may be feasibly recorded [202]. The data undergoes both trigger-level cuts, at the time of recording, and offline cuts. The latter are imposed on all data which passes the former. The events failing the former are not recorded and cannot be recovered. It is through the definition of cuts that sample regions are identified, and analyses are implemented in MADANALYSIS 5, as in this work.

The CL_s technique is then used in presenting results from a frequentist statistics perspective [203]. The technique is used for determining exclusion intervals through setting limits. Particle physicists may be attracted to frequentist statistics, rather than Bayesian approaches, so as not to be biased by subjectivity. Bayesian credible intervals converge with frequentist confidence intervals in the case of large statistics. However, frequentist confidence intervals may be misleading in the case of low statistics, as is often the case with experimental searches subject to rare signals and large backgrounds [203].

When making a measurement, the CL_s method of presenting the result is complementary to the traditional frequentist confidence interval. In this alternative approach, the CL_s is instead defined as ‘the ratio of confidences in the signal+background to background hypothesis’ [204]. The CL_s method allows for the strongest possible exclusion on a given measurement, or confirming the existence of a signal as strongly as possible, while maintaining reasonable false positive and false negative rates [204].

5.6 Reinterpreted LHC analysis results

We now move to the implementation of the LHC recasting. For the monojet search, we study the ATLAS 13 TeV monojet-like search

ATLAS_EXOT_2016_27 [205, 206], featuring an energetic jet and large missing momentum, and covering 36.2 fb^{-1} . In the case of multijet searches, we consider the ATLAS_CONF_2019_040 [207, 208] analysis covering 139 fb^{-1} and featuring at least two hard jets in association with missing momentum. Both searches are held in the MADANALYSIS5 public analysis database (PAD) [209], and were implemented using

the MADANALYSIS5 recasting framework [119, 120], employing MADGRAPH5_AMC@NLO (MG5_AMC) [113] in conjunction with PYTHIA 8 [118] to describe parton showering and hadronisation. To extract the CL_s , defined as the ratio of confidences in the signal+background to background hypothesis [204], we run 100,000 toy experiments generating a Poisson distribution for the number of background events b , with mean and width respectively the expected number of background events in the analysis and the associated uncertainty. We then evaluate the p -values of the signal + background and background only scenarios, finally deriving the associated CL_s values for each signal region within a given analysis. In the case of both the dimension-five cross section and the NLO cross section, the mono-jet jSS cross section is negligible once the p_T requirements of the mono-jet searches are imposed, leaving us to consider only the recasting of the multi-jet. We find that the values of C/Λ which result in the correct relic density lead to a significant suppression of the dimension-five contributions to the collider cross section. This suppression of the contributions due to the contact term applies also to the $t\bar{t}$ searches, which were not included in the recasting. In the analysis of Ref. [150], the authors utilised the CMS-SUS-17-001 analysis [210], a search for direct stop pair production at $\sqrt{s} = 13$ TeV, and featuring 35.9 fb^{-1} of data. The analysis required two opposite sign isolated leptons, two hard jets, and well separated missing transverse energy. This analysis has recently been updated [211] to 137 fb^{-1} of data, but does not yet feature in the MADANALYSIS5 PAD database. However, a comparison of the observed limits in both cases reveals that a significant deviation is not observed when updating to the larger luminosity. We therefore follow the procedure outlined in Ref. [212] in recalculating the CL_s for the full Run 2 dataset by extrapolating the background and its uncertainty, where the background relative uncertainty is taken as constant across the extrapolations. Using a recasting of the CMS-SUS-17-001 for this signal, the extrapolation procedure is performed by rescaling the number of background events n_b as

$$n_b^{new} = n_b \frac{\mathcal{L}_{new}}{\mathcal{L}_0}, \quad (5.34)$$

where the original luminosity \mathcal{L}_0 and desired luminosity \mathcal{L}_{new} are 35.9 fb^{-1} and 139 fb^{-1} respectively. We assume the new number of background events to be equal to the number of observed events, n_{obs}^{new} , which also features in the CL_s calculation. The associated uncertainties are rescaled in a similar fashion. As a result, the shaded region in blue shown in the collider exclusion plot of fig. 5.12 depicts the 95 % confidence

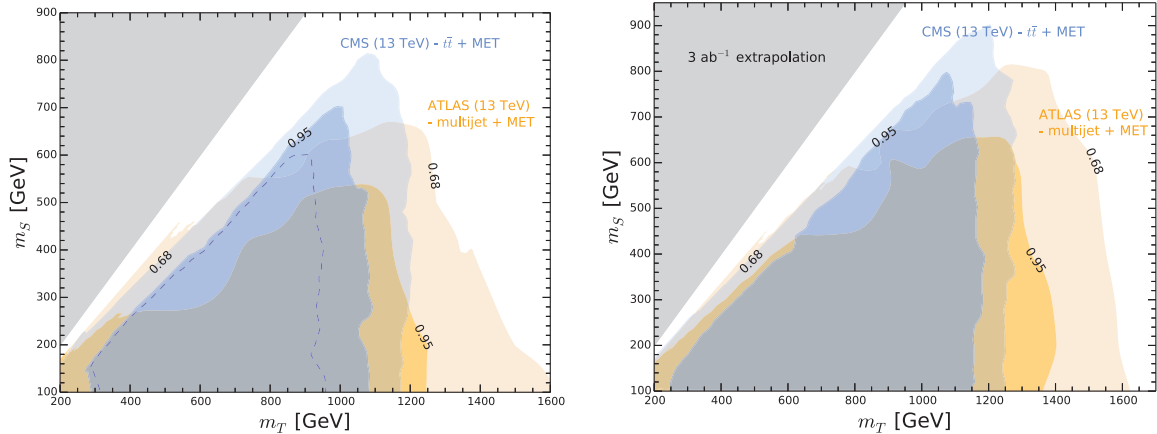


Fig. 5.12 Collider constraints calculated for the $t\bar{t} + \cancel{E}_T$ channel for both the multi-jet and $t\bar{t}$ searches, indicating the 95 % CL (darker regions) and 68 % CL (lighter regions) exclusion contours. We have indicated the LHC run-2 exclusions with a luminosity of 139 fb^{-1} in the left figure, including the dashed line indicating the exclusion obtained from the CMS-SUS-17-001 analysis featuring 35.9 fb^{-1} of data, and the extrapolation of the bounds to 3 ab^{-1} on the right.

limit for the full Run 2 $t\bar{t} + \cancel{E}_T$ CMS search, where the original analysis at \mathcal{L}_0 is indicated by the dashed blue line. Finally, an extrapolation to 3 ab^{-1} is presented, using the above technique to rescale both the multi-jet and $t\bar{t} + \cancel{E}_T$ analyses. While the ATLAS_CONF_2019_040 analysis can be used to exclude a range of mediator and dark matter masses, the constraints are not modified by the inclusion of dimension-five effects in a statistically significant manner. For this reason we simply update the bounds in Ref. [150] for the multi-jet plus \cancel{E}_T analysis for the pure QCD effects. The bounds on this model that may be extracted from recasting the ATLAS_CONF_2019_040 are summarised in blue in fig. 5.12, where the darker blue region is excluded at the 95% CL by at least one signal region of the considered analysis, and the lighter blue region shows the 1σ limit. Similarly, the extrapolated exclusions for CMS-SUS-17-001 are given in darker and lighter orange. We include bounds for the full LHC Run-2 (left), and an extrapolation to 3 ab^{-1} (right). It is clear that lighter masses of the mediator T are excluded, and combinations of light S with mediator masses up to roughly 1 TeV are also excluded or strongly constrained. Finally, we present in fig. 5.13 a combined exclusion plot displaying the constraints obtained through both the astrophysical and collider constraints. The results show that the vast majority of the parameter space of this model is testable at current or future experiments. Indeed, the yellow shaded region of the plot shows the reach of the model above the neutrino floor, indicating that the model is clearly testable at

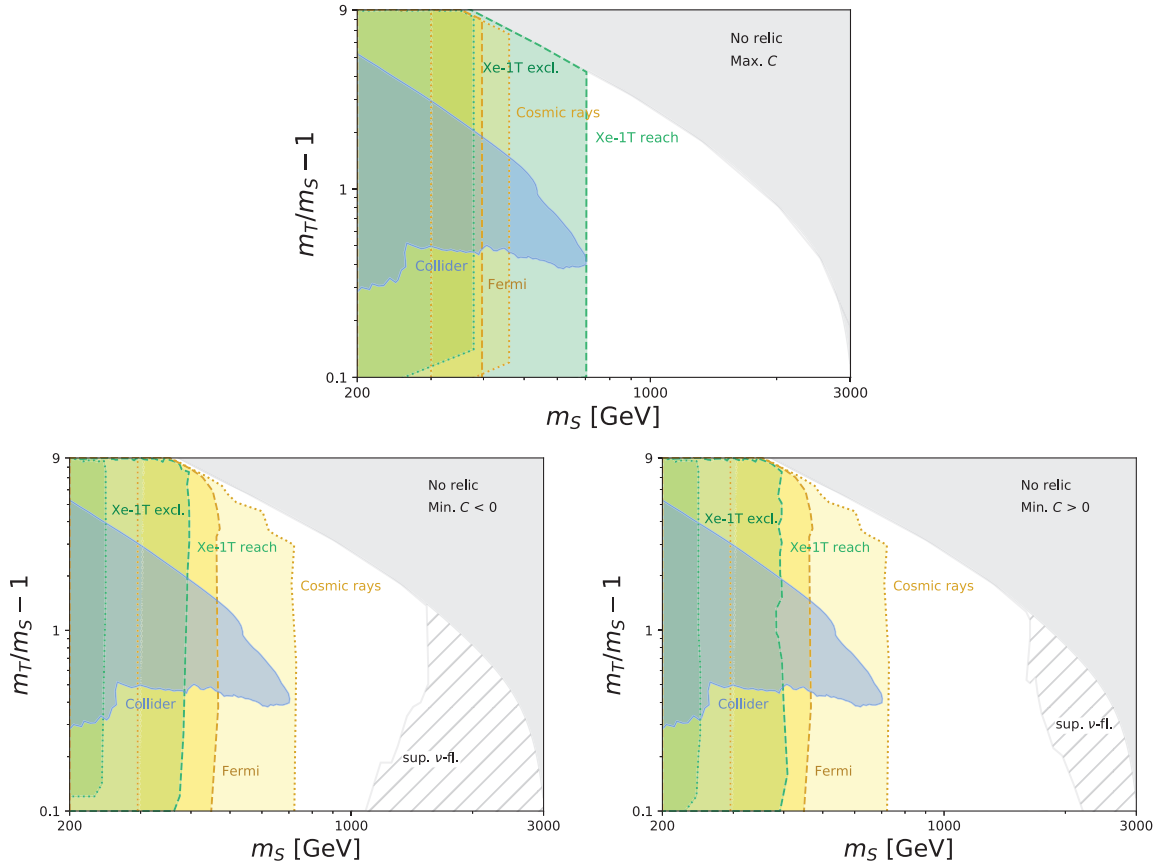


Fig. 5.13 Exclusion plots featuring all experimental constraints for maximum c (top), minimum $c < 0$ (bottom left) and minimum $c > 0$ (bottom right). The grey shaded region features disallowed relic densities. The green shaded regions correspond to the direct detection constraints, the darker blue to the collider constraints, and the yellows to the indirect detection constraints. It should be noted that ‘minimum’ c again corresponds to the maximal possible c value which makes no modification to the relic density calculated by the Yukawa coefficient.

future direct detection experiments. The indirect constraints are more stringent for the minimum values of C than for the maximum values, which is an interesting result. In the large C limit, the additional cross section generated by the Yukawa term is minimal, with $\sigma_{d5}/\sigma_{\tilde{y}} \approx 10^{10}$. The addition of the Yukawa term then does not add to the C -generated cross section for indirect detection. This result is independent of m_T , as per eq. (5.9). In the opposing limit, the difference is much smaller, with $\sigma_{d5}/\sigma_{\tilde{y}} \approx 10$. Thus the cross section generated by small C adds to the large- \tilde{y}_t cross section.

5.7 A top partner

To further support the possibility of the heavy dark matter being embedded in a composite Higgs scenario, we consider the inclusion of an additional heavy resonance, T' , in the effective model. We describe T' as being a top partner, a standard inclusion within a generic composite Higgs model to facilitate the mechanism of partial compositeness. As any composite Higgs model in the same family as those considered in previous chapters may be expected to feature a heavy top partner, the study of the impact of such a resonance on the phenomenology in this chapter is relevant. While a composite Higgs model may feature a number of heavy vector-like quarks, here we will consider the inclusion of a single top partner embedded in the general representation of $SU(2)_L$, coupling to all SM quarks. We follow the path of Ref. [77], which proposes a minimal Lagrangian describing all allowed couplings of the VLQs for a model-independent search strategy.

The VLQ T' , which is considered to arise as a composite resonance in the same manner as S and T , has electromagnetic charge $Q = 2/3$ and can mix and decay directly into SM quarks as in Ref. [77]. In contrast to the vector-like mediator T , under the imposed \mathbb{Z}_2 symmetry this VLQ is required to be even in order to facilitate partial compositeness, whereby the top partner mixes with the top quark. One should consider whether it is realistic to demand that T and T' have opposite \mathbb{Z}_2 charge, but we postulate that it is reasonable for the two VLQs to live in separate multiplets and to have opposite parity. T' is a colour triplet, lives in a general (complete) representation of weak $SU(2)_L$, and has (chiral) couplings to all SM quarks via Yukawa mixing. The top partners can live in multiplets of $SU(2)$ [77], including singlets, doublets or triplets. In the context of composite Higgs models, masses for the top partner may be expected to lie in the range 500 – 1500 GeV, which we will consider here. The Lagrangian to be added to the model includes the interactions of the top partner with SM particles in a renormalisable form [213], and where additional operators dictating the interactions of the top partner with the \mathbb{Z}_2 -odd BSM states are given in the final terms

$$\begin{aligned}
\mathcal{L}_{T'} = & \bar{T}'(i\not{D} - m_{T'})T' - h \left[\bar{T}' \left(\hat{\kappa}_L^{T'} P_L + \hat{\kappa}_R^{T'} P_R \right) q_u + \text{h.c.} \right] \\
& + \frac{g}{2c_W} \left[\bar{T}' \not{Z} \left(\tilde{\kappa}_L^{T'} P_L + \tilde{\kappa}_R^{T'} P_R \right) q_u + \text{h.c.} \right] \\
& + \frac{\sqrt{2}g}{2} \left[\bar{T}' \not{W} \left(\kappa_L^{T'} P_L + \kappa_R^{T'} P_R \right) q_d + \text{h.c.} \right] + \tilde{y}_{T'} S \bar{T}' T + \text{h.c.} + \frac{C'}{\Lambda} S S \bar{T}' T',
\end{aligned} \tag{5.35}$$

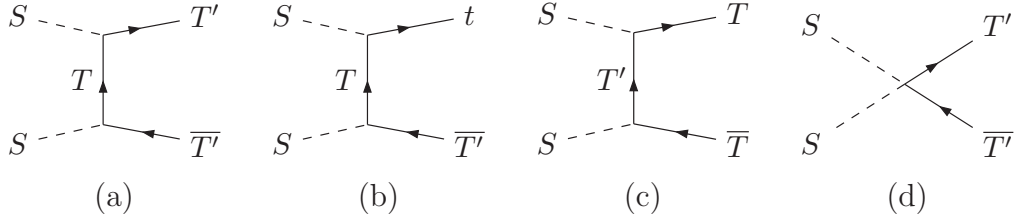


Fig. 5.14 Amplitudes contributing to the relic density calculation for S which arise due to the addition of the top partner T' . Diagrams (a) and (b) originate from the new Yukawa-type interaction, while diagram (d) arises due to the additional dimension-five term. Diagram (c) is possible, but given that $m_T > m_S$ it will not contribute to the S annihilation cross section in a non-negligible way.

where couplings to the gluon and photon are standard. All couplings are dictated by gauge invariance, depending on the representation of the VLQ [77]. Here, an additional Yukawa term and dimension-five term are introduced. These new vertices may be expected to impact the relic density of S through additional annihilations to $T\bar{T}'$ or $t\bar{T}'$ pairs, and is not expected to impact the $t\bar{t}$ process. The new Feynman diagrams relevant to the model are shown in fig. 5.14.

If T' is heavier than S and T , we may expect minimal impact on the direct and indirect detection constraints. However, it is possible that there may have been an impact in the early universe, and the relic density modification should therefore be checked. As with S and T , we require that the mass of the top partner is always within an order of magnitude of both S and T , to further support the idea that they are all scalar resonances. In this vein, we perform a new scan including the additional operators in eq. (5.35), where the Yukawa and dimension-five couplings vary across the same parameter space as their counterparts in the previous sections.

The interplay between the Yukawa-type terms is shown in fig. 5.15. In this figure, where all points correspond to the correct relic density, the masses of S , T , and T' are allowed to vary across the parameter space. The two-dimensional histogram features a colour gradient corresponding to the dark matter mass, and corresponds to the unique case where the dimension-five term has been turned off ($C = 0$). This scenario allows for the direct comparison of the interplay between Yukawa-type terms. Additionally, the light blue shaded region denotes the area which is filled in the event that the dimension-five term is switched back on; in this scenario, the Yukawa-type terms are allowed to become very small, as in the previous section. The gap evident on the $\tilde{y}_{T'}$ -axis is a physical feature which emerges due to kinematic effects in the decay channels, and is governed by the $r' = m_{T'}/m_S - 1$ parameter; for r' positive larger

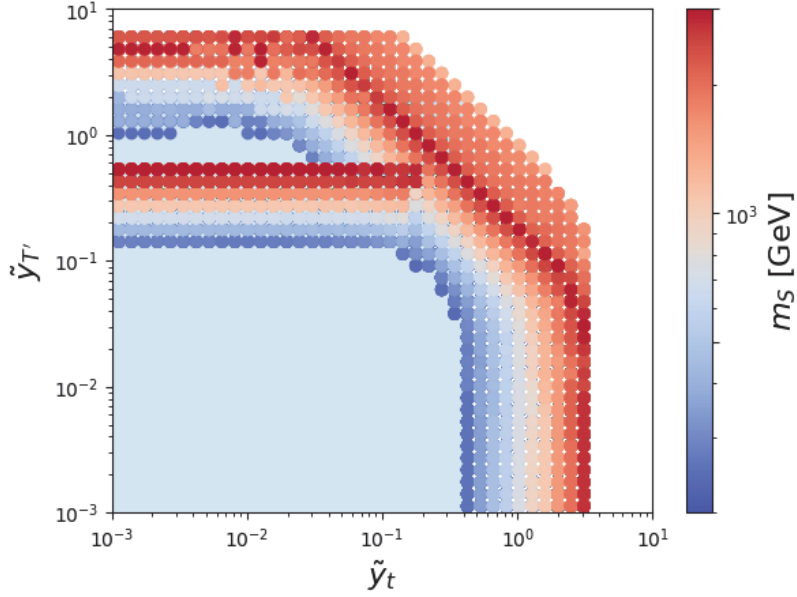


Fig. 5.15 Interplay of Yukawa-type terms for a range of S , T and T' masses. All points show the correct relic density.

values of $\tilde{y}_{T'}$ are observed, and for r' negative we find smaller values of $\tilde{y}_{T'}$ are observed. The gap therefore appears due to a change in behaviour when T' becomes heavier than the dark matter candidate. Additional kinematic effects govern the diagonal ridge visible in the plot.

5.7.1 Experimental discussion

As in the previous section, where the top partner was not included, a dark matter model of this nature is potentially reachable through both astrophysical and collider experiments. In considering the potential outcomes at each, the relative masses of the resonances define whether we may expect the bounds to change. From the Feynman diagrams in fig. 5.14 it is clear that the top partner T' will contribute to the SS annihilation only when $2m_S \geq m_{T'} + m_t$, where $m_{T'}$ is always greater than m_t .

Indeed, on assessing the relic density calculations in the orthogonal region, we find no change to the scan of the previous section where the top partner was not present.

In considering the potential constraints arising due to colliders, we first reiterate the bounds imposed in section 5.6. There we showed that the maximum bounds on m_T are roughly 1.25 TeV with $m_S \sim 100$ GeV, 1.15 TeV with $m_S \sim 500$ GeV, and lowering to roughly 1.0 TeV with $m_S \sim 700$ GeV. Additionally, current experimental bounds on top partners, without additional decays to the TS final state, are roughly 1.3 TeV.

m_T	m_S	Bounds modified for
$m_T \sim 1.0$ TeV	$500 < m_S < 700$ GeV	1.5 TeV $< m_{T'} < 1.7$ TeV
$m_T \sim 1.15$ TeV	200 GeV $< m_S < 500$ GeV	$1.35 < m_{T'} < 1.65$ TeV
$m_T \sim 1.25$ TeV	$m_S \sim 100$ GeV	$m_{T'} > 1.35$ TeV

Table 5.2 Modification of the bounds in the relevant mass cases.

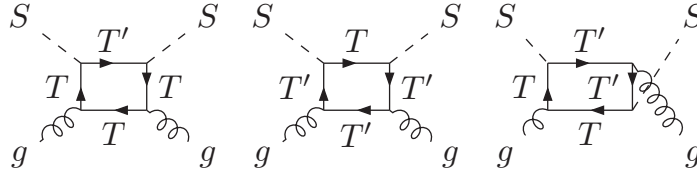


Fig. 5.16 Additional diagrams which contribute to the direct detection due to the new vertex.

We present the masses of the mediator and dark matter candidate which would weaken bounds for a top partner in three separate scenarios in table 5.2. Considering first the case where $m_T > m_{T'}$, the bounds on m_T could be weakened in the case where $m_T > 1.3$ TeV + m_S . In the alternative case, where $m_{T'} > m_T$, bounds on the top partner would be modified as outlined in table. 5.2. However, in each case outlined, there are no bounds to be relaxed as current bounds on the top partner VLQ sit at roughly 1.3 TeV, and the additional decays of $T \rightarrow T'S$ or $T' \rightarrow TS$ would not be expected to shift the current bounds at colliders. Investigating this model would therefore rely fully on astrophysical constraints.

Considering implications on direct detection experiments, we identify several new Feynman diagrams which would contribute to the effective interaction of the dark matter candidates with a SM nucleus, illustrated in fig. 5.16. These diagrams mirror those presented in section 5.3, where the top quark t has here been replaced by the top partner T' . We are therefore able to employ the techniques of Ref. [191] in order to obtain the interaction cross section, where we will be able to include or exclude the additional term generated by the dimension-five coupling as we wish. Notably, while the results of section 5.3 employed the approximation that $m_t < m_S, m_T$, we do not have that same behaviour in this case, and will apply the full model without an approximation. We expect also that the top partner T' will modify the SS annihilation with respect to the previous work only when $2m_S \geq m_{T'} + m_t$.

5.8 Conclusion

In this work we have investigated the significant modifications that arise in a theory featuring a heavy top-philic dark matter candidate through the inclusion of a dimension-five term. In an attempt to motivate situating such a heavy scalar within a composite Higgs model as a scalar resonance, we have investigated the higher dimensional interaction term, which may be expected to arise within a generic composite Higgs model. In doing so, we find that the phenomenology of such a state is significantly modified with respect to the contributions arising from the NLO cross section.

By including a heavy mediator roughly mass-degenerate with the dark matter candidate, we have investigated the parameter space which yields the correct relic density using an analytical formulation. We have demonstrated that the area where coannihilations occur should be treated separately and with care. When investigating the direct detection constraints, it has been shown that many possible models within the allowed parameter space lie above the neutrino floor, and are therefore within testable limits at experiments. In the case of indirect detection, the addition of the dimension-five operator pushes the model across current and expected bounds up to $m_S \sim 700$ GeV for some parameter choices. In the collider simulation, we found no significant improvement due to the dimension-five effects. These results serve to underline the importance of the complementarity of collider and astrophysical constraints, as the dark matter models saw modifications in constraints due to their relic densities but not at colliders.

As an extension to this study, we investigated the addition of an additional heavy \mathbb{Z}_2 even state which could play the role of top partner in a composite Higgs model. We discussed additional interactions which feature in the extension, and investigated the interplay between the new Yukawa-type term which is introduced as a result. We also discussed potential experimental constraints for the extension, motivating that a collider scan is not likely to yield a modification to existing bounds, and that direct and indirect detection will need to be relied upon.

Chapter 6

Concluding remarks

The current status of particle physics is a combination of experimental triumphs and theoretical unknowns, which have resulted in a varied field of BSM theories with no clear theoretical guidance on how the SM should be extended. While focusing on extensions to the scalar sector, in this thesis we have tried to reflect that a wide range of theories are currently in contention. The relative paucity of clues found thus far at colliders and other experiments is not an indication that the problems have disappeared, but perhaps of a gap in our understanding. Given the wide parameter spaces in each model discussed in this thesis alone, it is also conceivable that the solution is simply very well hidden.

The range of extensions to the scalar sector which have been covered in this thesis have been focused on theories of compositeness, where the Higgs boson is re-imagined as a bound state of fundamental fermions. This not only provides a solution to the hierarchy problem in forcing the Higgs mass to lie well below the Planck scale, but also leads to the introduction of a number of other mass resonances which emerge as additional bound states of fermions. Two ubiquitous players in any composite Higgs model of this nature are the pseudo-scalar a , emerging as a consequence of the $U(1)$ symmetry of the theory, and the pNGB η , which appears alongside the Higgs boson when the global symmetry of the hyperfermions is broken. The first of these is discussed in chapter 3, where we have outlined a search for such a light particle at future high-luminosity lepton colliders. The search and relevant parameter space is complementary to current bounds and channels, including both di-photon and di-tau searches. Given that compositeness may be first confirmed not through Higgs-related measurements but rather through measurements of other composite resonances, we motivated searches for such states at future colliders, which will be well-placed to search for light and weakly interacting states. Also in chapter 3, we explored the use

of machine learning techniques to improve on cut-and-count results. We motivated BDTs as a strong contender in this area, where we showed they can be used to separate hard-to-reach signal from background.

The second ever present feature of a composite Higgs model is the pNGB η , discussed in chapter 4. There we outlined how a composite Higgs model is built using as an example the $SU(4)/Sp(4)$ group structure, and investigated potential phenomenology for the η . Given the existence of stringent EWPT results, we investigated the heavier η case, with its mass lying above 500 GeV. We focused mainly on fermiophobic scenarios, which lead to interesting signals but suffer from very small production numbers which make a search in this set-up difficult.

In both chapters 3 and 4, we introduced the missing mass variable, and showed that it has significant potential in separating signal from background. We investigated a range of future lepton colliders, which feature a number of centre of mass energies, luminosities, and polarisations. These colliders, none of which are yet built, are all in contention to be the project which will take over from the LHC. Where the resonances considered are expected to be light, the large luminosities promised by the FCC project may be advantageous, as motivated in chapter 3. Searches for heavier resonances will need to rely on colliders with higher centre of mass energies, such as the CLIC collider discussed in chapter 4.

We then extended our compositeness theory to encompass heavy dark matter. In chapter 5, we investigated the inclusion of a WIMP candidate in the theory accompanied by a heavy mediator. Unlike the usual method of including dark matter in a composite Higgs model as a pNGB, we postulated instead that the candidate emerges as a scalar resonance of the fundamental fermions. Much like QCD, where light pions exist far below the confinement scale and heavier resonances lie near to it, here the heavy dark matter and mediator are massive and may be up to 3 TeV. We began by including a generic dimension-five term to an existing model, as these contact terms may be expected to contribute in strongly interacting theories. To build on this effective model, we have introduced a generic heavy top partner, a VLQ which couples linearly to the top quark and is a sign of partial compositeness. We discussed the additional interactions which may arise, and motivated why one would not expect modifications to collider constraints due to this new resonance. Instead, further investigations should focus on astrophysical experiments to derive further bounds.

Perhaps one turtle stands at the bottom of them all, or perhaps it really is “turtles all the way down”. To know that, we will need to continue moving towards higher

energies to investigate the upper limits of the SM. This thesis has introduced a number of effective models which demonstrate the reach of compositeness theories. In it we have motivated the extension of the scalar sector as the place where the answers to some of the foremost questions in particle physics may be found.

References

- [1] Serguei Chatrchyan et al. Observation of a new boson at a mass of 125 GeV with the CMS experiment at the LHC. *Phys. Lett.*, B716:30–61, 2012. doi:[10.1016/j.physletb.2012.08.021](https://doi.org/10.1016/j.physletb.2012.08.021).
- [2] Georges Aad et al. Observation of a new particle in the search for the Standard Model Higgs boson with the ATLAS detector at the LHC. *Phys. Lett.*, B716: 1–29, 2012. doi:[10.1016/j.physletb.2012.08.020](https://doi.org/10.1016/j.physletb.2012.08.020).
- [3] Steven Weinberg. Implications of Dynamical Symmetry Breaking. *Phys. Rev.*, D13:974–996, 1976. doi:[10.1103/PhysRevD.13.974](https://doi.org/10.1103/PhysRevD.13.974).
- [4] Steven Weinberg. A model of leptons. *Phys. Rev. Lett.*, 19:1264–1266, Nov 1967. doi:[10.1103/PhysRevLett.19.1264](https://doi.org/10.1103/PhysRevLett.19.1264).
- [5] Abdus Salam. Weak and Electromagnetic Interactions. *Conf. Proc.*, C680519: 367–377, 1968.
- [6] Sheldon L. Glashow. Partial-symmetries of weak interactions. *Nuclear Physics*, 22(4):579 – 588, 1961. ISSN 0029-5582. doi:[http://dx.doi.org/10.1016/0029-5582\(61\)90469-2](http://dx.doi.org/10.1016/0029-5582(61)90469-2).
- [7] B. Abi et al. Measurement of the Positive Muon Anomalous Magnetic Moment to 0.46 ppm. *Phys. Rev. Lett.*, 126(14):141801, 2021. doi:[10.1103/PhysRevLett.126.141801](https://doi.org/10.1103/PhysRevLett.126.141801).
- [8] G. W. Bennett et al. Final Report of the Muon E821 Anomalous Magnetic Moment Measurement at BNL. *Phys. Rev. D*, 73:072003, 2006. doi:[10.1103/PhysRevD.73.072003](https://doi.org/10.1103/PhysRevD.73.072003).
- [9] R. Aaij et al. Test of lepton universality with $B^0 \rightarrow K^{*0} \ell^+ \ell^-$ decays. *JHEP*, 08: 055, 2017. doi:[10.1007/JHEP08\(2017\)055](https://doi.org/10.1007/JHEP08(2017)055).
- [10] Roel Aaij et al. Test of lepton universality using $B^+ \rightarrow K^+ \ell^+ \ell^-$ decays. *Phys. Rev. Lett.*, 113:151601, 2014. doi:[10.1103/PhysRevLett.113.151601](https://doi.org/10.1103/PhysRevLett.113.151601).
- [11] Roel Aaij et al. Angular analysis and differential branching fraction of the decay $B_s^0 \rightarrow \phi \mu^+ \mu^-$. *JHEP*, 09:179, 2015. doi:[10.1007/JHEP09\(2015\)179](https://doi.org/10.1007/JHEP09(2015)179).
- [12] Roel Aaij et al. Differential branching fraction and angular analysis of $\Lambda_b^0 \rightarrow \Lambda \mu^+ \mu^-$ decays. *JHEP*, 06:115, 2015. doi:[10.1007/JHEP06\(2015\)115](https://doi.org/10.1007/JHEP06(2015)115). [Erratum: *JHEP* 09, 145 (2018)].

- [13] Albert M Sirunyan et al. Measurement of angular parameters from the decay $B^0 \rightarrow K^{*0} \mu^+ \mu^-$ in proton-proton collisions at $\sqrt{s} = 8$ TeV. *Phys. Lett. B*, 781: 517–541, 2018. doi:[10.1016/j.physletb.2018.04.030](https://doi.org/10.1016/j.physletb.2018.04.030).
- [14] Morad Aaboud et al. Angular analysis of $B_d^0 \rightarrow K^{*0} \mu^+ \mu^-$ decays in pp collisions at $\sqrt{s} = 8$ TeV with the ATLAS detector. *JHEP*, 10:047, 2018. doi:[10.1007/JHEP10\(2018\)047](https://doi.org/10.1007/JHEP10(2018)047).
- [15] A. Abdesselam et al. Angular analysis of $B^0 \rightarrow K^{*0} \ell^+ \ell^-$. In *LHC Ski 2016: A First Discussion of 13 TeV Results*, 4 2016.
- [16] Roel Aaij et al. Angular analysis of the $B^0 \rightarrow K^{*0} \mu^+ \mu^-$ decay using 3 fb⁻¹ of integrated luminosity. *JHEP*, 02:104, 2016. doi:[10.1007/JHEP02\(2016\)104](https://doi.org/10.1007/JHEP02(2016)104).
- [17] R Aaij et al. Measurement of Form-Factor-Independent Observables in the Decay $B^0 \rightarrow K^{*0} \mu^+ \mu^-$. *Phys. Rev. Lett.*, 111:191801, 2013. doi:[10.1103/PhysRevLett.111.191801](https://doi.org/10.1103/PhysRevLett.111.191801).
- [18] Y. Amhis et al. Averages of b -hadron, c -hadron, and τ -lepton properties as of summer 2016. *Eur. Phys. J. C*, 77(12):895, 2017. doi:[10.1140/epjc/s10052-017-5058-4](https://doi.org/10.1140/epjc/s10052-017-5058-4).
- [19] Peter W. Higgs. Broken symmetries and the masses of gauge bosons. *Phys. Rev. Lett.*, 13:508–509, Oct 1964. doi:[10.1103/PhysRevLett.13.508](https://doi.org/10.1103/PhysRevLett.13.508).
- [20] F. Englert and R. Brout. Broken symmetry and the mass of gauge vector mesons. *Phys. Rev. Lett.*, 13:321–323, Aug 1964. doi:[10.1103/PhysRevLett.13.321](https://doi.org/10.1103/PhysRevLett.13.321).
- [21] R. Brout and F. Englert. Spontaneous symmetry breaking in gauge theories: A Historical survey. In *1997 Europhysics Conference on High Energy Physics*, pages 3–10, 2 1998.
- [22] P. W. Anderson. Plasmons, gauge invariance, and mass. *Phys. Rev.*, 130: 439–442, Apr 1963. doi:[10.1103/PhysRev.130.439](https://doi.org/10.1103/PhysRev.130.439).
- [23] Jeffrey Goldstone, Abdus Salam, and Steven Weinberg. Broken symmetries. *Phys. Rev.*, 127:965–970, Aug 1962. doi:[10.1103/PhysRev.127.965](https://doi.org/10.1103/PhysRev.127.965).
- [24] J. Goldstone. Field Theories with Superconductor Solutions. *Nuovo Cim.*, 19: 154–164, 1961. doi:[10.1007/BF02812722](https://doi.org/10.1007/BF02812722).
- [25] Chuene Mosomane, Mukesh Kumar, Alan S. Cornell, and Bruce Mellado. Exploring cp-even scalars of a two higgs-doublet model in future e⁻ p colliders. *Journal of Physics: Conference Series*, 889(1):012004, 2017.
- [26] John Ellis. Higgs Physics. In *2013 European School of High-Energy Physics*, 12 2013. doi:[10.5170/CERN-2015-004.117](https://doi.org/10.5170/CERN-2015-004.117).
- [27] Sally Dawson, Christoph Englert, and Tilman Plehn. Higgs Physics: It ain’t over till it’s over. *Phys. Rept.*, 816:1–85, 2019. doi:[10.1016/j.physrep.2019.05.001](https://doi.org/10.1016/j.physrep.2019.05.001).

- [28] Csaba Csaki, Christophe Grojean, and John Terning. Alternatives to an Elementary Higgs. *Rev. Mod. Phys.*, 88(4):045001, 2016. doi:[10.1103/RevModPhys.88.045001](https://doi.org/10.1103/RevModPhys.88.045001).
- [29] Gabriele Ferretti and Denis Karateev. Fermionic UV completions of Composite Higgs models. *JHEP*, 03:077, 2014. doi:[10.1007/JHEP03\(2014\)077](https://doi.org/10.1007/JHEP03(2014)077).
- [30] James Barnard, Tony Gherghetta, and Tirtha Sankar Ray. UV descriptions of composite Higgs models without elementary scalars. *JHEP*, 02:002, 2014. doi:[10.1007/JHEP02\(2014\)002](https://doi.org/10.1007/JHEP02(2014)002).
- [31] Roberto Contino. The Higgs as a Composite Nambu-Goldstone Boson. In *Physics of the large and the small, TASI 09, proceedings of the Theoretical Advanced Study Institute in Elementary Particle Physics, Boulder, Colorado, USA, 1-26 June 2009*, pages 235–306, 2011. doi:[10.1142/9789814327183_0005](https://doi.org/10.1142/9789814327183_0005).
- [32] A Wulzer. Composite higgs models - lecture 1: Ictp summer school on particle physics, 2015.
- [33] S. Coleman, J. Wess, and Bruno Zumino. Structure of phenomenological lagrangians. i. *Phys. Rev.*, 177:2239–2247, Jan 1969. doi:[10.1103/PhysRev.177.2239](https://doi.org/10.1103/PhysRev.177.2239).
- [34] Curtis G. Callan, Sidney Coleman, J. Wess, and Bruno Zumino. Structure of phenomenological lagrangians. ii. *Phys. Rev.*, 177:2247–2250, Jan 1969. doi:[10.1103/PhysRev.177.2247](https://doi.org/10.1103/PhysRev.177.2247).
- [35] Steven Weinberg. Effective gauge theories. *Physics Letters B*, 91(1):51–55, 1980. ISSN 0370-2693. doi:[https://doi.org/10.1016/0370-2693\(80\)90660-7](https://doi.org/10.1016/0370-2693(80)90660-7).
- [36] Andrea Romanino. The standard model of particle physics: Baikal summer jinr-isu school proceedings, 2009.
- [37] Tilman Plehn. Lectures on LHC Physics. *Lect. Notes Phys.*, 844:1–193, 2012. doi:[10.1007/978-3-642-24040-9](https://doi.org/10.1007/978-3-642-24040-9).
- [38] Ties Behnke, James E. Brau, Brian Foster, Juan Fuster, Mike Harrison, James McEwan Paterson, Michael Peskin, Marcel Stanitzki, Nicholas Walker, and Hitoshi Yamamoto. The International Linear Collider Technical Design Report - Volume 1: Executive Summary, 2013.
- [39] T. K. Charles et al. The Compact Linear Collider (CLIC) - 2018 Summary Report. *CERN Yellow Rep. Monogr.*, 1802:1–98, 2018. doi:[10.23731/CYRM-2018-002](https://doi.org/10.23731/CYRM-2018-002).
- [40] A. Abada et al. FCC-ee: The Lepton Collider. *Eur. Phys. J. ST*, 228(2): 261–623, 2019. doi:[10.1140/epjst/e2019-900045-4](https://doi.org/10.1140/epjst/e2019-900045-4).
- [41] Mingyi Dong et al. CEPC Conceptual Design Report: Volume 2 - Physics & Detector. *arXiv: 1811.10545*, 2018.

- [42] Jorge De Blas, Gauthier Durieux, Christophe Grojean, Jiayin Gu, and Ayan Paul. On the future of Higgs, electroweak and diboson measurements at lepton colliders. *JHEP*, 12:117, 2019. doi:[10.1007/JHEP12\(2019\)117](https://doi.org/10.1007/JHEP12(2019)117).
- [43] Csaba Csáki and Philip Tanedo. Beyond the Standard Model. In *2013 European School of High-Energy Physics*, 2015. doi:[10.5170/CERN-2015-004.169](https://doi.org/10.5170/CERN-2015-004.169).
- [44] Giuliano Panico and Andrea Wulzer. The Composite Nambu-Goldstone Higgs. *Lect. Notes Phys.*, 913:pp.1–316, 2016. doi:[10.1007/978-3-319-22617-0](https://doi.org/10.1007/978-3-319-22617-0).
- [45] Kaustubh Agashe, Roberto Contino, and Alex Pomarol. The Minimal composite Higgs model. *Nucl. Phys.*, B719:165–187, 2005. doi:[10.1016/j.nuclphysb.2005.04.035](https://doi.org/10.1016/j.nuclphysb.2005.04.035).
- [46] Brando Bellazzini, Csaba Csáki, and Javi Serra. Composite Higgses. *Eur. Phys. J.*, C74(5):2766, 2014. doi:[10.1140/epjc/s10052-014-2766-x](https://doi.org/10.1140/epjc/s10052-014-2766-x).
- [47] Alexandre Arbey, Giacomo Cacciapaglia, Haiying Cai, Aldo Deandrea, Solene Le Corre, and Francesco Sannino. Fundamental Composite Electroweak Dynamics: Status at the LHC. *Phys. Rev.*, D95(1):015028, 2017. doi:[10.1103/PhysRevD.95.015028](https://doi.org/10.1103/PhysRevD.95.015028).
- [48] Giacomo Cacciapaglia, Gabriele Ferretti, Thomas Flacke, and Hugo Serôdio. Light scalars in composite Higgs models. *Front.in Phys.*, 7:22, 2019. doi:[10.3389/fphy.2019.00022](https://doi.org/10.3389/fphy.2019.00022).
- [49] David B. Kaplan and Howard Georgi. SU(2) x U(1) Breaking by Vacuum Misalignment. *Phys. Lett.*, 136B:183–186, 1984. doi:[10.1016/0370-2693\(84\)91177-8](https://doi.org/10.1016/0370-2693(84)91177-8).
- [50] David B. Kaplan, Howard Georgi, and Savas Dimopoulos. Composite Higgs Scalars. *Phys. Lett.*, 136B:187–190, 1984. doi:[10.1016/0370-2693\(84\)91178-X](https://doi.org/10.1016/0370-2693(84)91178-X).
- [51] Michael J. Dugan, Howard Georgi, and David B. Kaplan. Anatomy of a Composite Higgs Model. *Nucl. Phys.*, B254:299–326, 1985. doi:[10.1016/0550-3213\(85\)90221-4](https://doi.org/10.1016/0550-3213(85)90221-4).
- [52] Giacomo Cacciapaglia and Francesco Sannino. Fundamental Composite (Goldstone) Higgs Dynamics. *JHEP*, 04:111, 2014. doi:[10.1007/JHEP04\(2014\)111](https://doi.org/10.1007/JHEP04(2014)111).
- [53] Leonard Susskind. Dynamics of spontaneous symmetry breaking in the weinberg-salam theory. *Phys. Rev. D*, 20:2619–2625, Nov 1979. doi:[10.1103/PhysRevD.20.2619](https://doi.org/10.1103/PhysRevD.20.2619).
- [54] Adrian Carmona. Lectures on composite higgs.
- [55] Gabriele Ferretti. Gauge theories of Partial Compositeness: Scenarios for Run-II of the LHC. *JHEP*, 06:107, 2016. doi:[10.1007/JHEP06\(2016\)107](https://doi.org/10.1007/JHEP06(2016)107).

- [56] Csaba Csáki, Salvator Lombardo, and Ofri Telem. TASI Lectures on Non-supersymmetric BSM Models. In *Proceedings, Theoretical Advanced Study Institute in Elementary Particle Physics : Anticipating the Next Discoveries in Particle Physics (TASI 2016): Boulder, CO, USA, June 6-July 1, 2016*, pages 501–570. WSP, WSP, 2018. doi:[10.1142/9789813233348_0007](https://doi.org/10.1142/9789813233348_0007).
- [57] Estia Eichten and Kenneth Lane. Dynamical breaking of weak interaction symmetries. *Physics Letters B*, 90(1):125–130, 1980. ISSN 0370-2693. doi:[https://doi.org/10.1016/0370-2693\(80\)90065-9](https://doi.org/10.1016/0370-2693(80)90065-9).
- [58] Savas Dimopoulos and John Ellis. Challenges for extended technicolour theories. *Nuclear Physics B*, 182(3):505–528, 1981. ISSN 0550-3213. doi:[https://doi.org/10.1016/0550-3213\(81\)90132-2](https://doi.org/10.1016/0550-3213(81)90132-2).
- [59] Giacomo Cacciapaglia. The dynamics of composite higgses. *Journal of Physics: Conference Series*, 623:012006, jun 2015. doi:[10.1088/1742-6596/623/1/012006](https://doi.org/10.1088/1742-6596/623/1/012006).
- [60] Gabriele Ferretti. UV Completions of Partial Compositeness: The Case for a SU(4) Gauge Group. *JHEP*, 06:142, 2014. doi:[10.1007/JHEP06\(2014\)142](https://doi.org/10.1007/JHEP06(2014)142).
- [61] Luca Vecchi. A dangerous irrelevant UV-completion of the composite Higgs. *JHEP*, 02:094, 2017. doi:[10.1007/JHEP02\(2017\)094](https://doi.org/10.1007/JHEP02(2017)094).
- [62] Giacomo Cacciapaglia, Haiying Cai, Aldo Deandrea, and Ashwani Kushwaha. Fundamental Composite Higgs model in SU(6)/SO(6), 2019.
- [63] Thomas DeGrand, Maarten Golterman, Ethan T. Neil, and Yigal Shamir. One-loop chiral perturbation theory with two fermion representations. *Phys. Rev.*, D94(2):025020, 2016. doi:[10.1103/PhysRevD.94.025020](https://doi.org/10.1103/PhysRevD.94.025020).
- [64] Alexander Belyaev, Giacomo Cacciapaglia, Haiying Cai, Gabriele Ferretti, Thomas Flacke, Alberto Parolini, and Hugo Serodio. Di-boson signatures as standard candles for partial compositeness. *JHEP*, 01:094, 2017. doi:[10.1007/JHEP01\(2017\)094](https://doi.org/10.1007/JHEP01(2017)094), [10.1007/JHEP12\(2017\)088](https://doi.org/10.1007/JHEP12(2017)088). [Erratum: *JHEP*12,088(2017)].
- [65] Gabriele Ferretti. Composite Higgs bosons. *PoS*, CHARGED2018:026, 2019. doi:[10.22323/1.339.0026](https://doi.org/10.22323/1.339.0026).
- [66] Randy Lewis, Claudio Pica, and Francesco Sannino. Light Asymmetric Dark Matter on the Lattice: SU(2) Technicolor with Two Fundamental Flavors. *Phys. Rev. D*, 85:014504, 2012. doi:[10.1103/PhysRevD.85.014504](https://doi.org/10.1103/PhysRevD.85.014504).
- [67] Ari Hietanen, Randy Lewis, Claudio Pica, and Francesco Sannino. Fundamental Composite Higgs Dynamics on the Lattice: SU(2) with Two Flavors. *JHEP*, 07:116, 2014. doi:[10.1007/JHEP07\(2014\)116](https://doi.org/10.1007/JHEP07(2014)116).
- [68] Sidney Coleman and Erick Weinberg. Radiative corrections as the origin of spontaneous symmetry breaking. *Phys. Rev. D*, 7:1888–1910, Mar 1973. doi:[10.1103/PhysRevD.7.1888](https://doi.org/10.1103/PhysRevD.7.1888).

- [69] M. et al Tanabashi. Review of particle physics. *Phys. Rev. D*, 98:030001, Aug 2018. doi:[10.1103/PhysRevD.98.030001](https://doi.org/10.1103/PhysRevD.98.030001).
- [70] Gero von Gersdorff, Eduardo Pontón, and Rogerio Rosenfeld. The Dynamical Composite Higgs. *JHEP*, 06:119, 2015. doi:[10.1007/JHEP06\(2015\)119](https://doi.org/10.1007/JHEP06(2015)119).
- [71] David B. Kaplan. Flavor at SSC energies: A New mechanism for dynamically generated fermion masses. *Nucl. Phys.*, B365:259–278, 1991. doi:[10.1016/S0550-3213\(05\)80021-5](https://doi.org/10.1016/S0550-3213(05)80021-5).
- [72] Diogo Buarque Franzosi and Alberto Tonero. Top-quark Partial Compositeness beyond the effective field theory paradigm. *JHEP*, 04:040, 2020. doi:[10.1007/JHEP04\(2020\)040](https://doi.org/10.1007/JHEP04(2020)040).
- [73] Alessandro Agugliaro. *Composite Higgs: theory and phenomenology*. PhD thesis, Universita Degli Studi Firenze, 2018.
- [74] Oleksii Matsedonskyi. *Composite Higgs, Top Partners and the LHC*. PhD thesis, Universita degli Studi di Padova, January 2014.
- [75] Nicolas Bizot, Giacomo Cacciapaglia, and Thomas Flacke. Common exotic decays of top partners. *JHEP*, 06:065, 2018. doi:[10.1007/JHEP06\(2018\)065](https://doi.org/10.1007/JHEP06(2018)065).
- [76] Yasuhiro Okada and Luca Panizzi. LHC signatures of vector-like quarks. *Adv. High Energy Phys.*, 2013:364936, 2013. doi:[10.1155/2013/364936](https://doi.org/10.1155/2013/364936).
- [77] Mathieu Buchkremer, Giacomo Cacciapaglia, Aldo Deandrea, and Luca Panizzi. Model Independent Framework for Searches of Top Partners. *Nucl. Phys.*, B876:376–417, 2013. doi:[10.1016/j.nuclphysb.2013.08.010](https://doi.org/10.1016/j.nuclphysb.2013.08.010).
- [78] N. Arkani-Hamed, A. G. Cohen, E. Katz, and A. E. Nelson. The Littlest Higgs. *JHEP*, 07:034, 2002. doi:[10.1088/1126-6708/2002/07/034](https://doi.org/10.1088/1126-6708/2002/07/034).
- [79] Martin Schmaltz and David Tucker-Smith. Little Higgs review. *Ann. Rev. Nucl. Part. Sci.*, 55:229–270, 2005. doi:[10.1146/annurev.nucl.55.090704.151502](https://doi.org/10.1146/annurev.nucl.55.090704.151502).
- [80] Roshan Foadi, Mads T. Frandsen, and Francesco Sannino. 125 GeV Higgs boson from a not so light technicolor scalar. *Phys. Rev. D*, 87(9):095001, 2013. doi:[10.1103/PhysRevD.87.095001](https://doi.org/10.1103/PhysRevD.87.095001).
- [81] Shinya Matsuzaki and Koichi Yamawaki. Is 125 GeV techni-dilaton found at LHC? *Phys. Lett. B*, 719:378–382, 2013. doi:[10.1016/j.physletb.2013.01.031](https://doi.org/10.1016/j.physletb.2013.01.031).
- [82] Adam Falkowski. Pseudo-goldstone Higgs production via gluon fusion. *Phys. Rev. D*, 77:055018, 2008. doi:[10.1103/PhysRevD.77.055018](https://doi.org/10.1103/PhysRevD.77.055018).
- [83] Avik Banerjee, Gautam Bhattacharyya, Nilanjana Kumar, and Tirtha Sankar Ray. Constraining Composite Higgs Models using LHC data. *JHEP*, 03:062, 2018. doi:[10.1007/JHEP03\(2018\)062](https://doi.org/10.1007/JHEP03(2018)062).
- [84] Avik Banerjee, Sayan Dasgupta, and Tirtha Sankar Ray. Probing composite Higgs boson substructure at the HL-LHC. *Phys. Rev. D*, 104(9):095021, 2021. doi:[10.1103/PhysRevD.104.095021](https://doi.org/10.1103/PhysRevD.104.095021).

- [85] Florian Goertz. Composite Higgs theory. *PoS*, ALPS2018:012, 2018. doi:[10.22323/1.330.0012](https://doi.org/10.22323/1.330.0012).
- [86] Simone Blasi. *Hierarchies and new symmetries: from flavored axions to composite Higgs*. PhD thesis, U. Heidelberg (main), 2020.
- [87] Joerg Jaeckel and Andreas Ringwald. The Low-Energy Frontier of Particle Physics. *Ann. Rev. Nucl. Part. Sci.*, 60:405–437, 2010. doi:[10.1146/annurev.nucl.012809.104433](https://doi.org/10.1146/annurev.nucl.012809.104433).
- [88] Paola Arias, Davide Cadamuro, Mark Goodsell, Joerg Jaeckel, Javier Redondo, and Andreas Ringwald. WISPy Cold Dark Matter. *JCAP*, 06:013, 2012. doi:[10.1088/1475-7516/2012/06/013](https://doi.org/10.1088/1475-7516/2012/06/013).
- [89] David J. E. Marsh. Axions and ALPs: a very short introduction. In *13th Patras Workshop on Axions, WIMPs and WISPs*, pages 59–74, 2018. doi:[10.3204/DESY-PROC-2017-02/marsh_david](https://doi.org/10.3204/DESY-PROC-2017-02/marsh_david).
- [90] R. D. Peccei and Helen R. Quinn. Cp conservation in the presence of pseudoparticles. *Phys. Rev. Lett.*, 38:1440–1443, Jun 1977. doi:[10.1103/PhysRevLett.38.1440](https://doi.org/10.1103/PhysRevLett.38.1440).
- [91] R. D. Peccei and Helen R. Quinn. Constraints imposed by cp conservation in the presence of pseudoparticles. *Phys. Rev. D*, 16:1791–1797, Sep 1977. doi:[10.1103/PhysRevD.16.1791](https://doi.org/10.1103/PhysRevD.16.1791).
- [92] Leanne D. Duffy and Karl van Bibber. Axions as Dark Matter Particles. *New J. Phys.*, 11:105008, 2009. doi:[10.1088/1367-2630/11/10/105008](https://doi.org/10.1088/1367-2630/11/10/105008).
- [93] David J. E. Marsh. Axion Cosmology. *Phys. Rept.*, 643:1–79, 2016. doi:[10.1016/j.physrep.2016.06.005](https://doi.org/10.1016/j.physrep.2016.06.005).
- [94] Jonathan Kozaczuk and Travis A. W. Martin. Extending LHC Coverage to Light Pseudoscalar Mediators and Coy Dark Sectors. *JHEP*, 04:046, 2015. doi:[10.1007/JHEP04\(2015\)046](https://doi.org/10.1007/JHEP04(2015)046).
- [95] Matthew J. Dolan, Felix Kahlhoefer, Christopher McCabe, and Kai Schmidt-Hoberg. A taste of dark matter: Flavour constraints on pseudoscalar mediators. *JHEP*, 03:171, 2015. doi:[10.1007/JHEP03\(2015\)171](https://doi.org/10.1007/JHEP03(2015)171). [Erratum: *JHEP* 07, 103 (2015)].
- [96] Yasunori Nomura and Jesse Thaler. Dark Matter through the Axion Portal. *Phys. Rev. D*, 79:075008, 2009. doi:[10.1103/PhysRevD.79.075008](https://doi.org/10.1103/PhysRevD.79.075008).
- [97] Brando Bellazzini, Alberto Mariotti, Diego Redigolo, Filippo Sala, and Javi Serra. R-axion at colliders. *Phys. Rev. Lett.*, 119(14):141804, 2017. doi:[10.1103/PhysRevLett.119.141804](https://doi.org/10.1103/PhysRevLett.119.141804).
- [98] Katherine Freese, Joshua A. Frieman, and Angela V. Olinto. Natural inflation with pseudo nambu-goldstone bosons. *Phys. Rev. Lett.*, 65:3233–3236, Dec 1990. doi:[10.1103/PhysRevLett.65.3233](https://doi.org/10.1103/PhysRevLett.65.3233).

- [99] Giacomo Cacciapaglia, Gabriele Ferretti, Thomas Flacke, and Hugo Serodio. Revealing timid pseudo-scalars with taus at the LHC. *Eur. Phys. J.*, C78(9):724, 2018. doi:[10.1140/epjc/s10052-018-6183-4](https://doi.org/10.1140/epjc/s10052-018-6183-4).
- [100] Albert M Sirunyan et al. Search for low-mass resonances decaying into bottom quark-antiquark pairs in proton-proton collisions at $\sqrt{s} = 13$ TeV. *Phys. Rev.*, D99(1):012005, 2019. doi:[10.1103/PhysRevD.99.012005](https://doi.org/10.1103/PhysRevD.99.012005).
- [101] M. Aaboud et al. Search for low-mass dijet resonances using trigger-level jets with the ATLAS detector in pp collisions at $\sqrt{s} = 13$ TeV. *Phys. Rev. Lett.*, 121(8):081801, 2018. doi:[10.1103/PhysRevLett.121.081801](https://doi.org/10.1103/PhysRevLett.121.081801).
- [102] Albert M Sirunyan et al. Search for a narrow resonance lighter than 200 GeV decaying to a pair of muons in proton-proton collisions at $\sqrt{s} = 13$ TeV, 2019.
- [103] Georges Aad et al. Search for high-mass dilepton resonances using 139 fb^{-1} of pp collision data collected at $\sqrt{s} = 13$ TeV with the ATLAS detector. *Phys. Lett.*, B796:68–87, 2019. doi:[10.1016/j.physletb.2019.07.016](https://doi.org/10.1016/j.physletb.2019.07.016).
- [104] Alberto Mariotti, Diego Redigolo, Filippo Sala, and Kohsaku Tobioka. New LHC bound on low-mass diphoton resonances. *Phys. Lett. B*, 783:13–18, 2018. doi:[10.1016/j.physletb.2018.06.039](https://doi.org/10.1016/j.physletb.2018.06.039).
- [105] Albert M Sirunyan et al. Search for a standard model-like Higgs boson in the mass range between 70 and 110 GeV in the diphoton final state in proton-proton collisions at $\sqrt{s} = 8$ and 13 TeV. *Phys. Lett.*, B793:320–347, 2019. doi:[10.1016/j.physletb.2019.03.064](https://doi.org/10.1016/j.physletb.2019.03.064).
- [106] Morad Aaboud et al. Search for resonances in diphoton events at $\sqrt{s}=13$ TeV with the ATLAS detector. *JHEP*, 09:001, 2016. doi:[10.1007/JHEP09\(2016\)001](https://doi.org/10.1007/JHEP09(2016)001).
- [107] Morad Aaboud et al. Search for additional heavy neutral Higgs and gauge bosons in the ditau final state produced in 36 fb^{-1} of pp collisions at $\sqrt{s} = 13$ TeV with the ATLAS detector. *JHEP*, 01:055, 2018. doi:[10.1007/JHEP01\(2018\)055](https://doi.org/10.1007/JHEP01(2018)055).
- [108] Jihn E. Kim. Composite invisible axion. *Phys. Rev. D*, 31:1733–1735, Apr 1985. doi:[10.1103/PhysRevD.31.1733](https://doi.org/10.1103/PhysRevD.31.1733).
- [109] Edward Witten. Global Aspects of Current Algebra. *Nucl. Phys.*, B223:422–432, 1983. doi:[10.1016/0550-3213\(83\)90063-9](https://doi.org/10.1016/0550-3213(83)90063-9).
- [110] J. Wess and B. Zumino. Consequences of anomalous Ward identities. *Phys. Lett.*, 37B:95–97, 1971. doi:[10.1016/0370-2693\(71\)90582-X](https://doi.org/10.1016/0370-2693(71)90582-X).
- [111] Adam Alloul, Neil D. Christensen, Céline Degrande, Claude Duhr, and Benjamin Fuks. FeynRules 2.0 - A complete toolbox for tree-level phenomenology. *Comput. Phys. Commun.*, 185:2250–2300, 2014. doi:[10.1016/j.cpc.2014.04.012](https://doi.org/10.1016/j.cpc.2014.04.012).
- [112] Richard D. Ball, Valerio Bertone, Stefano Carrazza, Luigi Del Debbio, Stefano Forte, Alberto Guffanti, Nathan P. Hartland, and Juan Rojo. Parton distributions with QED corrections. *Nucl. Phys.*, B877:290–320, 2013. doi:[10.1016/j.nuclphysb.2013.10.010](https://doi.org/10.1016/j.nuclphysb.2013.10.010).

- [113] J. Alwall, R. Frederix, S. Frixione, V. Hirschi, F. Maltoni, O. Mattelaer, H. S. Shao, T. Stelzer, P. Torrielli, and M. Zaro. The automated computation of tree-level and next-to-leading order differential cross sections, and their matching to parton shower simulations. *JHEP*, 07:079, 2014. doi:[10.1007/JHEP07\(2014\)079](https://doi.org/10.1007/JHEP07(2014)079).
- [114] Celine Degrande, Claude Duhr, Benjamin Fuks, David Grellscheid, Olivier Mattelaer, and Thomas Reiter. UFO - The Universal FeynRules Output. *Comput. Phys. Commun.*, 183:1201–1214, 2012. doi:[10.1016/j.cpc.2012.01.022](https://doi.org/10.1016/j.cpc.2012.01.022).
- [115] J. de Favereau, C. Delaere, P. Demin, A. Giammanco, V. Lemaître, A. Mertens, and M. Selvaggi. DELPHES 3, A modular framework for fast simulation of a generic collider experiment. *JHEP*, 02:057, 2014. doi:[10.1007/JHEP02\(2014\)057](https://doi.org/10.1007/JHEP02(2014)057).
- [116] Matteo Cacciari, Gavin P. Salam, and Gregory Soyez. The anti- k_t jet clustering algorithm. *JHEP*, 04:063, 2008. doi:[10.1088/1126-6708/2008/04/063](https://doi.org/10.1088/1126-6708/2008/04/063).
- [117] Matteo Cacciari, Gavin P. Salam, and Gregory Soyez. FastJet User Manual. *Eur. Phys. J. C*, 72:1896, 2012. doi:[10.1140/epjc/s10052-012-1896-2](https://doi.org/10.1140/epjc/s10052-012-1896-2).
- [118] Torbjorn Sjostrand, Stephen Mrenna, and Peter Z. Skands. A Brief Introduction to PYTHIA 8.1. *Comput. Phys. Commun.*, 178:852–867, 2008. doi:[10.1016/j.cpc.2008.01.036](https://doi.org/10.1016/j.cpc.2008.01.036).
- [119] Eric Conte, Benjamin Fuks, and Guillaume Serret. MadAnalysis 5, A User-Friendly Framework for Collider Phenomenology. *Comput. Phys. Commun.*, 184:222–256, 2013. doi:[10.1016/j.cpc.2012.09.009](https://doi.org/10.1016/j.cpc.2012.09.009).
- [120] Eric Conte and Benjamin Fuks. Confronting new physics theories to LHC data with MADANALYSIS 5. *Int. J. Mod. Phys. A*, 33(28):1830027, 2018. doi:[10.1142/S0217751X18300272](https://doi.org/10.1142/S0217751X18300272).
- [121] Claire Adam-Bourdarios, Glen Cowan, Cécile Germain, Isabelle Guyon, Balázs Kégl, and David Rousseau. The Higgs boson machine learning challenge. In Glen Cowan, Cécile Germain, Isabelle Guyon, Balázs Kégl, and David Rousseau, editors, *Proceedings of the NIPS 2014 Workshop on High-energy Physics and Machine Learning*, volume 42 of *Proceedings of Machine Learning Research*, pages 19–55, Montreal, Canada, 13 Dec 2015. PMLR.
- [122] Curtis A. Meyer, Mike Williams, and Robert Bradford. Computing invariant masses and missing masses. In *CLAS-NOTE 04-008*. Carnegie Mellon University, 2004. URL https://www.jlab.org/Hall-B/notes/clas_notes04/2004-008.pdf.
- [123] Leif Lönnblad, Carsten Peterson, and Thorsteinn Rognvaldsson. Using neural networks to identify jets. *Nuclear Physics B*, 349(3):675–702, 1991. ISSN 0550-3213. doi:[https://doi.org/10.1016/0550-3213\(91\)90392-B](https://doi.org/10.1016/0550-3213(91)90392-B).
- [124] Byron P. Roe, Hai-Jun Yang, Ji Zhu, Yong Liu, Ion Stancu, and Gordon McGregor. Boosted decision trees, an alternative to artificial neural networks. *Nucl. Instrum. Meth. A*, 543(2-3):577–584, 2005. doi:[10.1016/j.nima.2004.12.018](https://doi.org/10.1016/j.nima.2004.12.018).

- [125] Hai-Jun Yang, Byron P. Roe, and Ji Zhu. Studies of boosted decision trees for miniboone particle identification. *Nuclear Instruments and Methods in Physics Research Section A: Accelerators, Spectrometers, Detectors and Associated Equipment*, 555(1-2):370–385, Dec 2005. ISSN 0168-9002. doi:[10.1016/j.nima.2005.09.022](https://doi.org/10.1016/j.nima.2005.09.022).
- [126] Mariana Frank, Benjamin Fuks, Katri Huitu, Subhadeep Mondal, Santosh Kumar Rai, and Harri Waltari. Left-right supersymmetric option at a high-energy upgrade of the LHC. *Phys. Rev. D*, 101(11):115014, 2020. doi:[10.1103/PhysRevD.101.115014](https://doi.org/10.1103/PhysRevD.101.115014).
- [127] T. Aaltonen et al. Observation of Single Top Quark Production and Measurement of $|V_{tb}|$ with CDF. *Phys. Rev. D*, 82:112005, 2010. doi:[10.1103/PhysRevD.82.112005](https://doi.org/10.1103/PhysRevD.82.112005).
- [128] Bernard Aubert et al. Measurement of CP-violating asymmetries in the $B^0 \rightarrow K^+K^-K^0$ Dalitz plot. In *33rd International Conference on High Energy Physics*, 7 2006.
- [129] V.M. Abazov et al. Search for single top quarks in the tau+jets channel using 4.8 fb-1 of pp collision data. *Physics Letters B*, 690(1):5–14, 2010. ISSN 0370-2693. doi:<https://doi.org/10.1016/j.physletb.2010.05.003>.
- [130] V. M. Abazov et al. Observation of Single Top Quark Production. *Phys. Rev. Lett.*, 103:092001, 2009. doi:[10.1103/PhysRevLett.103.092001](https://doi.org/10.1103/PhysRevLett.103.092001).
- [131] V. M. Abazov et al. Evidence for production of single top quarks. *Phys. Rev. D*, 78:012005, 2008. doi:[10.1103/PhysRevD.78.012005](https://doi.org/10.1103/PhysRevD.78.012005).
- [132] V. M. Abazov et al. Evidence for production of single top quarks and first direct measurement of $|V_{tb}|$. *Phys. Rev. Lett.*, 98:181802, 2007. doi:[10.1103/PhysRevLett.98.181802](https://doi.org/10.1103/PhysRevLett.98.181802).
- [133] G. Aad et al. Measurement of the top quark pair cross section with atlas in pp collisions at s=7 tev using final states with an electron or a muon and a hadronically decaying tau lepton. *Physics Letters B*, 717(1):89–108, 2012. ISSN 0370-2693. doi:<https://doi.org/10.1016/j.physletb.2012.09.032>.
- [134] G. Aad et al. Evidence for the associated production of a w boson and a top quark in atlas at s=7tev. *Physics Letters B*, 716(1):142–159, 2012. ISSN 0370-2693. doi:<https://doi.org/10.1016/j.physletb.2012.08.011>.
- [135] L. Breiman, J. Friedman, R. Olshen, and C. Stone. *Classification and Regression Trees*. Wadsworth and Brooks, Monterey, CA, 1984.
- [136] Yann Coadou. Boosted Decision Trees and Applications. *EPJ Web Conf.*, 55: 02004, 2013. doi:[10.1051/epjconf/20135502004](https://doi.org/10.1051/epjconf/20135502004).
- [137] Alexey Natekin and Alois Knoll. Gradient boosting machines, a tutorial. *Frontiers in Neurorobotics*, 7:21, 2013. ISSN 1662-5218. doi:[10.3389/fnbot.2013.00021](https://doi.org/10.3389/fnbot.2013.00021).

- [138] Jerome H. Friedman. Greedy function approximation: A gradient boosting machine. *Annals of Statistics*, 29:1189–1232, 2000.
- [139] Glen Cowan, Kyle Cranmer, Eilam Gross, and Ofer Vitells. Asymptotic formulae for likelihood-based tests of new physics. *Eur. Phys. J.*, C71:1554, 2011. doi:[10.1140/epjc/s10052-011-1554-0](https://doi.org/10.1140/epjc/s10052-011-1554-0), [10.1140/epjc/s10052-013-2501-z](https://doi.org/10.1140/epjc/s10052-013-2501-z). [Erratum: *Eur. Phys. J.*C73,2501(2013)].
- [140] Martin Bauer, Mathias Heiles, Matthias Neubert, and Andrea Thamm. Axion-Like Particles at Future Colliders. *Eur. Phys. J. C*, 79(1):74, 2019. doi:[10.1140/epjc/s10052-019-6587-9](https://doi.org/10.1140/epjc/s10052-019-6587-9).
- [141] Martin Bauer, Matthias Neubert, and Andrea Thamm. Collider Probes of Axion-Like Particles. *JHEP*, 12:044, 2017. doi:[10.1007/JHEP12\(2017\)044](https://doi.org/10.1007/JHEP12(2017)044).
- [142] Search for a neutral MSSM Higgs boson decaying into $\tau\tau$ at 13 TeV. 6 2016.
- [143] David d’Enterria. Collider constraints on axion-like particles. In *Workshop on Feebly Interacting Particles*, 2 2021.
- [144] G. Cacciapaglia, A. Deandrea, A. M. Iyer, and K. Sridhar. Tera-Zooming in on light (composite) axion-like particles. 4 2021.
- [145] Ari Hietanen, Randy Lewis, Claudio Pica, and Francesco Sannino. Composite Goldstone Dark Matter: Experimental Predictions from the Lattice. *JHEP*, 12: 130, 2014. doi:[10.1007/JHEP12\(2014\)130](https://doi.org/10.1007/JHEP12(2014)130).
- [146] Tilman Plehn. *Higgs Physics*, pages 1–62. Springer Berlin Heidelberg, Berlin, Heidelberg, 2012. ISBN 978-3-642-24040-9. doi:[10.1007/978-3-642-24040-9_1](https://doi.org/10.1007/978-3-642-24040-9_1).
- [147] Miguel A. Monroy-Rodríguez and Christine Allen. The end of the macho era, revisited: New limits on macho masses from halo wide binaries. *The Astrophysical Journal*, 790(2):159, Jul 2014. ISSN 1538-4357. doi:[10.1088/0004-637x/790/2/159](https://doi.org/10.1088/0004-637x/790/2/159).
- [148] Teng Ma and Giacomo Cacciapaglia. Fundamental Composite 2HDM: SU(N) with 4 flavours. *JHEP*, 03:211, 2016. doi:[10.1007/JHEP03\(2016\)211](https://doi.org/10.1007/JHEP03(2016)211).
- [149] Chengfeng Cai, Giacomo Cacciapaglia, and Hong-Hao Zhang. Vacuum alignment in a composite 2HDM. *JHEP*, 01:130, 2019. doi:[10.1007/JHEP01\(2019\)130](https://doi.org/10.1007/JHEP01(2019)130).
- [150] Stefano Colucci, Benjamin Fuks, Federica Giacchino, Laura Lopez Honorez, Michel H. G. Tytgat, and Jérôme Vandecasteele. Top-philic Vector-Like Portal to Scalar Dark Matter. *Phys. Rev.*, D98:035002, 2018. doi:[10.1103/PhysRevD.98.035002](https://doi.org/10.1103/PhysRevD.98.035002).
- [151] Stefano Colucci, Federica Giacchino, Michel H.G. Tytgat, and Jérôme Vandecasteele. Radiative corrections to vectorlike portal dark matter. *Phys. Rev. D*, 98(11):115029, 2018. doi:[10.1103/PhysRevD.98.115029](https://doi.org/10.1103/PhysRevD.98.115029).
- [152] F. Zwicky. On the Masses of Nebulae and of Clusters of Nebulae. *apj*, 86:217, October 1937. doi:[10.1086/143864](https://doi.org/10.1086/143864).

- [153] Vera C. Rubin and Jr. Ford, W. Kent. Rotation of the Andromeda Nebula from a Spectroscopic Survey of Emission Regions. *apj*, 159:379, February 1970. doi:[10.1086/150317](https://doi.org/10.1086/150317).
- [154] David S. Davis and Raymond E. White, III. Rosat temperatures and abundances for a complete sample of elliptical galaxies. *Astrophys. J. Lett.*, 470:L35, 1996. doi:[10.1086/310289](https://doi.org/10.1086/310289).
- [155] S. W. Allen, D. A. Rapetti, R. W. Schmidt, H. Ebeling, G. Morris, and A. C. Fabian. Improved constraints on dark energy from Chandra X-ray observations of the largest relaxed galaxy clusters. *Mon. Not. Roy. Astron. Soc.*, 383:879–896, 2008. doi:[10.1111/j.1365-2966.2007.12610.x](https://doi.org/10.1111/j.1365-2966.2007.12610.x).
- [156] Richard Massey, Thomas Kitching, and Johan Richard. The dark matter of gravitational lensing. *Rept. Prog. Phys.*, 73:086901, 2010. doi:[10.1088/0034-4885/73/8/086901](https://doi.org/10.1088/0034-4885/73/8/086901).
- [157] Douglas Clowe, Marusa Bradac, Anthony H. Gonzalez, Maxim Markevitch, Scott W. Randall, Christine Jones, and Dennis Zaritsky. A direct empirical proof of the existence of dark matter. *Astrophys. J. Lett.*, 648:L109–L113, 2006. doi:[10.1086/508162](https://doi.org/10.1086/508162).
- [158] P.A.R. Ade et al. Planck 2013 results. XVI. Cosmological parameters. *Astron. Astrophys.*, 571:A16, 2014. doi:[10.1051/0004-6361/201321591](https://doi.org/10.1051/0004-6361/201321591).
- [159] Yoshiaki Sofue and Vera Rubin. Rotation curves of spiral galaxies. *Ann. Rev. Astron. Astrophys.*, 39:137–174, 2001. doi:[10.1146/annurev.astro.39.1.137](https://doi.org/10.1146/annurev.astro.39.1.137).
- [160] N. Aghanim et al. Planck 2018 results. VI. Cosmological parameters, 7 2018.
- [161] Gianfranco Bertone, editor. *Particle Dark Matter: Observations, Models and Searches*. Cambridge University Press, 2010. doi:[10.1017/CBO9780511770739](https://doi.org/10.1017/CBO9780511770739).
- [162] T. Binoth and J.J. van der Bij. Influence of strongly coupled, hidden scalars on Higgs signals. *Z. Phys. C*, 75:17–25, 1997. doi:[10.1007/s002880050442](https://doi.org/10.1007/s002880050442).
- [163] Robert M. Schabinger and James D. Wells. A Minimal spontaneously broken hidden sector and its impact on Higgs boson physics at the large hadron collider. *Phys. Rev. D*, 72:093007, 2005. doi:[10.1103/PhysRevD.72.093007](https://doi.org/10.1103/PhysRevD.72.093007).
- [164] Brian Patt and Frank Wilczek. Higgs-field portal into hidden sectors. 5 2006.
- [165] Markus Ahlers, Joerg Jaeckel, Javier Redondo, and Andreas Ringwald. Probing Hidden Sector Photons through the Higgs Window. *Phys. Rev. D*, 78:075005, 2008. doi:[10.1103/PhysRevD.78.075005](https://doi.org/10.1103/PhysRevD.78.075005).
- [166] Brian Batell, Maxim Pospelov, and Adam Ritz. Probing a Secluded U(1) at B-factories. *Phys. Rev. D*, 79:115008, 2009. doi:[10.1103/PhysRevD.79.115008](https://doi.org/10.1103/PhysRevD.79.115008).
- [167] Christoph Englert, Joerg Jaeckel, Michael Spannowsky, and Panagiotis Stylianou. Power meets Precision to explore the Symmetric Higgs Portal. *Phys. Lett. B*, 806:135526, 2020. doi:[10.1016/j.physletb.2020.135526](https://doi.org/10.1016/j.physletb.2020.135526).

- [168] Chiara Arina. Impact of cosmological and astrophysical constraints on dark matter simplified models. *Front. Astron. Space Sci.*, 5:30, 2018. doi:[10.3389/fspas.2018.00030](https://doi.org/10.3389/fspas.2018.00030).
- [169] Haipeng An, Lian-Tao Wang, and Hao Zhang. Dark matter with t -channel mediator: a simple step beyond contact interaction. *Phys. Rev. D*, 89(11):115014, 2014. doi:[10.1103/PhysRevD.89.115014](https://doi.org/10.1103/PhysRevD.89.115014).
- [170] Seungwon Baek, Pyungwon Ko, and Peiwen Wu. Top-philic Scalar Dark Matter with a Vector-like Fermionic Top Partner. *JHEP*, 10:117, 2016. doi:[10.1007/JHEP10\(2016\)117](https://doi.org/10.1007/JHEP10(2016)117).
- [171] Seungwon Baek, Pyungwon Ko, and Peiwen Wu. Heavy quark-philic scalar dark matter with a vector-like fermion portal. *JCAP*, 07:008, 2018. doi:[10.1088/1475-7516/2018/07/008](https://doi.org/10.1088/1475-7516/2018/07/008).
- [172] Abhishek Kumar and Sean Tulin. Top-flavored dark matter and the forward-backward asymmetry. *Phys. Rev. D*, 87(9):095006, 2013. doi:[10.1103/PhysRevD.87.095006](https://doi.org/10.1103/PhysRevD.87.095006).
- [173] Can Kilic, Matthew D. Klimek, and Jiang-Hao Yu. Signatures of Top Flavored Dark Matter. *Phys. Rev. D*, 91(5):054036, 2015. doi:[10.1103/PhysRevD.91.054036](https://doi.org/10.1103/PhysRevD.91.054036).
- [174] Chiara Arina et al. A comprehensive approach to dark matter studies: exploration of simplified top-philic models. *JHEP*, 11:111, 2016. doi:[10.1007/JHEP11\(2016\)111](https://doi.org/10.1007/JHEP11(2016)111).
- [175] M.A. Gomez, C.B. Jackson, and G. Shaughnessy. Dark Matter on Top. *JCAP*, 12:025, 2014. doi:[10.1088/1475-7516/2014/12/025](https://doi.org/10.1088/1475-7516/2014/12/025).
- [176] Yue Zhang. Top Quark Mediated Dark Matter. *Phys. Lett. B*, 720:137–141, 2013. doi:[10.1016/j.physletb.2013.01.063](https://doi.org/10.1016/j.physletb.2013.01.063).
- [177] Brian Batell, Tongyan Lin, and Lian-Tao Wang. Flavored Dark Matter and R-Parity Violation. *JHEP*, 01:075, 2014. doi:[10.1007/JHEP01\(2014\)075](https://doi.org/10.1007/JHEP01(2014)075).
- [178] Kingman Cheung, Kentarou Mawatari, Eibun Senaha, Po-Yan Tseng, and Tzu-Chiang Yuan. The Top Window for dark matter. *JHEP*, 10:081, 2010. doi:[10.1007/JHEP10\(2010\)081](https://doi.org/10.1007/JHEP10(2010)081).
- [179] M. Beneke, A. Broggio, C. Hasner, and M. Vollmann. Energetic gamma-rays from tev scale dark matter annihilation resummed. *Physics Letters B*, 786:347–354, Nov 2018. ISSN 0370-2693. doi:[10.1016/j.physletb.2018.10.008](https://doi.org/10.1016/j.physletb.2018.10.008).
- [180] Brando Bellazzini, Csaba Csaki, Jay Hubisz, Javi Serra, and John Terning. Composite Higgs Sketch. *JHEP*, 11:003, 2012. doi:[10.1007/JHEP11\(2012\)003](https://doi.org/10.1007/JHEP11(2012)003).
- [181] Geneviève Bélanger, Fawzi Boudjema, Andreas Goudelis, Alexander Pukhov, and Bryan Zaldivar. micrOMEGAs5.0 : Freeze-in. *Comput. Phys. Commun.*, 231:173–186, 2018. doi:[10.1016/j.cpc.2018.04.027](https://doi.org/10.1016/j.cpc.2018.04.027).

- [182] Adam Alloul, Neil D. Christensen, Céline Degrande, Claude Duhr, and Benjamin Fuks. FeynRules 2.0 - A complete toolbox for tree-level phenomenology. *Comput. Phys. Commun.*, 185:2250–2300, 2014. doi:[10.1016/j.cpc.2014.04.012](https://doi.org/10.1016/j.cpc.2014.04.012).
- [183] Alexander Belyaev, Neil D. Christensen, and Alexander Pukhov. CalcHeP 3.4 for collider physics within and beyond the standard model. *Computer Physics Communications*, 184(7):1729–1769, Jul 2013. ISSN 0010-4655. doi:[10.1016/j.cpc.2013.01.014](https://doi.org/10.1016/j.cpc.2013.01.014).
- [184] Neil Christensen, Priscila de Aquino, Celine Degrande, Claude Duhr, Benjamin Fuks, Michel Herquet, Fabio Maltoni, and Steffen Schumann. A comprehensive approach to new physics simulations. *The European Physical Journal C*, 71(2), Feb 2011. ISSN 1434-6052. doi:[10.1140/epjc/s10052-011-1541-5](https://doi.org/10.1140/epjc/s10052-011-1541-5).
- [185] Chiara Arina. Review on Dark Matter Tools. In *Tools for High Energy Physics and Cosmology*, 12 2020.
- [186] Edward W. Kolb and Michael S. Turner. *The Early Universe*, volume 69. 1990. ISBN 978-0-201-62674-2. doi:[10.1201/9780429492860](https://doi.org/10.1201/9780429492860).
- [187] Kyoungchul Kong and Konstantin T. Matchev. Precise calculation of the relic density of Kaluza-Klein dark matter in universal extra dimensions. *JHEP*, 01:038, 2006. doi:[10.1088/1126-6708/2006/01/038](https://doi.org/10.1088/1126-6708/2006/01/038).
- [188] Anirban Das and Basudeb Dasgupta. Selection Rule for Enhanced Dark Matter Annihilation. *Phys. Rev. Lett.*, 118(25):251101, 2017. doi:[10.1103/PhysRevLett.118.251101](https://doi.org/10.1103/PhysRevLett.118.251101).
- [189] Kim Griest and David Seckel. Three exceptions in the calculation of relic abundances. *Phys. Rev. D*, 43:3191–3203, 1991. doi:[10.1103/PhysRevD.43.3191](https://doi.org/10.1103/PhysRevD.43.3191).
- [190] Geraldine Servant and Timothy M.P. Tait. Is the lightest Kaluza-Klein particle a viable dark matter candidate? *Nucl. Phys. B*, 650:391–419, 2003. doi:[10.1016/S0550-3213\(02\)01012-X](https://doi.org/10.1016/S0550-3213(02)01012-X).
- [191] Junji Hisano, Ryo Nagai, and Natsumi Nagata. Effective Theories for Dark Matter Nucleon Scattering. *JHEP*, 05:037, 2015. doi:[10.1007/JHEP05\(2015\)037](https://doi.org/10.1007/JHEP05(2015)037).
- [192] Genevieve Belanger, Ali Mjallal, and Alexander Pukhov. Recasting direct detection limits within micrOMEGAs and implication for non-standard Dark Matter scenarios. *Eur. Phys. J. C*, 81(3):239, 2021. doi:[10.1140/epjc/s10052-021-09012-z](https://doi.org/10.1140/epjc/s10052-021-09012-z).
- [193] Junji Hisano, Koji Ishiwata, and Natsumi Nagata. Gluon contribution to the dark matter direct detection. *Phys. Rev. D*, 82:115007, 2010. doi:[10.1103/PhysRevD.82.115007](https://doi.org/10.1103/PhysRevD.82.115007).
- [194] J. Billard, L. Strigari, and E. Figueroa-Feliciano. Implication of neutrino backgrounds on the reach of next generation dark matter direct detection experiments. *Phys. Rev. D*, 89(2):023524, 2014. doi:[10.1103/PhysRevD.89.023524](https://doi.org/10.1103/PhysRevD.89.023524).

- [195] E. Aprile et al. Physics reach of the XENON1T dark matter experiment. *JCAP*, 04:027, 2016. doi:[10.1088/1475-7516/2016/04/027](https://doi.org/10.1088/1475-7516/2016/04/027).
- [196] E. Aprile et al. First Dark Matter Search Results from the XENON1T Experiment. *Phys. Rev. Lett.*, 119(18):181301, 2017. doi:[10.1103/PhysRevLett.119.181301](https://doi.org/10.1103/PhysRevLett.119.181301).
- [197] Jan Conrad. Indirect Detection of WIMP Dark Matter: a compact review. In *Interplay between Particle and Astroparticle physics*, 11 2014.
- [198] E. Charles et al. Sensitivity Projections for Dark Matter Searches with the Fermi Large Area Telescope. *Phys. Rept.*, 636:1–46, 2016. doi:[10.1016/j.physrep.2016.05.001](https://doi.org/10.1016/j.physrep.2016.05.001).
- [199] Stefano Moretti, Dermot O’Brien, Luca Panizzi, and Hugo Prager. Production of extra quarks decaying to Dark Matter beyond the Narrow Width Approximation at the LHC. *Phys. Rev. D*, 96(3):035033, 2017. doi:[10.1103/PhysRevD.96.035033](https://doi.org/10.1103/PhysRevD.96.035033).
- [200] Stefano Moretti, Dermot O’Brien, Luca Panizzi, and Hugo Prager. Production of extra quarks at the Large Hadron Collider beyond the Narrow Width Approximation. *Phys. Rev. D*, 96(7):075035, 2017. doi:[10.1103/PhysRevD.96.075035](https://doi.org/10.1103/PhysRevD.96.075035).
- [201] Kyle Cranmer and Itay Yavin. Recast — extending the impact of existing analyses. *Journal of High Energy Physics*, 2011(4), Apr 2011. ISSN 1029-8479. doi:[10.1007/jhep04\(2011\)038](https://doi.org/10.1007/jhep04(2011)038).
- [202] Eric Conte, Béranger Dumont, Benjamin Fuks, and Chris Wymant. Designing and recasting lhc analyses with madanalysis 5. *The European Physical Journal C*, 74(10), Oct 2014. ISSN 1434-6052. doi:[10.1140/epjc/s10052-014-3103-0](https://doi.org/10.1140/epjc/s10052-014-3103-0).
- [203] A L Read. Presentation of search results: theCLstechnique. *Journal of Physics G: Nuclear and Particle Physics*, 28(10):2693–2704, sep 2002. doi:[10.1088/0954-3899/28/10/313](https://doi.org/10.1088/0954-3899/28/10/313).
- [204] *Workshop on Confidence Limits: CERN, Geneva, Switzerland 17 - 18 Jan 2000. 1st Workshop on Confidence Limits*, Geneva, 2000. CERN, CERN. doi:[10.5170/CERN-2000-005](https://doi.org/10.5170/CERN-2000-005).
- [205] Morad Aaboud et al. Search for dark matter and other new phenomena in events with an energetic jet and large missing transverse momentum using the ATLAS detector. *JHEP*, 01:126, 2018. doi:[10.1007/JHEP01\(2018\)126](https://doi.org/10.1007/JHEP01(2018)126).
- [206] Dipan Sengupta. The MadAnalysis5 implementation of the ATLAS in monojet+missing energy. 2018. doi:[10.7484/INSPIREHEP.DATA.HUH5.239F](https://doi.org/10.7484/INSPIREHEP.DATA.HUH5.239F).
- [207] Search for squarks and gluinos in final states with jets and missing transverse momentum using 139 fb^{-1} of $\sqrt{s} = 13 \text{ TeV}$ pp collision data with the ATLAS detector. 8 2019.

- [208] Federico Ambrogio. MadAnalysis 5 recast of ATLAS-CONF-2019-040. 2019. doi:[10.7484/INSPIREHEP.DATA.45EF.23SB](https://doi.org/10.7484/INSPIREHEP.DATA.45EF.23SB).
- [209] B. Dumont, B. Fuks, S. Kraml, S. Bein, G. Chalons, E. Conte, S. Kulkarni, D. Sengupta, and C. Wymant. Toward a public analysis database for LHC new physics searches using MADANALYSIS 5. *Eur. Phys. J.*, C75(2):56, 2015. doi:[10.1140/epjc/s10052-014-3242-3](https://doi.org/10.1140/epjc/s10052-014-3242-3).
- [210] Albert M Sirunyan et al. Search for top squarks and dark matter particles in opposite-charge dilepton final states at $\sqrt{s} = 13$ TeV. *Phys. Rev. D*, 97(3):032009, 2018. doi:[10.1103/PhysRevD.97.032009](https://doi.org/10.1103/PhysRevD.97.032009).
- [211] Albert M Sirunyan et al. Search for top squark pair production using dilepton final states in pp collision data collected at $\sqrt{s} = 13$ TeV. *Eur. Phys. J. C*, 81(1):3, 2021. doi:[10.1140/epjc/s10052-020-08701-5](https://doi.org/10.1140/epjc/s10052-020-08701-5).
- [212] Jack Y. Araz, Mariana Frank, and Benjamin Fuks. Reinterpreting the results of the LHC with MadAnalysis 5: uncertainties and higher-luminosity estimates. *Eur. Phys. J. C*, 80(6):531, 2020. doi:[10.1140/epjc/s10052-020-8076-6](https://doi.org/10.1140/epjc/s10052-020-8076-6).
- [213] Benjamin Fuks and Hua-Sheng Shao. QCD next-to-leading-order predictions matched to parton showers for vector-like quark models. *Eur. Phys. J. C*, 77(2):135, 2017. doi:[10.1140/epjc/s10052-017-4686-z](https://doi.org/10.1140/epjc/s10052-017-4686-z).